High Repetition Rate Laser Diagnostics for Combustion Applications

Sjöholm, Johan

2012

Citation for published version (APA):
Sjöholm, J. (2012). *High Repetition Rate Laser Diagnostics for Combustion Applications*. [Doctoral Thesis (compilation), Combustion Physics].

Total number of authors:
1

High Repetition Rate Laser Diagnostics for Combustion Applications

Doctoral Thesis

LUND
UNIVERSITY

Johan Sjöholm

Printed by Media-Tryck, Lund University
Lund, Sweden, 2012

Lund Reports on Combustion Physics, LRPC-157
ISBN 978-91-7473-319-8
ISSN 1102-8718
ISRN LUTFD2/TFCP-157-SE

Johan Sjöholm
Division of Combustion Physics
Department of Physics
Lund University
P.O. Box 118
SE-221 00, Lund, Sweden

To Agneta and our children

Abstract

High repetition rate laser diagnostics has proven to be a useful tool for studying combustion phenomena. Laser techniques are, in general, relatively non-intrusive and have the potential to measure specific species at very low concentrations and with extremely high temporal resolution. However, most laser systems in this field of research are limited to repetition rates below 100 Hz, and are thus incapable of resolving the fastest time scales in turbulent combustion. For this purpose, the multi-YAG laser systems at Lund University have been used. These consist of four double-pulsed Nd:YAG lasers combined into one unit with a single optical output. This allows eight high-energy laser pulses to be fired in very rapid succession. In order to match the repetition rate of the multi-YAG systems, framing cameras consisting of eight intensified CCD detectors with a single optical input were used.

Several of the measurements presented in this thesis were made in optically accessible engines. These engines were based on production line engines that were modified for optical measurements through the addition of a Bowditch piston extension. This gives optical access to the combustion chamber from below via a 45 degree mirror and in some cases from the sides as well. The combustion process in the engines has been studied using a number of laser techniques including laser-induced fluorescence (LIF), Raman scattering and laser-induced incandescence (LII).

In the work presented in this thesis, multi-YAG laser systems were used to study mixture preparation through the application of high-speed fuel tracer LIF in several different optical engines, both light- and heavy-duty, and various combustion concepts. High-speed LII and Raman spectroscopy were used to study combustion in a heavy-duty diesel engine. This thesis also presents fuel LIF measurements on a fuel tracer using structured laser illumination planar imaging (SLIPI) in the same heavy-duty diesel engine.

Various laser techniques were further developed, including high-speed LII and the adaptation of the SLIPI technique for engine measurements. Development of simultaneous measurements of four species in a turbulent flame, and comparisons of different schemes for carbon monoxide LIF were also made. Finally, an optical parametric oscillator (OPO) unit was tested and evaluated together with the multi-YAG system.

Populärvetenskaplig sammanfattning

Vår värld drivs av förbränning. Från den lilla elden som används vid matlagning till gigantiska gasturbiner och kolkraftverk som genererar en stor del av all elektricitet. Dessutom så drivs nästan alla fordon av förbränningsmotorer. Det har uppskattats att över nittio procent av alla energi vi i världen omvandlar kommer från förbränning i någon form.

Det är således ganska lätt att inse att en liten förändring i hur effektivt vi använder till exempel olja och kol kan få stora konsekvenser på en global nivå. En annan aspekt av förbränning är att flera av de ämnen som kan finnas med i avgaserna, såsom sot, kväveoxider och svaveloxider, är skadliga för vår hälsa. Att minska dessa utsläpp är inte helt enkelt och kräver ofta dyr och avancerad efterbehandling av avgaserna. Målet med stora delar av forskningen inom förbränningsområdet idag är att minska de skadliga ämnena i avgaserna och att samtidigt höja effektiviteten. För att åstadkomma detta krävs dock en ökad förståelse av de bakomliggande processerna i förbränningen.

Optiska metoder och då speciellt de som använder lasrar har visat sig vara användbara verktyg för att studera förbränningsprocesser. Genom att använda en laser för att belysa t.ex. en flamma kan man detektera enskilda ämnen och även radikaler som finns i mycket låga koncentrationer. Dessutom kan väldigt hög tidsupplösning åstadkommas, vilket effektivt fryser flödet och skapar skarpa bilder utan rörelseoskärpa. Ett vanligt förfarande är att forma laserstrålen till ett tunt ark, som man sen leder genom objektet man vill studera. Genom att placera en kamera i nittiograders vinkel till arket kan man skapa en tvådimensionell bild som då visar ett tvärsnitt av objektet.

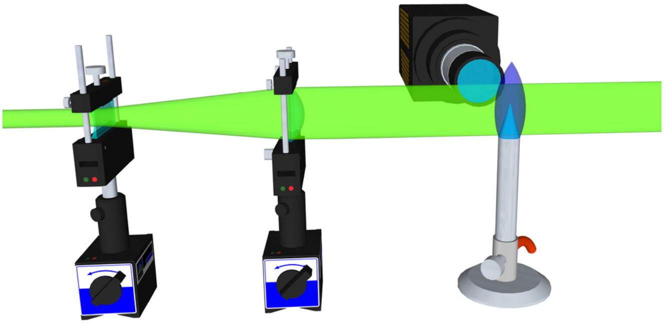

Illustration av laserarksavbildning av en flamma.

Vill man studera turbulent förbränning, som den i förbränningsmotorer eller i gasturbiner, kan det vara av intresse att följa flödet i tiden genom att ta flera laserarks bilder i snabb följd. Dock rör sig turbulenta flöden generellt sett snabbare än vad vanliga lasersystem klarar av att följa. Således krävs ett extraordinärt lasersystem för att analysera flödet. I Lund har vi för detta syfte så kallade multi-YAG system. Dessa system kan producera åtta laserpulser i extremt snabb följd, ner mot miljondelar av en sekund mellan laserpulserna.

Ett exempel på höghastighets laserdiagnostik med en Multi-YAG laser är de serier som visar bränslekoncentrationen i motorer som presenteras i denna avhandling. Motorerna var ombyggda med kvartsdelar i kolven och runt förbränningsrummet vilket möjliggjorde laserarksmätningarna. På detta sätt kan man följa hur bränslet blandas med luften i cylindern och sen se hur och var bränslet förbränns. Ett annat exempel är studier av sot i motorerna. Här används laserarket för att belysa sot inuti en dieselmotor. För att förstå vad som händer i den högst turbulenta miljön inuti en diesel motor måste man följa sotet över tiden med flera bilder.

Man kan också använda en Multi-YAG laser för att titta på flera ämnen samtidigt. För att göra detta bygger man om lasern så att pulserna får olika våglängd. Eftersom olika ämnen absorberar olika våglängder kan man således välja vilket ämne man vill studera. Man kan på detta sätt ta bilder av fyra ämnen samtidigt. Till skillnad från att ta dessa fyra bilderna vid olika tidpunkter så kan simultana mätningarna visa hur ämnena överlappar och interagerar i en turbulent och stokastisk miljö.

Av stort intresse för dieselmotorer är hur bränslet blandas med luften i cylindern. Dieselmotorer använder idag direktinsprutning med mycket högt tryck. Detta gör att bränslet, som är en vätska, snabbt omvandlas till en gassprej i cylindern. Denna gas blandas sedan med luften i cylindern och när rätt koncentration uppnåtts börjar blandningen brinna på grund av den höga temperaturen. Då detta sker kommer sot att bildas, men exakt hur och varför är inte helt klart. I ett försök till att förstå detta så mättes blandningens koncentration precis vid den punkt där sprejen börjar brinna. Detta visade sig dock inte förklara hur mycket sot som motorn producerade. Troligen på grund av att sotet som bildas i sprejen till stor del brinner upp senare i förbränningen.

I en annan studie mättes hur bränslesprejen interagerar med de omgivande väggarna i förbränningsrummet. Efter en bit så träffar sprejen oftast en vägg vilket gör att flödet riktas om till att följa väggen. För att ytterligare komplicera det hela så finns det flera sprejer i förbränningsrummet vilket gör att sprejflödena som går längs väggarna kolliderar med varandra. Resultaten visade att efter det att sprejen träffat väggen i förbränningsrummet så blandas mycket mindre luft in i sprejen än man förväntade sig vilket kan leda till att mer sot genereras.

List of papers

I. Seyfried, H., Olofsson, J., **Sjöholm, J.**, Richter, M., Aldén, M., Vressner, A. and Johansson, B., *High-Speed PLIF Imaging for Investigation of Turbulence Effects on Heat Release Rates in HCCI Combustion*, SAE Technical Paper 2007-01-0213, 2007.

II. Bai, X.S., Yu, R., Vressner, A., Hultqvist, A., Johansson, B., Olofsson, J., Seyfried, H., **Sjöholm, J.**, Richter, M. and Aldén, M., *Effect of Turbulence on HCCI Combustion*, SAE Technical Paper 2007-01-0183, 2007.

III. Persson, H., **Sjöholm, J.**, Kristensson, E., Johansson, B., Richter, M. and Aldén, M., *Study of Fuel Stratification on Spark Assisted Compression Ignition (SACI) Combustion with Ethanol Using High Speed Fuel PLIF*, SAE Technical Paper 2008-01-2401, 2008.

IV. **Sjöholm, J.**, Kristensson, E., Richter, M., Aldén, M., Göritz, G. and Knebel, K., *Ultra high speed pumping of an OPO laser, for high speed laser-induced fluorescence measurements*, Measurement Science and Technology, 20, 025306, 2009.

V. Aronsson, U., Chartier, C., Andersson, Ö., Egnell, R., **Sjöholm, J.**, Richter, M. and Aldén, M., *Analysis of the Correlation Between Engine-Out Particulates and Local Φ in the Lift-Off Region of a Heavy Duty Diesel Engine Using Raman Spectroscopy*, SAE International Journal of Fuels and Lubricants, 2(1):645-660, 2009.

VI. Aronsson, U., Chartier, C., Andersson, Ö., Johansson, B., **Sjöholm, J.**, Wellander, R., Richter, M., Aldén, M. and Miles, P., *Analysis of EGR Effects on the Soot Distribution in a Heavy Duty Diesel Engine using Time-Resolved Laser Induced Incandescence*, SAE Technical Paper 2010-01-2104, 2010.

VII. **Sjöholm, J.**, Wellander, R., Bladh, H., Richter, M., Bengtsson, P.-E., Alden, M., Aronsson, U., Chartier, C., Andersson, Ö. and Johansson, B., *Challenges for In-cylinder High-Speed Two-Dimensional Laser-Induced Incandescence Measurements of Soot*, SAE Technical paper 2011-01-1280, 2011.

VIII. **Sjöholm, J.**, Chartier, C., Kristensson, E., Berrocal, E., Gallo Y., Richter, M., Andersson, Ö., Aldén, M. and Johansson, B., *Quantitative in-cylinder fuel measurements in a heavy duty diesel engine using Structured Laser Illumination Planar Imaging (SLIPI)*, COMODIA 2012, MD-10, 2012.

IX. Chartier, C., Gallo, Y., Andersson, Ö., Johansson. B., **Sjöholm, J.**, Kristensson, E., Richter, M. and Aldén, M., *Air-entrainment in wall-jets using SLIPI in a heavy-duty diesel engine*, submitted to SAE fuel and Lubricants 2012, SAE draft #12FFL-0272, 2012.

X. **Sjöholm, J.**, Rosell, J., Li, B., Richter, M., Li, Z.S., Bai, X.S. and Aldén, M., *Simultaneous visualization of OH, CH, CH_2O and toluene PLIF in a methane jet flame with varying degrees of turbulence.*, Accepted for oral presentation at the 34th International Symposium on Combustion, 2012.

XI. Rosell, J., **Sjöholm, J.**, Richter, M. and Aldén, M., *Comparison of three schemes of two-photon laser induced fluorescence for CO detection in flames*, submitted to applied spectroscopy, 2012.

Related work

A. Joelsson, T., Yu, R., **Sjöholm, J.**, Tunestål, P. and Bai, X.S., *Effects of Negative Valve Overlap on the Auto-ignition Process of Lean Ethanol/Air Mixture in HCCI-Engines*, SAE Technical Paper 2010-01-2235, 2010.

B. Lantz, A., Collin, R., **Sjöholm, J.**, Li, Z.S., Petersson, P. and Aldén, M., *High-speed fuel/hydroxyl radical imaging in a gas turbine pilot burner*, AIAA Journal, Vol. 50, No. 4, April 2012.

C. Brackmann, C., Rosell, J., **Sjöholm, J.**, Richter, M., Bood, J. and Aldén, M., *Picosecond excitation for reduction of photolytic effects in two-photon laser-induced fluorescence of CO*, Accepted for oral presentation at the 34th International Symposium on Combustion, 2012.

Contents

Abbreviations

A/D	Analogue to Digital
AEOI	After End Of Injection
ASE	Amplified Stimulated Emission
ASOI	After Start Of Injection
ATDC	After Top Dead Centre
BBO	Beta Barium Borate
CA10	Crank Angle for 10% Burned Mass Fraction
CA50	Crank Angle for 50% Burned Mass Fraction
CA90	Crank Angle for 90% Burned Mass Fraction
CAD	Crank Angle Degree
CCD	Charge-Coupled Device
CI	Compression Ignition
CMOS	Complementary Metal-Oxide Semiconductor
COV	Coefficient of Variation
DI	Direct Injection
DNS	Direct Numerical Simulations
DoE	Design of Experiments
EGR	Exhaust Gas Recirculation
EOI	End Of Injection
FSN	Filtered Smoke Number
HCCI	Homogeneous Charge Compression Ignition
HR	High Reflectance (dielectric mirror)
HT	High Transmission (dielectric mirror)
IC	Internal Combustion
ICCD	Intensified Charge-Coupled Device
IMEP	Indicated Mean Effective Pressure

IR	Infrared
LES	Large Eddy Simulations
LIF	Laser-Induced Fluorescence
LII	Laser-Induced Incandescence
MCP	MicroChannel Plate
multi-YAG	System of four Nd:YAG lasers
Nd:YAG	Neodymium-doped Yttrium Aluminium Garnett
NOx	Nitric oxides, e.g. NO and NO_2
NVO	Negative Valve Overlap
OPO	Optical Parametric Oscillator
PAH	PolyAromatic Hydrocarbon
PFI	Port Fuel Injection
PIV	Particle Image Velocimetry
PLIF	Planar Laser-Induced Fluorescence
PM	Particulate Matter
PPC	Partially Premixed Combustion
RANS	Reynolds Averaged Navier Stokes
RTP	Room Temperature and Pressure
SACI	Spark Assisted Compression Ignition
SHG	Second Harmonic Generating (crystal)
SI	Spark Ignition
SLIPI	Structured Laser Illumination Planar Imaging
SOI	Start of Injection
SOx	Sulphuric oxides e.g. SO_2
TDC	Top Dead Centre
UHC	Unburned HydroCarbons
UV	Ultraviolet
Φ	Equivalence ratio
λ	Relative air-fuel ratio, $\lambda = \Phi^{-1}$

Chapter 1 Introduction

1.1 The need for high-speed combustion diagnostic

The human use of energy worldwide in 2009 has been estimated to be around 140 000 TWh [1]. It has further been estimated that over 91% of this energy was provided by combustion processes (the remainder being nuclear, hydro, solar energy, etc.), and that 81% originated from fossil fuels, the remaining 10% being biofuels and energy from waste [1]. It is thus important that we increase the efficiency of combustion processes as this would lower the worldwide consumption of fossil fuels. This would consequently extend the period of time over which oil and oil derivatives could be used as fuels before they have to be phased out due to prohibitively high prices.

NOx, particles and SOx are generated through the combustion of hydrocarbons. These have all been shown to have adverse effects on health, such as increased mortality, respiratory diseases and cardiovascular effects [2]. Reducing the concentration of these harmful species in our environment is, therefore, of the utmost importance. However, lowering the production of NOx and particulate matter without also lowering the efficiency of modern engines requires an increased understanding of the combustion processes, and therefore calls for advanced combustion diagnostics.

Optical diagnostic methods have proven to be useful for studying combustion phenomena, and laser diagnostics in particular have demonstrated great potential and promising results. Specific species and radicals at very low concentrations can be studied with lasers. Extremely high temporal resolution can also be achieved, effectively freezing the flow field and even chemical reactions. Last, but not least, these methods are relatively non-intrusive, and provide accurate, reliable information with high validity [3].

In most practical combustion environments, such as those in diesel and gasoline engines, highly turbulent conditions prevail. The reason for this is that turbulence increases the mixing between different regions which in turn increase the combustion efficiency [4]. Turbulence covers a wide range of spatial and temporal scales: from the largest, and thus slowest vortices that can be created in a given system, down to the

Kolmogorov scale, where the turbulent energy is dissipated as heat [5]. This energy cascade is illustrated in Figure 1.1.

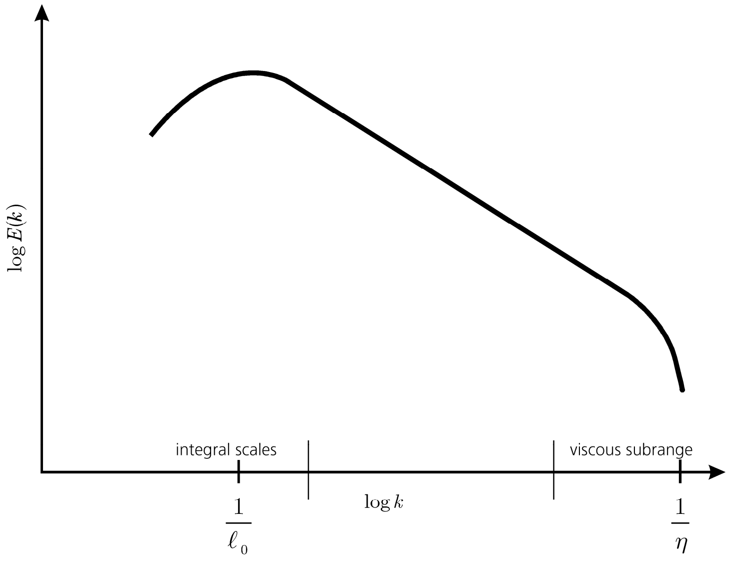

Figure 1.1 Log-Log plot showing the energy in the turbulence as a function of the inverse of the length scale (smaller length scales to the right) [6].

As most laser systems within this field of research are limited to repetition rates below 100 Hz they are clearly incapable of following turbulent combustion events in e.g. internal combustion (IC) engines or gas turbines. For this purpose, alternative laser sources and detectors with sufficiently high repetition rates are required. Furthermore, the cycle-to-cycle variations in IC engines can be substantial. This makes it difficult, and in some cases even impossible, to correlate a measurements made during one cycle to one made in another cycle. It is thus necessary to make several measurements in one cycle to fully understand the time development of the combustion processes.

Chapter 2 Equipment

This chapter describes the equipment used in the work presented in this thesis. It does not provide a comprehensive summary of all the equipment that can be used for combustion diagnostics.

2.1 Lasers

A laser, the name being an acronym for “light amplification by stimulated emission of radiation”, is a device which, by means of a gain medium placed inside a cavity, emits a coherent beam of radiation in the infrared (IR) to ultraviolet (UV) region of the electromagnetic spectrum. The gain medium can be virtually any medium that is reasonably transparent and has the appropriate energy levels. Energy is usually added to the gain medium by so-called pumping, for example, in the form of photons from flash lamps or diodes.

2.1.1 Nd:YAG lasers

Nd:YAG lasers are one of the most common solid state lasers. The gain medium is an yttrium aluminium garnet (YAG) crystal ($Y_3Al_5O_{12}$), doped with neodymium (Nd^{3+}) ions, usually at concentrations of around 1%. Through pumping, the Nd^{3+} ions can be excited to either the $^4F_{5/2}$ state or the energetically higher lying absorption band. The ions relax down to the $^4F_{3/2}$ level through non-radiating processes. Lasing can then be achieved through decay from the $^4F_{3/2}$ level to the $^4I_{11/2}$ level. Finally, the rapid decay to the ground level $^4I_{9/2}$ gives a four-level laser system. This system produces a laser wavelength of 1064 nm. The $^4I_{13/2}$ level can also be used for laser action producing a wavelength of 1312 nm through a four-level system, and it is also possible to use the ground state in a three-level laser system resulting in a wavelength of 946 nm. However, the best efficiency is achieved at 1064 nm [7, 8].

Nd:YAG lasers can be either pulsed or continuous. Pulsed Nd:YAG laser systems usually utilize flash lamps or diodes for pumping. The laser pulses can be created through Q-switching, a process in which the intra-cavity losses are kept high until the appropriate population inversion is achieved. The Q-switch is then opened, often using polarization effects in an electro-optical element. This allows a cascade of photons (laser pulse) to rapidly build up through stimulated emission. The laser pulse continues until the population inversion is lost or the Q-switch is closed. Thermal effects usually limit the output power (pulse energy × repetition rate) that can be achieved.

Frequency conversion through non-linear crystals, e.g. beta barium borate (BBO) or potassium dideuterium phosphate (KD*P), can be used to change the fundamental wavelength of 1064 nm to 532 nm (by frequency doubling, also called second-harmonic generation), 355 nm (the third harmonic), 266 nm (the fourth harmonic) and 213 nm (the fifth harmonic). Shorter wavelengths are usually not used due to the high absorbance of air below ~200 nm.

2.1.2 High-power and high repetition rate lasers

One drawback of conventional Nd:YAG lasers is the limited repetition rate coupled to the available output power. The high pulse energy required for several applications, e.g. pumping of dye lasers or measurements using laser induced incandescence (LII) usually limits the repetition rate to 10 – 100 Hz. On the other hand, in high repetition rate systems, i.e. >10 kHz, the pulse energy is severely limited.

Kilohertz laser systems can today produce around 10 mJ/pulse at 10 kHz and 532 nm. This is still an impressive 100 W of optical power in the green part of the spectrum. Applications like laser induced fluorescence (LIF) of CO and CH, which have intrinsically low signal levels, are still very challenging using these systems. However, there are applications in which kHz Nd:YAG lasers with comparatively low pulse energy have shown potential. One such example is fuel tracer LIF using biacetyl. The high fluorescence yield of biacetyl and the possibility of exciting biacetyl with 355 nm radiation (the third harmonic of a Nd:YAG laser) allows for imaging even in harsh environments such as those in IC engines [9]. Another feasible application is high-speed particle image velocimetry (PIV) [10].

OH LIF has also been demonstrated with a dye laser modified for kHz repetition rates. However, the available pulse energy was rather limited (25 µJ/pulse at 5 kHz and 283 nm) [11]. The possibility of OH LIF using a kHz Nd:YLF laser system without a dye laser has also been demonstrated [12]. Gas-phase toluene LIF measurements at 10 kHz have been demonstrated using the fourth harmonic (266 nm) from a high-speed Nd:YAG laser. The temperature field was calculated using data from two cameras with different optical filters [13].

Another option for high-speed laser combustion diagnostics is a laser system that can produce a burst of pulses from one laser [14]. These systems are based on a continuous wave (CW) Nd:YAG laser beam which is “sliced” in time using either two Pockels cells [15] or an acousto-optic modulator (AOM) [16] to create a burst of pulses. The burst is then sent through several amplifier stages to increase the pulse energy. The output pulse energy of these systems is limited by the amount of amplification that can be generated without free running and the duration, or length, of the pulse train is limited by the amplifier flash lamps discharge duration. Newer versions of these systems have even been used for quasi-three-dimensional measurements [17].

Copper vapour lasers have also been used for high-speed combustion diagnostics. These typically operate at repetition rates over 10 kHz and produce wavelengths of either 511 or 578 nm. As the pulse energy at these repetition rates is limited to a couple of mJ, these systems are usually used for Mie scattering and PIV in practical applications such as IC engines [18, 19]. Similarly to kHz Nd:YAG lasers, copper vapour lasers can be used to pump dye lasers but the output pulse energy is usually very limited.

One final way to circumvent the limitation on repetition rate and output power is to use a system combined of several lasers. Such a system of lasers can generate several high-power pulses in rapid succession. This idea was presented already in the early 1980s [20]. The multi-YAG laser systems presented in the next section are an example of such combined systems that have been extensively applied for laser diagnostics in combustion environments.

2.1.3 Multi-YAG lasers

The Division of Combustion Physics at Lund University has two multi-YAG laser systems. The first was acquired in 1996 and has been extensively used for various measurements. The second was delivered in 2007 and has been used for LIF, Raman spectroscopy and LII measurements. The following sections deal mainly with the new multi-YAG system. Additional information regarding the first multi-YAG system in Lund can be found in [21, 22]. Similar systems are now also available at other labs [23].

Each multi-YAG system consists of four separate Nd:YAG lasers, combined into one system, as shown in Figure 2.1. Each laser operates at a repetition rate of 10 Hz, and at the normal fundamental laser wavelength for Nd:YAG lasers, 1064 nm (red lines in Figure 2.1).

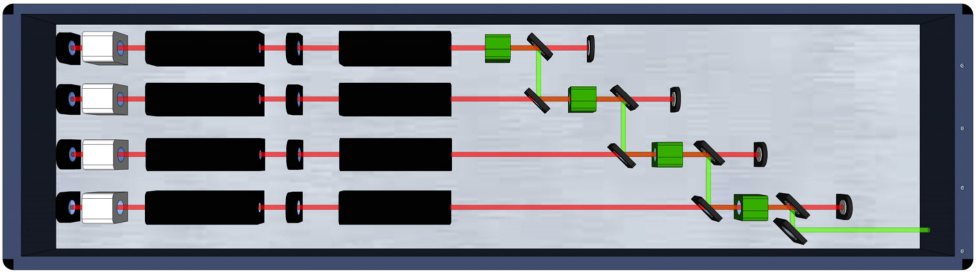

Figure 2.1 Illustration of the new multi-YAG laser system in the 532 nm configuration. Each laser consists of, from left to right, a cavity mirror, a Q-switch, an oscillator stage, an output coupler, an amplifier stage and a second-harmonic-generating crystal (green).

Combining four laser beams with acceptable losses while maintaining the original wavelength is difficult. Therefore, a frequency-doubling and combination scheme is adopted in these systems. In this scheme, the beam from the first laser is frequency doubled to 532 nm using a second-harmonic-generating (SHG) crystal. The frequency-doubled beam is then separated from the fundamental beam by a dielectric mirror (coated HR 532 and HT 1064) that reflects the 532 nm at right angles while transmitting the 1064 nm beam.

The frequency-doubled beam from the first laser is then spatially overlapped with the fundamental beam from the second laser using a second dielectric mirror. The two combined beams are then sent through a second SHG crystal. As the phase-matching condition in the crystal is not met for both wavelengths at the same time, the 532 nm beam from the first laser can pass through unchanged, while the fundamental from the second laser is frequency doubled to 532 nm.

This procedure is then repeated for all four lasers and the result is a single beam consisting of the 532 nm pulses from all four lasers. An extra separation stage containing two dielectric mirrors is placed after the fourth SHG. This separates the fundamental beam from the fourth laser and directs the 532 nm beam to the output port of the laser. It should be noted that there are some losses in the recombination system (absorption and reflections from surfaces) that lower the energy from the first laser relative to the last in the beam recombination.

It is also possible to place a fourth harmonic generator (FHG) before the final separation stage. The single FHG crystal frequency doubles all four 532 nm pulses to produce a wavelength of 266 nm. Naturally, the dielectric mirrors after the FHG are also changed to ones that reflect 266 nm, while transmitting 1064 and 532 nm (HR 266, HT 532 and HT 1064).

The multi-YAG laser system can also generate 355 nm radiation. As 355 nm generation requires mixing 532 nm and 1064 nm this cannot be done using a single third-harmonic-generating (THG) crystal in a manner similar to 266 nm generation. Instead, each laser beam is individually doubled to 532 nm and tripled to 355 nm using a THG crystal. The 355 nm beam is separated from the 1064 and 532 nm beams using a dielectric mirror (coated HR 355 nm, HT 532 nm and HT 1064 nm). The beams are overlapped after the SHG crystals as this minimizes the losses in the system. The Multi-YAG in the 355 nm configuration is shown in Figure 2.2.

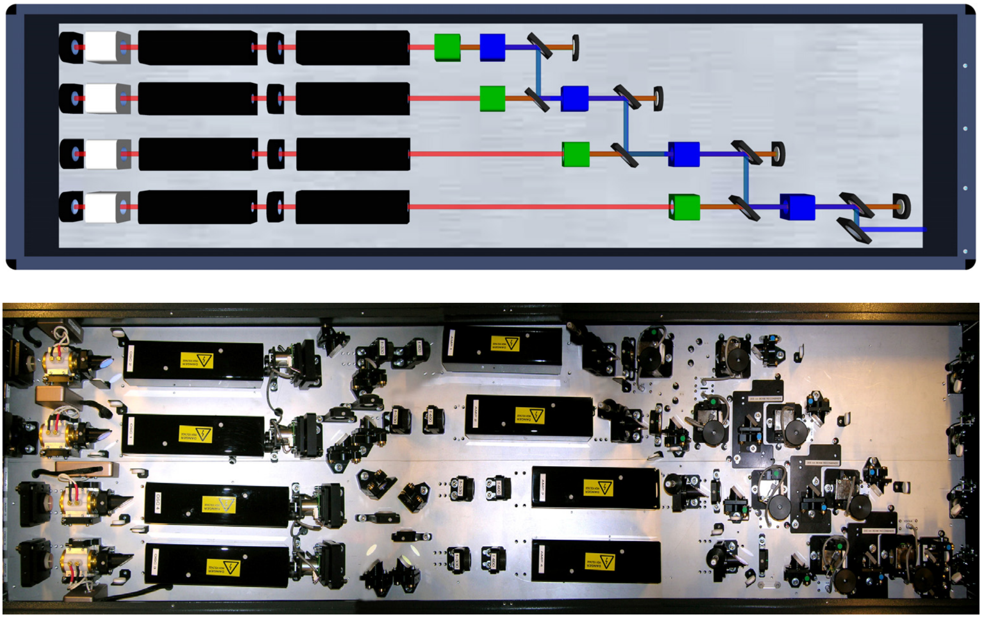

Figure 2.2 Illustration of the new multi-YAG laser system in the 355 nm configuration (top) and a photo of the same system (bottom).

Optimizing the 355 nm output from the multi-YAG laser can be challenging as the lambda half plates before the SHG crystals require some realignment (relative to the position used for 532 nm generation) in order to obtain optimal energy output. For maximum output energy at 355 nm the SHG process must be slightly un-optimized. Thus, the lambda half plate is turned slightly off axis, turning the polarization of the beam slightly. This gives the correct balance between 1064 and 532 nm in the THG crystal. The combined system for each laser thus has three degrees of freedom (lambda half plate rotation, and the positions of the SHG and FHG crystals) and only one variable (energy), related through non-linear processes. Considerable patience is required to optimise this system.

Due to the relatively long duration of the flash lamp discharge (~400 μs) it is possible to operate the multi-YAG system in double-pulse mode, i.e. the Q-switch is opened twice during one flash lamp discharge. This extends the number of pulses per pulse train from four to eight. A sketch of a typical pulse train is shown in Figure 2.3.

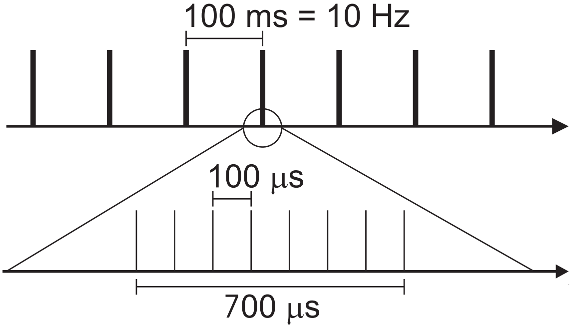

Figure 2.3 Typical time scales of the pulse train from the multi-YAG laser system. The separation between the pulses is 100 μs and the entire pulse train is 700 μs long from the first to the last pulse.

In single-pulse mode the time separation is completely arbitrary, without any restriction on pulse energy as long as the separation is not zero, i.e. the pulses are overlapping in time. In double-pulse mode the pulse energy is a function of the time between the two pulses from each laser. As the first pulse nullifies the population inversion in the gain medium, the time available for pumping prior to the second pulse limits its output energy. In the new Multi-YAG system, the pulse separation can be set between 20 and ~200 μs. As the pulses can be interleaved the separation between adjacent pulses can be as short as 5 μs for equidistant pulse trains.

Balancing the energy between the eight pulses usually requires the energy of the final (fourth) laser to be lowered, as some of the energy from the first laser will be lost in the recombination optics. The balance between the two pulses from one laser is achieved by first setting the desired distance between the pulses and then moving the pulses in time relative to the flash lamp discharge, thus changing the energy available to the first laser pulse. Some of the available pulse energies from the two multi-YAG systems are given in Table 2.1.

Table 2.1 Comparison between the original and newer multi-YAG systems pulse energies for separate beam operation and double-pulse operation, with optimum pulse separation. As separate beams at 266 nm are impossible, the average combined pulse energy is given instead.

	Original multi-YAG system	**New multi-YAG system**
Separate beam operation		
Laser energy at 532 nm	500 mJ/pulse	1400 mJ/pulse
Laser energy at 355 nm	~100 mJ/pulse	600 mJ/pulse
Laser energy at 266 nm	90 mJ/pulse	200 mJ/pulse
Double pulse operation (optimum pulse separation)		
Laser energy at 532 nm	200 mJ/pulse	350 mJ/pulse
Laser energy at 355 nm	~50 mJ/pulse	220 mJ/pulse
Laser energy at 266 nm	40 mJ/pulse	70 mJ/pulse
Available pulse separations in double-pulse mode	6.25 – 145 μs	5 – 200 μs

2.1.4 Dye lasers

Nd:YAG lasers, and most other lasers, can only produce fixed wavelengths due to the discrete energy levels of the gain medium. Dye lasers can be used when tuneable laser radiation is required. The gain medium in these systems is a dye consisting of large organic molecules dissolved in e.g. alcohols, providing broadband fluorescence bands. Different dyes are chosen depending on the desired wavelength. The abundant selection of dyes means that dye lasers can operate from the near UV region (>310 nm) to near IR wavelengths [24].

Dye lasers can be pumped with flash lamps, but it is more common to use another laser in the visible or UV region, e.g. a frequency-doubled (532 nm) or tripled (355 nm) Nd:YAG laser. The pulse duration of the dye laser is then determined by the duration of pump lasers pulse. Such a system is depicted in Figure 2.4, which shows an illustration of a modified Sirah, Cobra stretch dye laser. It should be noted that the beam going to the oscillator and the beam going to the pre-amplifier are actually stacked vertically, and not horizontally as shown in the sketch for convenience.

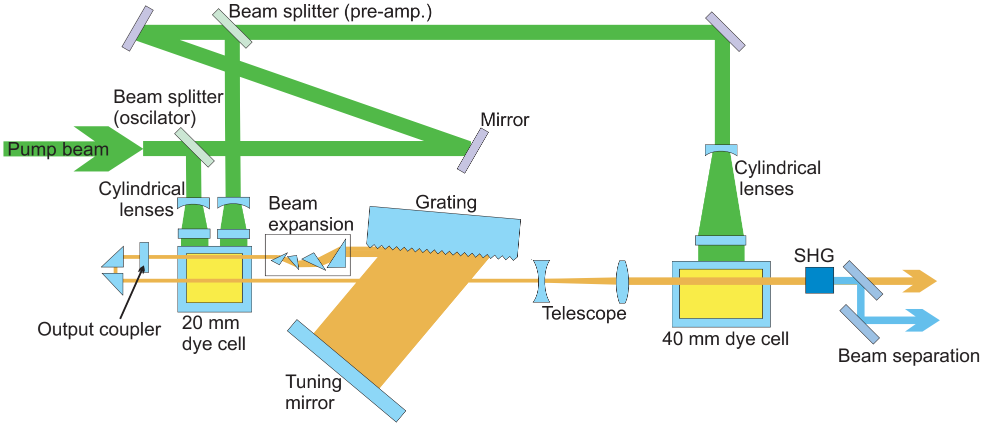

Figure 2.4 Illustration of a modified Sirah, Cobra Stretch dye laser. The pump beam is shown in green and the dye laser fundamental in orange.

The first pump beam that goes to the oscillator contains only a fraction of the pump beam energy. This is used to pump the laser cavity and thus initialize lasing action. The cavity is set up between the output coupler and a tuning mirror via a grating. The angle of the tuning mirror relative to the grating determines the dye laser wavelength from the broad fluorescence curve of the dye.

After the cavity, the dye laser beam is reversed through the same dye cell (slightly higher up) and intersected with the pre-amplifier pump beam. A telescope before the second amplifier stage enlarges the dye laser beam. About 70-80% of the pump beam energy is finally used in the 40 mm dye cell that constitutes the main amplifier. A SHG crystal can be used together with beam-separating mirrors after the dye laser if a wavelength in the UV is required. Other components, such as mixing crystals, etc. can be used depending on the required wavelength and pulse energy.

One problem associated with dye lasers is amplified stimulated emission (ASE), i.e. fluorescence from the dye that is not at the desired laser wavelength. Setting up the pump beams at a small angle to the dye laser beam can lower the amount of ASE. Furthermore, the output from the cavity can be filtered using polarizing optics before the pre-amplifier (ASE is unpolarized, in contrast to the dye laser beam).

At repetition rates higher than ~10 Hz, dye lasers can encounter problems due to depletion of the dye solution. If the dye in the active volume is not replaced between laser pulses the output power will decrease as a function of pulse order [21]. For operation with the multi-YAG laser system, this problem has been circumvented in a similar manner to the multi-YAG itself, i.e. by using four dye lasers. With a slight modification to the recombination optics, the multi-YAG systems can generate four separate output beams, effectively turning the multi-YAG into four separate lasers with common timing control. Each beam is then used to pump one dye laser of the type shown in Figure 2.4. The dye laser beams are recombined in the same manner as in the multi-YAG systems with four frequency-doubling crystals and dielectric mirrors selected for the appropriate wavelength [25]. The entire system is illustrated in Figure 2.5.

The limitation of this setup is that measurements using the fundamental wavelength of the dye laser are not feasible. If the dye laser fundamental wavelength is required a recombination system relying on the polarization of the beams could possibly be used. The main limitation in such a system is the polarisers as they must induce only low losses, while still being able to handle fairly high pulse energies and tuneable wavelengths. This recombination system has, however, not been tested using the four-dye-laser system and the multi-YAG laser.

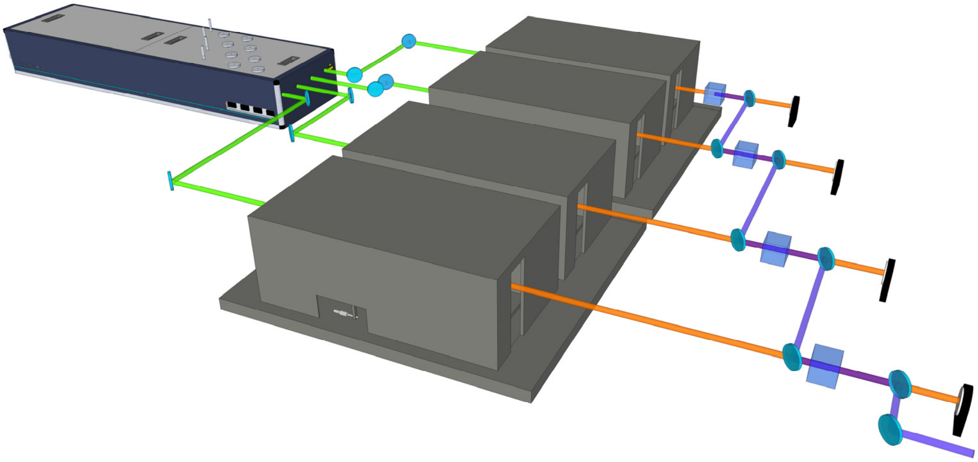

Figure 2.5 Illustration of four dye lasers pumped by the multi-YAG laser system. The beams are recombined after the dye lasers using four SHGs and eight dielectric mirrors.

2.1.5 Optical parametric oscillator (OPO)

Another method of creating high-speed tuneable laser radiation is to use an optical parametric oscillator (OPO). Very simplistically, an OPO splits one photon into two with lower frequency. As the energy in the each of the two photons is dependent on the angle of the active crystal, the output wavelength can be scanned by turning the crystal. An photograph of an OPO and a illustration of its components are given in Figure 2.6.

OPO systems show no evidence of the depletion effect seen in dye lasers. Thus, OPO systems can be pumped at very high repetition rates as long as the crystal can be sufficiently cooled to remove any absorbed energy.

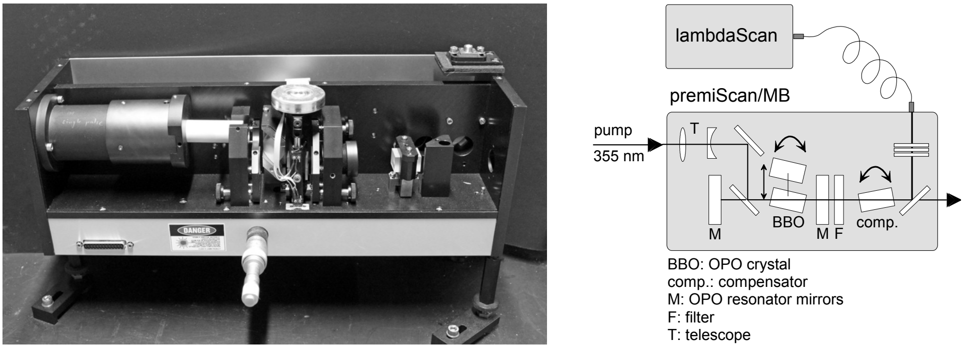

Figure 2.6 Photo of an OPO from GWU without the cover plates and peripheral components (left), and an illustration of its operational function (right).

A single OPO unit was used with the multi-YAG laser. This OPO was pumped by the recombined 355 nm beam from the multi-YAG. The 355 nm beam is first sent through a telescope to obtain the correct fluence through the crystal (see Figure 2.6). A higher 355 nm fluence gives higher conversion efficiency in the OPO, but in this setup the fluence must be kept below 0.7 J/cm^2 due to the damage-threshold of the BBO crystals in the OPO. The operating threshold is around 0.2 J/cm^2. Careful cleaning of the BBO crystals, preferably with isopropanol as BBO crystals are hygroscopic, is necessary before use to avoid damage to the surfaces at these high fluencies.

The 5 cm long cavity around the BBO crystals lowers the spectral width of the output beam to 3 – 5 cm^{-1}. The output wavelength is monitored using a fibre coupled wavemeter. In double-pulse operation (8 pulses from the multi-YAG), the telescope in the OPO can be switched to give the correct fluence through the crystal, despite the slightly lower pumping energy from the multi-YAG lasers.

It should be noted that the alignment between the four multi-YAG beams is extremely critical when using the OPO. In particular, the direction of the beams in the horizontal plane must not differ as this will cause the output wavelengths from the OPO to change between pulses. In addition, misalignment of the input beams (both horizontally and vertically) will cause significant differences in output power from the OPO. In fact, the output wavelength, measured by the wavemeter, can be used for the final fine tuning of the multi-YAG laser recombination optics in the horizontal plane.

2.2 Detectors

2.2.1 ICCD cameras

These cameras are based on an intensified charge-coupled device (ICCD) a cross section, of which is illustrated in Figure 2.7. The incoming light first encounters the photocathode which emits electrons when photons strike it. Voltages applied to the photocathode and the microchannel plate (MCP) then guide the electrons towards and through the MCP. The field applied across the MCP allows additional, secondary, electrons to be dislodged from the channel walls creating an avalanche effect. The avalanche of electrons finally strikes a phosphor screen (at a high negative voltage) that converts the electrons into photons. These photons are guided through a fibre bundle (usually tapered) to the CCD, where they create electron-hole pairs that can be trapped in the potential wells that correspond to the pixels. Data readout involves successively shifting the charges, one row at a time, towards one edge of the chip and at that edge shifting them towards a single A/D (analogue to digital) converter that converts the accumulated charge to a digital value.

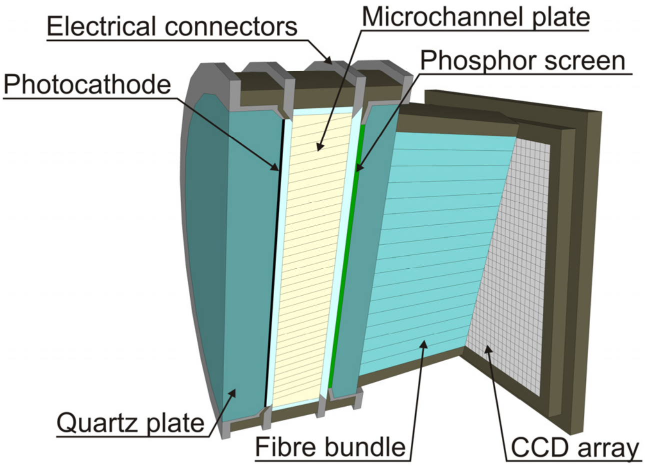

Figure 2.7 Illustration of the cross section of an ICCD. The intensifier is coupled to the CCD using a fibre bundle.

Signal linearity, i.e. a linear dependence between the number of incident photons and the detected signal (counts), is usually good in ICCDs as long as the incoming light level is below the saturation limit. In some cases the saturation limit can lie below the maximum limit of the A/D converter. It should be noted that, for low gain levels, the MCP will not amplify the signal sufficiently and no saturation will occur in the following steps, even for light levels that are well above the damage threshold of the photocathode.

The main advantage of these cameras is their extremely short exposure times, or gates, down to a couple of ns. Gating typically involves applying a short electrical activation pulse to the photocathode while the MCP and the phosphor screen are continuously active. This gives the fastest gating as the photocathode requires the lowest voltage for operation. For applications with high UV background levels, however, the highly energetic photons can cause the photocathode to emit electrons despite being inactivated. In such cases, it is possible to gate the MCP plate by turning off the voltage that allows the electron avalanche to progress through the MCP. This increases the background rejection ratio significantly but also increases the shortest available gating time.

2.2.2 High-speed framing cameras

A camera capable of at least MHz repetition rates is required to match the repetition rate of multi-YAG laser systems. A high collection efficiency is also required so that the camera can be used in applications with low signal strengths.

High-speed cameras using CMOS-chips for detection suffer from problems associated with signal linearity and read-out noise [26]. But they can be used together with multi-YAG laser systems, as has recently been demonstrated for CH LIF, an application with intrinsically low light levels [23]. Another problem is the limitation imposed on the resolution as the repetition rate is increased.

Historically, analogue film cameras have been used for high-speed imaging; an example of which is the “rotating mirror camera” where the photographic film is placed in a circle arc. A rotating mirror driven by an electric motor or turbine is placed at the centre of the circle thus reflecting the light across the film. However, it was not possible to synchronize the camera to an external event, and the only option was therefore to use the mirror in the camera as a master for the measurement [27]. Problems with image smearing and long film development times also made these systems very cumbersome to work with.

A more modern option is framing cameras. The two framing cameras in Lund, Imacon 468 and SIM 8, are slightly different in actual construction but the general structure is similar. They are both based on eight ICCDs that can be triggered individually. This allows for frame rates up to 100 MHz but limits the number of frames to eight per event.

Figure 2.8 A SIM 8 framing camera with an achromatic f = 100 mm, $f_{\#}$ = 2 B. Halle lens on a tripod, with tilt, rotation and height adjustment.

A single optical input lens is used in the Framing cameras, giving all eight ICCDs the same view of the measurement object. An optional intensifier can be placed after the initial lens. Apart from amplifying the signal, this transforms any incoming wavelength into the optimal wavelength for the optics and intensifiers in the cameras. This optional intensifier can be removed from both camers, and the cameras operated without it. For the SIM 8 camera, two intensifiers with varying phosphor decay time can be used: one with P46 phosphor (300 ns decay time) and one with FS phosphor (12 μs decay time). These decay times determine the minimum time separation between exposures if ghosting is to be avoided.

The difference between the two framing cameras lies mainly in the way light is split up before the eight ICCDs. In the Imacon 468 camera the light is split using an eight-faceted pyramid prism and eight small mirrors. In the newer SIM 8 camera the light is split using seven 50/50 beam splitter cubes, giving less optical aberrations as well as slightly higher efficiency. It should, however, be noted that at best, the detected signal for each CCD is less than one eighth of the original signal. The optional intensifier also increases noise levels somewhat. Another difference between the two cameras is that the SIM8 camera has a double exposure feature. This allows an additional eight images to be recorded after the first series. As the first images must be moved from the ICCDs this limits for how soon the second series can be triggered, but it is possible to record sequential 10 Hz pulse trains. Illustrations of the internal optics of the two cameras are shown in Figure 2.9 and Figure 2.10.

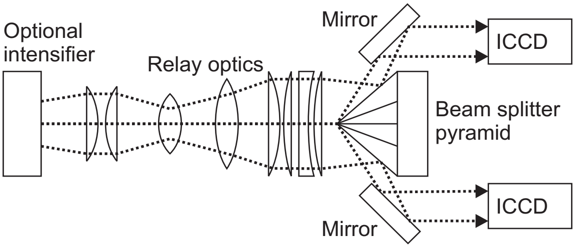

Figure 2.9 A sketch of the principal optical components in the Imacon 468 framing camera from Hadland. Only two of the eight ICCDs located in a ring around the pyramid prism are shown.

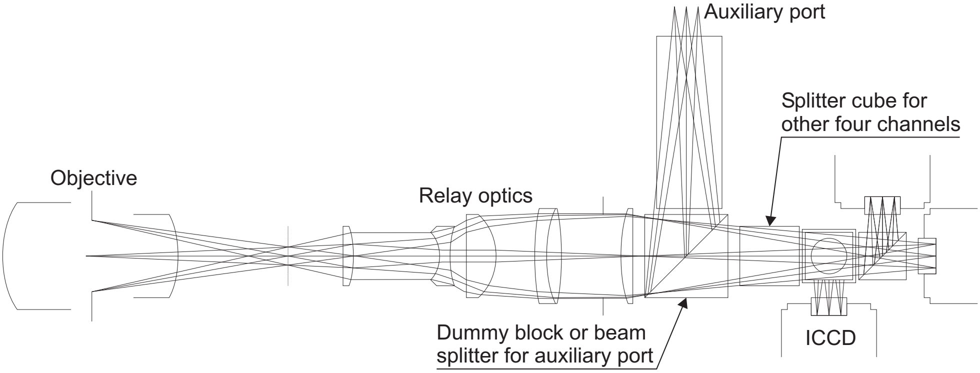

Figure 2.10 A sketch of a cross-section through the principal optical components in the SIM 8 framing camera from Specialised Imaging. Only three of the eight ICCDs are shown for clarity. Four of the other ICCDs would be located behind and one in front of the section shown.

2.2.3 Diodes

Fast diodes were used in this work mainly for monitoring the timing of the laser pulses relative to each other, e.g. from the multi-YAG system, or relative to other objects, e.g. optical engines or ICCD cameras. A diode (usually UV-sensitive) is also the easiest way to determine the pulse energy balance between the different pulses in a pulse train from the multi-YAG laser. Two aspects that must be considered in this application are that the diode is not saturated and that the correct termination is applied at the oscilloscope.

2.2.4 Spectrometers

Spectrometers are used to detect an optical signal as a function of its wavelength. A camera (e.g. an ICCD) is today most commonly used for detection. The camera covers a section of the wavelength spectrum making it possible to record single-shot spectra. If a wavelength region outside that covered by the camera is required the grating can be turned to change the projected wavelength segment.

The wavelength scale can be calibrated using gas discharge lamps that emit well known spectral lines. The spectral positions and strengths, etc. of these lines are tabulated for most atoms [28]. For the UV region, i.e. 200 – 400 nm, lamps with Zn, Cd and Hg are good options.

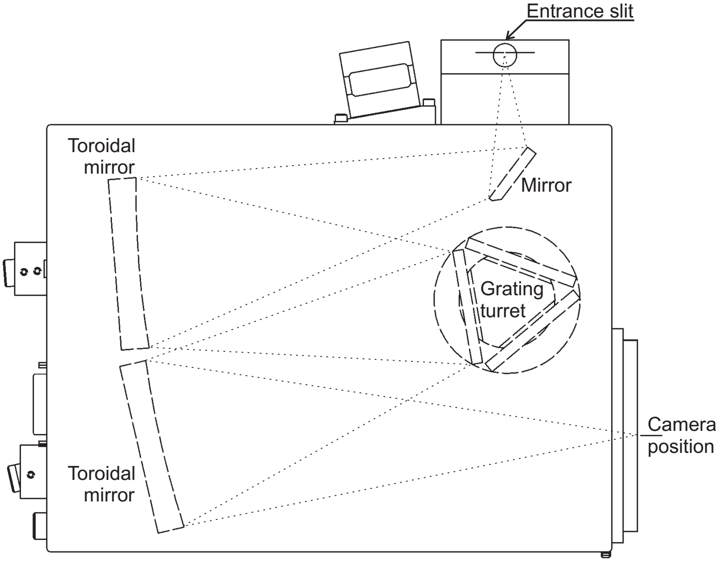

Figure 2.11 Sketch of an Acton 2300i spectrometer. The outline of the light path through the spectrometer is indicated by dotted lines.

A sketch of an Acton 2300i spectrometer can be seen in Figure 2.11. In the configuration used in this work, a PI MAX II ICCD camera (see Section 2.2.1) that was docked to the spectrometer at the lower right corner was used as detector (see Figure 2.11). The Acton 2300i spectrometer can be equipped with three gratings on the grating turret, but only two were used in the present experiments: 300 groves/mm and 1200 groves/mm, both blazed for 300 nm. This setup was initially optimized for Raman spectroscopy using 266 nm laser radiation as the excitation source (see Paper V). The spectral resolutions of the 300 groves/mm and 1200 groves/mm gratings at 300 nm were 0.13 nm/pixel and 0.032 nm/pixel, respectively.

2.3 Optical engines

As stated in the introduction, an increased understanding of the combustion process in internal combustion (IC) engines can be gained by studying engines with optical access. Compared to the static combustion vessels, in which more fundamental combustion studies are usually made, optical engines generally provide a more realistic environment. An optical engine is essentially an engine in which some of the parts have been replaced with “windows” allowing optical access to the combustion chamber. The window can be an optical fibre that only requires a small hole through the cylinder head, or it can be in the form of a full glass piston that provides optical access from below into the combustion chamber.

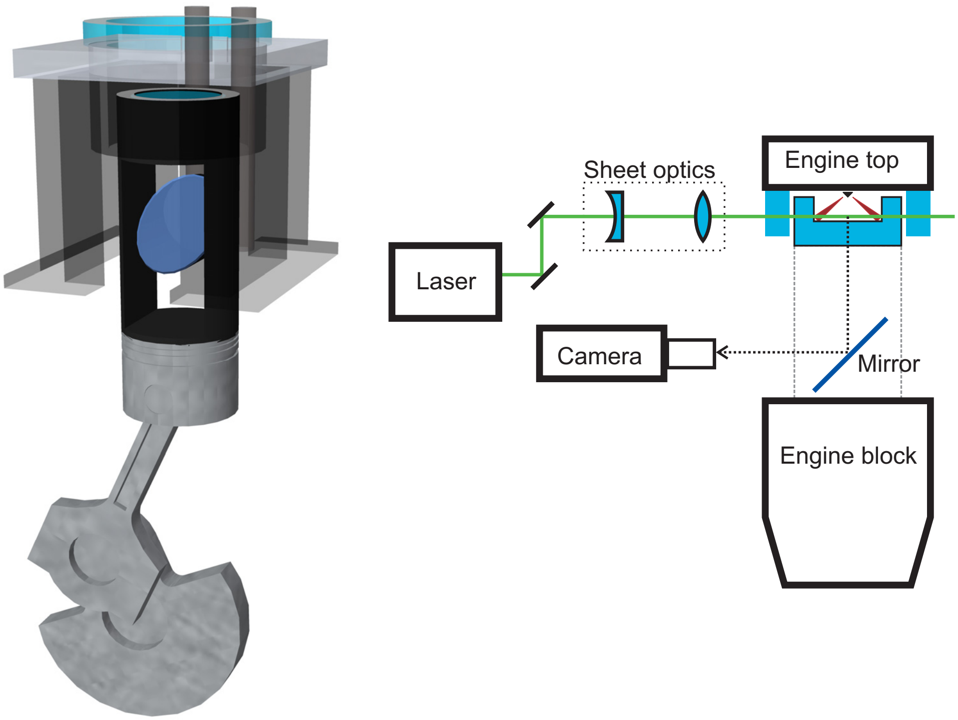

Figure 2.12 Left: 3D illustration of a piston with Bowditch piston extension (black) with support structure and a 45 degree mirror. Right: Simplified sketch of the setup for measurements in an optical direct injection engine using a laser sheet and a camera for imaging.

A common approach for achieving optical access in IC engines is a Bowditch piston extension [29]. This takes the form of an elongation attached to the regular piston, see Figure 2.12. The midsection of the elongation is hollow, providing room for a 45 degree mirror that is mounted on the engine block. It is then possible to see into the combustion chamber from below through the transparent parts in the new piston head.

In diesel engines there is usually a bowl in the piston top. An optical piston can have any shape, but complex re-entrant bowl geometries will severely distort the recorded images and make measurements with laser sheets more difficult. Furthermore, the sharp edges can generate elevated levels of local thermal stress that might damage the quartz component. The optical piston can be supplemented with optical access through the combustion chamber walls. Either small windows (usually four windows positioned symmetrically around the chamber) or a full optical liner can be used.

Physical access to the combustion chamber, for cleaning of the optical components, is gained through a drop-down liner around the piston elongation. A consequence of this design is that the piston rings are mounted very low on the piston skirt so that they do not pass above the top rim of the drop-down liner or even worse, traverses the quartz liner/windows in the combustion chamber walls.

A general rule of thumb is that the larger the quartz component the more fragile it is. The use of large optical components usually limits the operating range of the engine to lower loads. However, a full optical liner gives unsurpassed optical access to the combustion chamber and in some applications this is necessary. If the quartz liner can be avoided, this is recommended as it tends to be the weakest component in the setup and is prone to failure. Catastrophic failure of optical parts in engines can be caused by a number of factors. One is misalignment, which is usually detected immediately after assembly and can be rectified if caught before starting the engine. However, as optical components are fastened with floating gaskets, i.e. they are not in direct contact with the metallic parts of the engine they can slide over time. This is mostly a problem when using full quartz liners, which can slide into the path of the piston and be destroyed.

Another problem associated with optical components is fatigue. Cyclic loads with high temperature and pressure gradients are unavoidable in optical combustion engines. These lead to material fatigue that can cause a quartz component to break for no apparent reason after some time of use. This limits the life-time of optical components. Small optical parts with simple geometries seem to be less prone to failure due to fatigue.

Too high temperatures also tend to lower the operational lifetime of optical parts. For each application it is recommended that a maximum temperature is selected and that this is not exceeded in order to avoid breakage. A thermocouple, pressed against or glued to the outside of the quartz liner is recommended. If this is not possible, a thermocouple can be positioned in the plate below the quartz liner, but the time lag between the temperature rise of the plate and the optical parts that are in direct contact with the combustion chamber must be taken into account.

All modifications to an engine change the characteristics of the combustion process, some more than others. It has, however, been shown that most of the changes can be related to the difference in heat conduction between metal and quartz, and that these can be compensated for by changing the inlet temperature [30]. It is an interesting fact that the same study showed that engines with optical parts exhibited better combustion efficiency than the equivalent engines with metal parts.

2.3.1 Laser synchronization

One aspect of measurements involving lasers and optical engines is that both run on fixed time scales that are not readily synchronized. To facilitate the synchronization of the laser to the engine a phasing system can be used.

First, the laser is started in synchronization with the clock of the phasing system that is running at 10 Hz. The engine is then allowed to rev up and stabilize at the correct revolution speed, usually 1200 rpm. The engine rig thus sends a signal with a frequency of 10 Hz to the phasing system. The phasing system then shifts the output frequency to the laser to 9.9 Hz. This allows the timing of the laser pulse to slowly glide in time relative to the engine pulse. When the two pulses are synchronized, within given tolerances, the output pulse is changed to a duplicate of the incoming pulse.

If the incoming frequency falls outside the tolerances in the phasing system, the output signal is immediately returned to its internal clock. It then waits for the engine to return to 10 Hz (1200 rpm) before starting a new phasing procedure. As the tolerances set in the phasing system are more stringent than in the laser system, this setup allows the laser to operate continuously even if the engine is not stable or reliable for some reason.

2.3.2 Scania D12 optical engine

Figure 2.13 shows photographs of the heavy-duty Scania D12 optical engine in the Gendies Lab at Lund University. This engine can be operated in a variety of configurations, from a full metal configuration to a configuration with a quartz liner and an piston top made entirely of quartz.

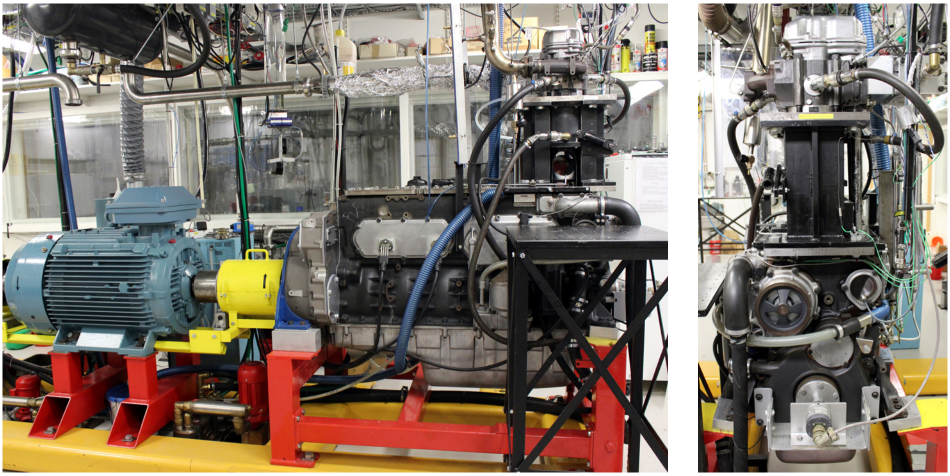

Figure 2.13 Photographs of the D12 engine rig in the Gendies Lab at Lund University. The left image shows a side view of the electrical motor and the diesel engine with a Bowditch piston extension. The right image shows a head-on view of the same D12 engine.

The engine is operated on one cylinder. The other five pistons are deactivated by drilling through the pistons to prevent compression work. Tungsten weights, matching the weight of the Bowditch piston extension, are added to the pistons to re-establish mass balance and thus minimize vibrations. The lower part of the engine is otherwise essentially unmodified. An electric motor, seen to the left in Figure 2.13, functions as a starter motor and a brake at higher loads. The electrical motor also maintains the revolution speed of the system, measured by a crank shaft encoder with 0.2 CAD (crank angle degree) resolution.

The optical configuration used in the later measurement campaigns had a piston crown made of a single piece of quartz, which was glued to the metal piston extension. The bowl in the crown had a cylindrical geometry with straight vertical walls in order to allow a laser sheet to enter the bowl more easily. The piston diameter was 126 mm and the bowl was 83.5 mm in diameter and 14 mm in depth. The diesel injectors used varied extensively from symmetrical eight-hole injectors, similar to those used in the production models, to asymmetrical, four-hole injectors with small orifices.

2.3.3 Volvo D5 optical engine

A light duty optical engine rig based on a Volvo D5, modified to provide optical access, is shown in Figure 2.14. Apart from the modifications giving optical access, this engine also has a fully flexible pneumatic valve train. This allows the four valves to open and close individually with almost any timing. This system can, for instance, be used to study the effects of post-combustion gases that are trapped in the cylinder, so-called internal exhaust gas recirculation (EGR). Rebreathing of exhaust gases from the exhaust manifold is also possible. The actual timing of the valves was monitored using an ICCD camera imaging the valve lift through the full quartz liner.

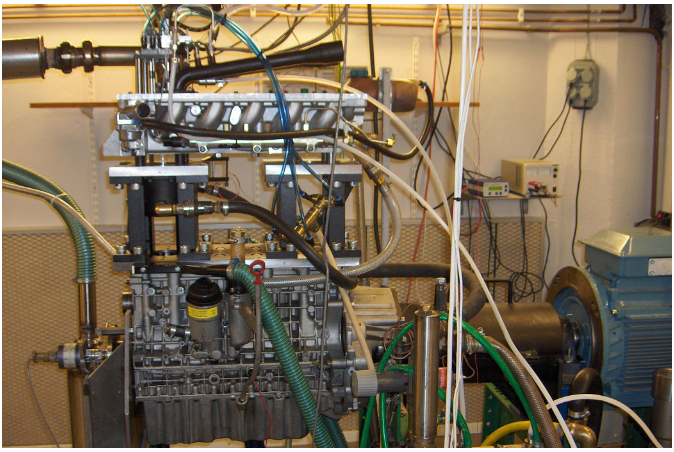

Figure 2.14 Single-cylinder optical engine based on a Volvo D5 engine with a Bowditch piston extension on the cylinder on the far left. This engine was also equipped with a fully flexible pneumatic valve train.

2.4 Laser sheet imaging

Laser sheet imaging is a 2D imaging technique whereby a thin slice of a transparent object is illuminated by a laser pulse and the signal is collected at right angles. It is by no means a new technique [31], but still very much in use in combustion diagnostics. Figure 2.15 illustrates a general laser sheet imaging setup.

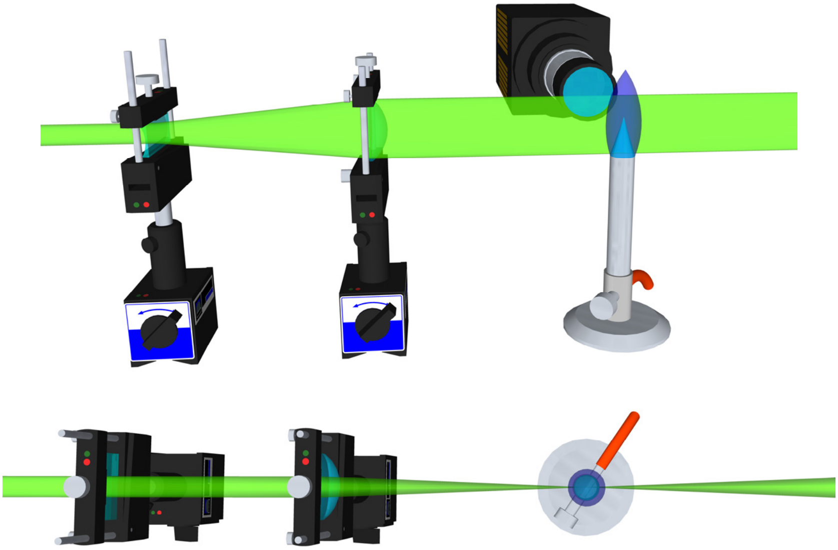

Figure 2.15 Laser sheet setup seen from the side (above) and from above (below).

The laser beam is first expanded in the vertical direction using a cylindrical lens, and then collimated using a spherical lens. In order to obtain a collimated laser sheet, the focal points of the two lenses should overlap. Note that most lenses have shorter focal distances than specified for UV wavelengths as the refractive index of e.g. quartz is slightly wavelength dependent.

Using a spherical lens also focuses the laser beam in the horizontal direction, see Figure 2.15, thus creating a thin laser sheet that bisects the measurement region. The signal is usually imaged at right angles using an ICCD camera.

The shape of the beam waist is dependent on the focal length of the spherical lens. A short focal length gives a thin but short beam waist, suitable for high-resolution imaging over a small area. A long focal length gives a thicker beam waist that does not expand as quickly, which is useful when imaging larger areas. For greater flexibility, two cylindrical lenses, one horizontal and one vertical, can be used instead of the spherical lens. Using three cylindrical lenses decouples the laser sheet height and the focal distance/beam waist shape.

Chapter 3 Methods

This chapter describes the measurement techniques used in the work presented in this thesis. First, absorption measurements will be briefly covered, mainly as an introduction to the following sections on Raman spectroscopy and laser induced fluorescence. The section on LIF describes measurements of different species including fuel tracer LIF. LII and structured laser illumination planar imaging (SLIPI) are also presented. The last section contains a short discussion on the modelling of combustion processes.

3.1 Absorption

Absorption is the loss of incident photons due to interaction with matter. Several diagnostic methods utilize absorption directly for measurements of different species. For example, soot volume fraction can be measured by sending a light beam through a volume and measuring the attenuation. A beam chopper and a lock-in amplifier are usually used in order to discriminate against background light.

Another method used is to send a beam with a tuneable wavelength through the sample. If the wavelength is tuned to an absorption line of a specific species the concentration of this species can be measured very accurately. In the presence of other species that absorb more broadly around the same wavelength, tuning the laser wavelength off the absorption line gives the background contribution, which can then be subtracted from the signal (for stationary conditions at least, i.e. without turbulence).

However, absorption techniques are inherently line-of-sight methods, i.e., the measured signal is the integrated absorption along the entire path of the beam. This averaging effect can be a problem, for instance, when measuring the temperature across a flame front with high temperature gradients. The absorption will be proportional to the number density which follows the Boltzmann distribution. As the Boltzmann distribution is highly non-linear the weighted average number density, and thus the absorption, will not reflect the true average temperature.

3.2 Raman scattering

Raman scattering has an inherent duality, making it both coveted and dreaded among researchers. In theory, it can be used to measure the concentrations of all major species simultaneously, making it possible to determine, for instance, the fuel-air ratio very accurately in a volume of gas with one measurement. The signal is also independent of quenching by other species. However, the signal level is very low, making it difficult to measure anything apart from the major species in a combustion environment.

The complete quantum mechanical treatment of Raman scattering given by e.g. Long [32] is beyond the scope of this thesis and only a more basic description will be given. A shorter review of Raman scattering is also given by Eckbreth [33].

Photons can scatter off molecules elastically, retaining their original energy (Rayleigh scattering), or inelastically, exchanging energy with the molecule in the process. Raman scattering, is created when the incident light exchanges energy with vibrational or rotational energy levels in the molecule, as illustrated in Figure 3.1. Due to the laws of quantum mechanics, the amount of energy exchanged must match the energy difference between the molecule's initial state and another vibrational/rotational mode. For simplicity, only vibrational Raman scattering will be considered here.

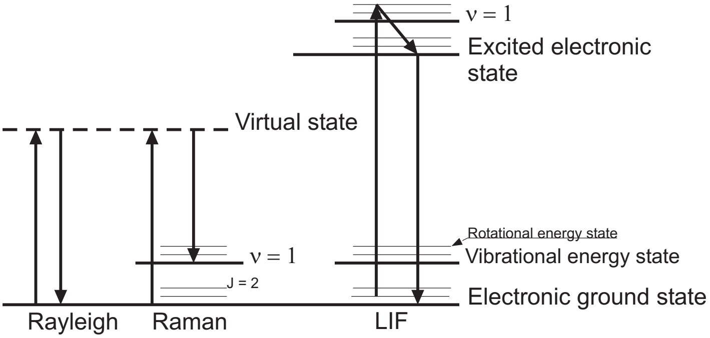

Figure 3.1 Schematic energy level diagram for elastic scattering, i.e. Rayleigh scattering, and inelastic scattering, i.e. Raman scattering, and LIF. In contrast to Rayleigh and Raman scattering, LIF is a resonant technique as the molecule is excited to a higher electronic state.

Diatomic molecules have only one vibrational mode, i.e. the stretching of the bond, while larger molecules have several modes. CO_2 (a linear triatomic molecule) has three fundamental modes: a symmetric stretching mode, an asymmetric stretching mode, and a bending mode. Only the symmetric stretching mode is directly Raman active, but the modes can mix to form additional Raman active modes. For larger molecules, the Raman spectra quickly become very complex. In the case of large hydrocarbons, the C-H stretching mode is usually one of the dominant vibrational modes.

As the photon does not excite the molecule to a higher energy level (as opposed to LIF, see Figure 3.1) the choice of laser wavelength is not critical and any wavelength can be used. This also implies that all species in the sample (and indeed all Raman-active modes) will be excited by the same laser pulse. Thus, multiple species can be detected in one measurement. The only requirements for the detection of multiple species are that the signals from the different molecules do not completely overlap and, of course, that the signal intensity is sufficient.

The Raman signal can be expressed according to Equation (3.1) where I_0 is the incident laser intensity [Wm^{-2}], N is the species number density [m^{-3}], $\partial\sigma/\partial\Omega$ is the Raman cross section [m^2], Ω is the collection solid angle determined by the optics [-], l is the length of the measurement region [m], A is the cross sectional area of the laser beam [m^2] and ε is the collection efficiency of the measurement [-].

$$I_{Raman} = I_0 N \frac{\partial\sigma}{\partial\Omega} \Omega l A \varepsilon \tag{3.1}$$

The Raman signal can be expressed in terms of the Raman shift and the Raman strength. The Raman shift is the spectral distance between the laser wavelength and the Raman peak in cm^{-1}. This corresponds to the energy that the molecule has absorbed from (or given to) the photon. The Raman strength is the intensity of the peak and is commonly given in relative terms, i.e. relative to the strength of the N_2 Raman signal. This approach applies to diatomic molecules with only one vibrational mode but can, to a certain degree, be extrapolated to larger molecules with more complex Raman spectra. However, for larger molecules the population of the different vibrational modes can vary, e.g. with temperature, effectively changing the relative Raman strengths.

The Raman shift and relative Raman strength for the most relevant species in hydrocarbon combustion systems are given in Table 3.1. The Raman strengths are given relative to N_2 for excitation with 532 nm radiation at room temperature and pressure (RTP).

Table 3.1 Raman shifts and relative Raman strengths for molecules relevant in combustion studies. The Raman strengths are given for 532 nm excitation at RTP relative to the Raman strength for N_2 [33, 34].

Molecule	**Raman shift (cm^{-1})**	**Relative Raman strength for 532 nm excitation at RTP**
N_2	2331 cm^{-1}	1
O_2	1556 cm^{-1}	1.41
Hydrocarbons, C – H stretching mode	2903 cm^{-1}	-- (Molecule dependent)
H_2O	3652 cm^{-1}	1.96
CO_2	1388 cm^{-1} (ν_1) 1285 cm^{-1} ($2\nu_2$)	0.98 1.3

In general, the Raman cross section varies with the laser frequency according to Equation (3.2). Thus, the Raman signal strength increases with decreasing laser wavelength for all species. One possible solution to the low signal strength is thus to use UV laser beams, e.g. 266 nm from a Nd:YAG laser. Decreasing the wavelength from 532 nm to 266 nm would theoretically increase the signal strength by a factor of 16. However, it is much more difficult to generate the same laser energy in the UV region as is readily available in the visible region. Also, high-energy UV laser pulses are more likely to cause photo-induced chemistry, background LIF signals and damage to optical components.

$$\frac{\partial\sigma}{\partial\Omega} \propto (\upsilon_{\text{laser}} - \upsilon_{\text{shift}})^4 \tag{3.2}$$

Due to resonance effects with electronic energy levels, the relative Raman signal strength for certain species can also vary with excitation wavelength. O_2, for instance, has resonances that increase the signal when using UV lasers, changing the relative cross section (relative to N_2) to 2.0 for 266 nm excitation (from 1.41 for 532 nm excitation) [35].

A common way to increase the Raman signal to acceptable levels is to use a high-energy laser, but problems such as optical breakdown in the measurement region and damage to optical components then arise. One solution to these problems is to use a pulse stretcher. This splits the pulse into several segments separated in time, thus significantly lowering the peak fluence, while the same total energy is sent through the sample. A drawback of pulse stretchers is that they usually cause deterioration of the beam profile, producing hot spots, which can also cause damage to optical components or breakdown in the measurement region. Also, a fraction of the energy is always lost in the pulse stretcher due to reflections, absorption or imperfect mirrors.

An alternative to using an optical pulse stretcher, is to use a multi-YAG laser system as a natural pulse stretcher, producing eight laser pulses under a very short time period. Furthermore, the multi-YAG laser can be readily optimized for 266 nm generation yielding high pulse energies, which will also further increase the weak Raman signal.

3.3 Laser-induced fluorescence

3.3.1 Theory

Following the notation of Eckbreth [33], LIF in small species can be described, to a first approximation, by a simple two level system, as illustrated in Figure 3.2.

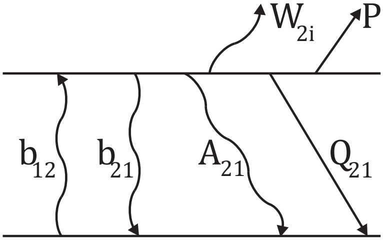

Figure 3.2 The two-level approximation for LIF with various rate constants.

The rates at which absorption and stimulated emission take place are denoted b_{12} and b_{21}, respectively. These depend linearly (in this approximation) on the incident laser field. A_{21} is the spontaneous emission rate constant, while W_{2i} and P are the photoionization and predissociation rate constants. Finally, Q_{21} represents the collisional quenching rate constant. The processes outlined in Figure 3.2 can be formulated as changes in population for the two levels as expressed in Equation (3.3), where N_1 and N_2 are the populations in the lower and upper levels, respectively.

$$\begin{aligned} \frac{dN_1}{dt} &= -N_1 b_{12} + N_2\,(b_{21} + A_{21} + Q_{21}) \\ \frac{dN_2}{dt} &= N_1 b_{12} - N_2\,(b_{21} + A_{21} + Q_{21} + P + W_{2i}) \end{aligned} \tag{3.3}$$

The fluorescence signal, F, is proportional to N_2A_{21}. Calculating N_2 from Equation (3.3) assuming that the populations in both levels have reached a steady state and that W_{2i} and P are very small, gives Equation (3.4), where N_1^0 denotes the population in the lower level prior to excitation.

$$\mathrm{N}_2 = N_1^0 \frac{\mathrm{b}_{12}}{\mathrm{b}_{12} + \mathrm{b}_{21}} \frac{1}{1 + \frac{\mathrm{A}_{21} + \mathrm{Q}_{21}}{\mathrm{b}_{12} + \mathrm{b}_{21}}} \tag{3.4}$$

Defining the saturation energy according to Equation (3.5) gives the relationship for the fluorescence signal power, F, seen in Equation (3.6) where hν is the energy of the photons emitted by the laser, $\Omega/4\pi$ is the collection solid angle, l and A are the length and area of the active volume determined by the laser sheet and detection optics and I_ν is the laser energy.

$$I_{sat} = \mathrm{c} \frac{\mathrm{A}_{21} + \mathrm{Q}_{21}}{\mathrm{b}_{12} + \mathrm{b}_{21}} \tag{3.5}$$

$$\mathrm{F} = h\nu \frac{\Omega}{4\pi} l\, A\, N_1^0 \frac{\mathrm{b}_{12}}{\mathrm{b}_{12} + \mathrm{b}_{21}} \frac{1}{1 + \frac{I_{sat}}{I_\nu}} \tag{3.6}$$

Other assumptions can be made to solve Equation (3.3) analytically. Those most commonly used in practical applications assumes that the transition is completely saturated. More detailed information can be found in [33].

3.3.2 OH LIF

OH is one of the most commonly used species in combustion diagnostics, mainly because of its ease of use, i.e. low interference from other species, and the good availability of laser sources, e.g. dye lasers with SHG. Other reasons are the high signal strength and the high quality of the information that can be obtained from OH LIF measurements.

OH is generally formed through high-temperature reactions in a flame and is thus a rather good flame front marker for atmospheric flames. It also serves as a marker of high-temperature zones in engines utilizing low-temperature combustion concepts, such as homogeneous charge compression ignition (HCCI).

OH is usually excited through the A←X (v′=1←v″=0) electronic-vibrational transition. This requires a laser wavelength around 284 nm. Additional excitation schemes include higher vibrational levels in the same electronic band, e.g. A←X (v′=2←v″=0), but the A←X (v′=0←v″=0) band at 308 nm can also be used. Other electronic levels can be used but the signal strength is lower.

After excitation of the A←X (v′=1←v″=0) transition, rapid vibrational and rotational energy transfer in the excited level cause most of the fluorescence signal to be emitted in the A→X (v′=0→v″=0) band, around 308 nm. An interference filter centred at 310 nm is usually employed do discriminate against scattered laser light and flame luminescence. Alternatively, a UG11 Schott filter (band pass 270 – 380 nm) can be used.

3.3.3 CH LIF

The fluorescence signal strength from CH is generally low, mainly due to the very low concentrations of CH in most combustion applications. Excitation can be achieved using either the A←X, B←X or C←X electronic transitions. The C←X transition is highly predissociative and thus seldom used. One option is excitation of the band head in the R-branch of the B←X (v′=1←v″=0) transition around 387 nm. Another option is excitation of the A←X (v′=0←v″=0) transition at 431 nm [36].

Similarly to OH LIF, the fluorescence is mostly emitted through the A→X (v′=0→v″=0) transition around 431 nm. However, both the A→X (v′=1→v″=1) and the B→X (v′=0→v″=1) transitions are spectrally close to 431 nm and any fluorescence emitted from these bands is usually also detected at the same time, especially for excitation of energetically higher levels.

3.3.4 CO LIF

CO LIF differs from OH and CH LIF in that the energy levels that can be used for LIF measurements require wavelengths below 200 nm. This is problematic in normal flames due to the broadband absorption of air [37]. One option is thus two-photon excitation. Two-photon excitation implies that the molecule, in this case CO, is first excited to a virtual level through the absorption of one photon. Before the molecule relaxes to the ground state a second photon is absorbed, giving the molecule enough energy to become excited into a higher electronic energy level. An energy level diagram of CO is shown in Figure 3.3 where some possible transitions are indicated.

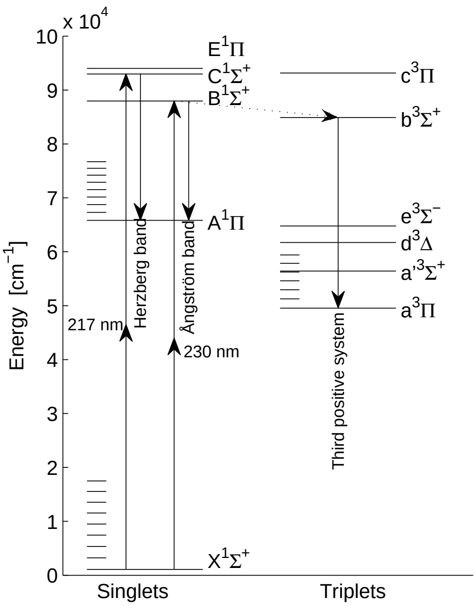

Figure 3.3 Energy level diagram for CO. Two commonly used excitation wavelengths for CO LIF, 230 and 217 nm, and the corresponding emission bands are shown

The most common excitation wavelength is 230.1 nm, corresponding to the $B^1\Sigma^+ \leftarrow X^1\Sigma^+$ transition. The fluorescence from the $B^1\Sigma^+ \rightarrow A^1\Pi^u$ transition, called the Ångström band (400 nm – 600 nm), is then detected [38]. 217.5 nm excitation of the $C^1\Sigma^+ \leftarrow X^1\Sigma^+$ transition with subsequent fluorescence, $C^1\Sigma^+ \rightarrow A^1\Pi^u$, i.e. the Herzberg band (360 – 600 nm), has also been demonstrated [39].

It is potentially also possible to use the fluorescence signal from the $b^3\Sigma^+ \rightarrow a^3\Pi$ transition (282 – 380 nm). The $b^3\Sigma$ triplet state is energetically close to the $B^1\Sigma^+$ singlet state and can be populated through collisions from this level after excitation with 230.1 nm radiation.

3.3.5 Formaldehyde, CH_2O, LIF

The formaldehyde molecule, CH_2O, is an intermediate combustion species. It is formed early in the chain of reactions in hydrocarbon combustion and can be used as an indicator of low-temperature reactions in e.g. HCCI engines [40].

The absorption spectrum that is useful in combustion applications consists of vibrational bands covering a wavelength range from 250 to 360 nm [41]. Due to a fortunate overlap between several weak rotation lines in the absorption spectrum and the wavelength from a frequency tripled Nd:YAG laser, i.e. 355 nm, this is a feasible option for excitation. The formaldehyde LIF signal is emitted in several vibrational bands covering 350 – 550 nm [42].

Unfortunately, the same laser wavelength that is required for formaldehyde excitation also excites several polyaromatic hydrocarbons (PAHs). An on-off resonance technique would be required to distinguish between these two signals. This technique requires tuneable lasers and the recording of two images: one in which the laser is tuned to an absorption line and one in which the laser is tuned off the line. As PAH absorption is usually smooth and broadband both images will contain the same contribution from PAH LIF. The PAH LIF signal can then be subtracted from the on-resonance image, isolating the formaldehyde LIF signal. The formaldehyde absorption peak ($2^0_0 4^1_0$) at 354 nm is fairly isolated [41] and can be used for on-off resonance measurements.

Figure 3.4 shows two LIF emission spectra from a Bunsen burner flame, one where the laser is tuned to the formaldehyde absorption line and one where it is tuned slightly off the resonance. The laser was a dye laser (see Figure 2.4) using Pyridine 1 pumped by 532 nm light from one of the lasers in the multi-YAG system to produce a wavelength of 708 nm, which was frequency doubled to give 354 nm. The band structure of formaldehyde is clearly seen in the on-resonance measurement, while mainly the PAH contribution can be seen in the off-resonance measurement.

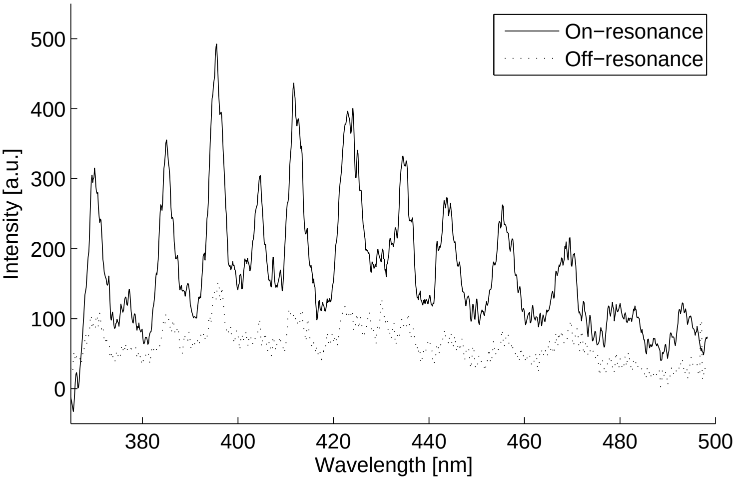

Figure 3.4 Formaldehyde LIF emission spectra from a Bunsen burner flame. The dye laser wavelength was tuned on and off the main absorption peak at 354 nm.

3.3.6 Fuel tracer LIF

Planar LIF is a relatively common way to determine the fuel distribution in combustion engines. Most commercial fuels contain species that can be used for fluorescence measurements. It is thus possible to directly measure the distribution of e.g. diesel, kerosene and gasoline in an optically accessible combustion engine [43].

However, the detected distribution might not show the true fuel distribution. Naphthalene, for instance, is one of the major contributors to the LIF signal from gasoline, and as the boiling point of naphthalene is in the top part of the boiling curve for most gasoline blends, the total LIF signal might not reflect the actual fuel distribution. Furthermore, when several species with different transport and evaporation properties as well as different quenching and fluoresce properties fluoresce at the same time, quantification of the fluorescence intensities to obtain local equivalence ratio values is extremely difficult. LIF measurements of real fuel are thus most often limited to qualitative measurements.

A solution to these problems is to use fuel tracer LIF. This technique simplifies the situation in that a single fluorescent tracer is added to a non-fluorescing base fuel. This allows control of the tracer concentration and simplifies the pressure and temperature dependencies of the signal. A comprehensive summary of quantitative fuel tracer LIF in practical combustion systems can be found in a review by Schulz and Sick [44].

If a slightly more realistic fuel is required, one can use mixtures of a few well-known species that do not fluoresce as a base fuel mix. The tracer added must then follow one of the fractions of the base fuel which are commonly divided into light, medium and heavy fuel fractions [45, 46].

The detected LIF signal, I_{LIF}, can be expressed according to equation (3.7), following roughly the notation of Sahoo et al. [47]:

$$I_{LIF} = \frac{E}{h\nu}\frac{\chi_{tracer}PdV}{kT}\sigma(T,P,\chi,\nu)\eta(T,P,\chi,\nu)\varepsilon \qquad (3.7)$$

where E is the laser fluence [J/m^2], hν is the laser photon energy [J], χ_{tracer} is the mole fraction of the tracer [-], P is the pressure [Pa], dV is the excited volume imaged onto one pixel of the detector [m^3], T is the local temperature [K], σ is the absorption cross section [m^2], η is the fluorescence quantum yield [-], χ represents the local molecular composition [-]and ε is the efficiency of the detector and imaging optics including optical filters [-].

It is sometimes possible to make some assumptions that simplify this equation. For ketones, such as acetone, the dependence of the combined absorption and fluorescence efficiency on pressure is often rather low (at least above 5 bar for acetone [44]), and the dependence on P can thus be disregarded . Furthermore, in non-reacting environments i.e. before the onset of combustion or for very low O_2 concentrations, the variation in local gas composition is rather low. Under these conditions the dependency on χ can also be disregarded as it will be fairly constant over the entire measurement region.

Assuming a stable setup with a constant laser frequency, illuminated volume and detection efficiency finally gives Equation (3.8).

$$I_{LIF} = C\,E\frac{\chi_{tracer}P}{T}\sigma(T)\eta(T) = C\,E\chi_{tracer}P\,F(T) \tag{3.8}$$

Here, C is a constant that can be determined through calibration measurements. For measurements in IC engines, the equivalence ratio (Φ) or corresponding lambda value ($\lambda = \Phi^{-1}$) is commonly the desired quantity. For a fuel with a tracer, Φ is defined according to Equation (3.9).

$$\Phi = \frac{\chi_{fuel} + \chi_{tracer}}{\chi_{air}} \Bigg/ \left(\frac{\chi_{fuel} + \chi_{tracer}}{\chi_{air}}\right)_{stoichiometric} \tag{3.9}$$

The assumptions that the tracer mole fraction is known relative to the fuel and that no other species than fuel, air and tracer exist in the cylinder can be expressed mathematically according to Equation (3.10). This assumes that there is no EGR and that the tracer follows the fuel perfectly through the injection and mixing stages.

$$\begin{gathered} \chi_{tracer} = \mathrm{a}\,\chi_{fuel} \\ 1 = \chi_{fuel} + \chi_{tracer} + \chi_{air} \end{gathered} \tag{3.10}$$

Usually, the fraction of tracer, a, is small; 10% tracer per unit volume is commonly considered a high tracer concentration. From the above equations (Equation (3.10)) it is possible to write the air mole fraction as a function of the tracer mole fraction, as in Equation (3.11).

$$\chi_{air} = 1 - \left(1 + \frac{1}{a}\right)\chi_{tracer} \tag{3.11}$$

Combining Equations (3.10) and (3.11) with Equation (3.9) gives the equivalence ratio in terms of the mole fraction of the tracer.

$$\Phi = \frac{\left(1+\frac{1}{a}\right)\chi_{tracer}}{1-\left(1+\frac{1}{a}\right)\chi_{tracer}} \Bigg/ \left(\frac{\chi_{fuel}+\chi_{tracer}}{\chi_{air}}\right)_{stoichiometric} \tag{3.12}$$

Rewriting Equation (3.12), gives the tracer mole fraction as a function of the equivalence ratio.

$$\chi_{tracer} = \frac{\Phi}{\left(1+\frac{1}{a}\right)\left[\left(\frac{\chi_{fuel}+\chi_{tracer}}{\chi_{air}}\right)^{-1}_{stoichiometric}+\Phi\right]} \tag{3.13}$$

In some cases Equation (3.13) can be linearized as in Equation (3.14). This assumes that the equivalence ratio is much smaller than the inverse of the stoichiometric fuel-air ratio.

$$\chi_{tracer} \approx \frac{\Phi}{\left(1+\frac{1}{a}\right)\left[\left(\frac{\chi_{fuel}+\chi_{tracer}}{\chi_{air}}\right)^{-1}_{stoichiometric}\right]} \tag{3.14}$$

The validity of the linearization in Equation (3.14) is easily tested. The inverse of the stoichiometric fuel-air ratios for some of the commonly used fuels in fuel tracer LIF studies are given in Table 3.2.

Table 3.2 The inverse of the stoichiometric fuel-air ratio for some fuel blends with air as oxidizer. The tracer, acetone, is added at 10% by volume, except in the case of methane where 10% by mass was used.

Fuel	**Chemical formula**	$\left(\frac{\chi_{fuel}+\chi_{tracer}}{\chi_{air}}\right)^{-1}_{stoichiometric}$
90% isooctane 10% acetone	C_8H_{18} C_3H_6O	52.4
90% n-heptane 10% acetone	C_7H_{16} C_3H_6O	47.0
90% ethanol 10% acetone	C_2H_5OH C_3H_6O	14.7
90% methane 10% acetone	CH_4 C_3H_6O	9.8

Calculating the fuel tracer mole fraction as a function of equivalence ratio with and without linearization (Equations (3.14) and (3.13), respectively) for the cases in Table 3.2 gives the results shown in Figure 3.5. It is clear that for larger fuel molecules the assumption is fairly accurate, but for smaller fuel molecules the error is large, even at rather low equivalence ratios.

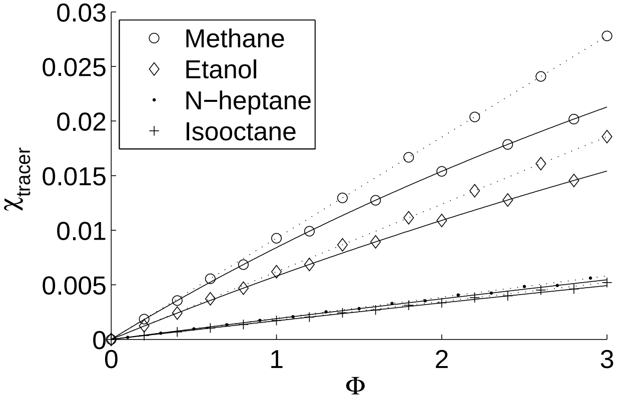

Figure 3.5 Fuel tracer fraction as a function of equivalence ratio for different base fuels with 10% acetone (by mass for methane otherwise by volume), see Table 3.2. The solid lines show the results without linearization, and the dotted lines show the results with linearization.

Using Equation (3.14) together with Equation (3.8), gives a linear relation between the equivalence ratio (Φ) and the detected LIF signal, as can be seen in Equation (3.15).

$$I_{LIF} = C \; \frac{\left(\frac{\chi_{fuel} + \chi_{tracer}}{\chi_{air}}\right)_{stoichiometric}}{\left(1 + \frac{1}{a}\right)} \; \Phi \; E \; P \; F(T) \tag{3.15}$$

$$\Phi = C' \; \frac{I_{LIF}}{E \cdot P \cdot F(T)}$$

The laser energy (E) and the pressure (P) must thus be monitored during the experiments. Calibration measurements with known equivalence ratios and temperatures have to be made in order to obtain C′ and F(T). For direct injection (DI) engines, this usually involves injecting fuel through an additional port fuel injector or injecting fuel very early in the cycle, giving ample time for mixing.

In the calculations above it was assumed that the cylinder contains only air and fuel with tracer. If EGR is used, a more rigorous analysis should be made if the EGR levels are expected to be high or if the EGR levels change during the measurements [48].

Toluene LIF

Toluene is commonly used as a fuel tracer mainly due to the resulting high LIF signal and the possibility of exciting it with common high-power lasers, e.g. the fourth harmonic from a Nd:YAG laser at 266 nm or Excimer lasers at 248 nm. Toluene is also a common component in commercial fuels and can, as such, represent part of the original fuel even though a model fuel is used.

As the absorption by toluene is high toluene LIF can suffer from problems associated with laser attenuation along the measurement volume. The toluene absorption band extends from 270 nm to roughly 230 nm at RTP. At higher temperatures the absorption band is red shifted towards longer wavelengths. For 266 nm excitation the absorption increases with temperature between 300 and 900 K [44].

Toluene fluorescence is broadband and is emitted between 260 and 340 nm with a peak at 280 nm. The fluorescence signal is also temperature dependent and is red shifted at higher temperatures. It should be noted that for 266 nm excitation the fluorescence quantum yield decreases as a function of temperature between 300 and 900 K [44]. The toluene LIF signal is also pressure dependent and careful calibration must be performed in order to discern both the temperature and the pressure dependence in IC engines.

Furthermore, toluene LIF is strongly quenched by oxygen. This is problematic in fuel concentration measurements, and one way of circumventing it is to use a non-reacting atmosphere, i.e. without oxygen, eliminating oxygen quenching altogether. However, this also hinders chemical reactions and care must be taken to ensure the validity of the measurements. This strong oxygen quenching has been suggested as a means of directly measuring the equivalence ratio. The technique is called fuel air ratio LIF or FARLIF, and several papers have been presented on this, e.g. [49] and references in [44]. However, the linearity of this technique has recently been questioned. For practical applications, at high temperatures, the intermolecular, non-radiative decay decreases the importance of oxygen quenching and thus the coupling between the signal and the fuel-air ratio can be undermined [50].

The temperature dependence of both the absorption band and the florescence band can be used for temperature measurements, at least in the absence of oxygen. In a homogeneously seeded gas system, without oxygen, toluene has the potential to be a very good and sensitive temperature probe.

Acetone LIF

Compared to toluene, the ketone acetone is easier to work with in fuel tracer applications. The pressure and temperature dependencies of the absorption cross section and fluorescence quantum yield are lower, and can in some cases be completely neglected, see Equation (3.8).

The absorption band for acetone extends from 320 nm towards the UV with a peak at 280 nm at RTP. The absorption band is further red shifted towards longer wavelengths with increasing temperature. Fast vibrational relaxation to lower vibrational states is responsible for the red-shifted fluorescence signal. The broadband fluorescence is located between 300 and 550 nm with a peak around 400 nm at RTP.

When using 266 nm for excitation the fluorescence signal decreases slightly as a function of temperature. A longer wavelength, around 300 nm, would minimize the temperature dependence over a large temperature interval relevant for combustion studies. The fluorescence intensity of acetone is pressure dependent, but for a wide range of pressures above 5 bar the signal has been shown to be fairly independent of pressure [51].

3.4 Laser-induced incandescence

The LII signal is the blue-shifted light emitted from a particle, usually soot, after it has been heated by a short laser pulse to a temperature significantly higher than that of the surrounding medium. The entire process can be expressed by an energy balance per unit time (see Equation (3.16)) for the particle in question, which contains the following terms: absorption, internal energy, conduction, sublimation and radiation.

$$\frac{\mathrm{dE}_{abs}}{\mathrm{dt}} - \frac{\mathrm{dE}_{int}}{\mathrm{dt}} - \frac{\mathrm{dE}_{cond}}{\mathrm{dt}} - \frac{\mathrm{dE}_{sub}}{\mathrm{dt}} - \frac{\mathrm{dE}_{rad}}{\mathrm{dt}} = 0 \tag{3.16}$$

The absorption term describes the amount of energy absorbed from the incident light field i.e. the laser pulse. As soot has a very broad absorption band (spectrally) virtually any laser can be used. The fundamental, 1064 nm, or the second harmonic, 532 nm, from a Nd:YAG laser are often used.

Absorbing energy from the laser pulse increases the temperature of the soot particle to a level significantly higher than the surrounding medium. This temperature history is expressed in the internal energy of the particle which is the second term in Equation (3.16). As the temperature of the particle increases, the conduction term becomes important as energy is lost to the surrounding medium through collisions with molecules and other particles.

As more and more energy is absorbed by the particle it finally begins to sublimate, releasing small carbon molecules from the surface. These carbon molecules, e.g. C_2 C_3 etc., take with them a substantial amount of energy and mass from the soot particle. Sublimation limits the temperature that the soot particle can reach to around 4000 K, which is substantially higher than that of the surrounding medium in almost all practical applications.

Finally, as the particle temperature increases, the radiation emitted by the particle will also increase, roughly following the Planck radiation law. The radiation is also blue shifted with increasing temperature. It is this blue-shifted radiation that is detected as the LII signal, usually at wavelengths in the UV/blue region where the contribution from flame luminosity (e.g. chemiluminescence and natural soot luminosity) is minimized. An in-depth theoretical discussion regarding these terms and the LII technique in general can be found in [52] and the references therein.

LII is today an established optical diagnostic technique for soot measurements. The peak of the LII signal, which is essentially simultaneous with the intensity maximum of the laser pulse, has been shown to be proportional to the soot volume fraction (f_v) [53]. This can be used for 2D measurements of the soot volume fraction using laser sheet illumination and an ICCD camera for detection of the prompt LII signal. The decay of the LII signal after the laser pulse, as the particles cool down, can be detected with e.g. a photo multiplier tube. When coupled to suitable LII models, this time-resolved LII signal can give both soot volume fraction and particle size [54]. Time-resolved measurements are, however, usually limited to point measurements.

Measurements of the soot volume fraction using LII are usually conducted at high laser fluence (>0.2 J/cm^2 at 532 nm) where sublimation effects are significant. The reason for this deliberately intrusive approach is that the dependence of the signal on the laser pulse fluence can be minimized. As the peak temperature of the soot particles is limited by the sublimation process and not the laser fluence, it is possible, using a Gaussian laser sheet profile, to achieve a saturation level or plateau regime, where variations in the laser fluence do not affect the intensity of the LII signal yield. However, the shape of the fluence curve depends strongly on the spatial energy profile of the laser sheet and it is possible to obtain a fluence curve without a plateau.

In diesel engines, LII is mostly used to obtain the 2D soot volume fraction [55, 56], but problems associated with laser attenuation, signal trapping, window fouling and beam distortion make it difficult to perform good quantitative in-cylinder measurements. Despite this, quantitative LII measurements have been made relying on calibrating the LII measurements with a known source of soot [57, 58]. However, quantitative soot volume fraction measurements with LII in diesel engines still require compensation for laser attenuation and signal trapping. Using low-sooting fuels can reduce the effects of laser attenuation and signal trapping, but these may still introduce large errors in quantitative measurements [59].

3.4.1 **High-speed LII measurements**

In-cylinder 2D LII imaging usually involves recording a single LII image in each engine cycle. Due to the highly stochastic nature of combustion and fluid dynamics in engines, the results cannot readily be compared between crank angle positions other than by using mean values. High-speed measurements, which enable tracking of the soot development in one cycle, are therefore highly relevant.

In diesel engines, most of the soot mass formed during the combustion phase is oxidized later in the cycle. Hence, the correlation between the amount of soot formed early during combustion and the soot in the exhaust, i.e. the filtered soot number (FSN) may be small. What is needed is a tool to distinguish between the soot formation and oxidation rates in individual engine cycles. In the general case, it is of course not possible to distinguish these rates just by measuring the soot volume fraction, as this depends on both rates simultaneously. However, by tracking the ▯▯▯アパート「
┘‼HYPERLINK \l "_Toc323706184" ¶4.4 High-speed LIIining this information with information on global engine parameters it might be possible to reach a stage at which the information can be correlated to the formation and oxidation rates.

It is especially important to be aware of laser-induced soot sublimation and morphological effects when performing high-speed LII measurements. High-fluence LII is intrinsically intrusive as there is a significant reduction in soot mass in the measurement volume after the laser pulse. Also, graphitization, i.e. a phase transformation from the original amorphous structure to a more graphite-like state with clear shell structures changes the soot particles [60]. These compositional changes, resulting from the rapid heating, are likely to affect the optical and physical properties of the particles (e.g. emissivity, density and heat conduction), and thus the LII signal [61]. When making several LII measurements in rapid succession, there is a risk of multiple measurements being performed on the same soot particles. This would be seen mainly as a decline in soot volume fraction over the consecutive measurements.

3.5 SLIPI

An important issue concerning laser sheet imaging is the background subtraction. Usually, a separate image with the background contribution is recorded and subtracted from the signal image. This can, however, be problematic in environments with heavy scattering where the laser photons and the signal photons will be scattered around in the medium. These effects of multiple scattering are difficult to compensate accurately for. By using Structured Laser Illumination Planar Imaging (SLIPI) it is possible to remove the effects of this scattered light. SLIPI is based on laser sheets that are spatially modulated with a sinusoidal pattern. The modulation can be expressed according to Equation (3.17) where x is the spatial coordinate along the height of the laser sheet, ω is the modulation frequency and p is the phase of the modulation.

$$E_{laser} = E_0\,(1 + \sin(\omega x + p)) \tag{3.17}$$

The detected signal from one modulated laser sheet can then be expressed as in Equation (3.18).

$$I_1 = I_B + I_S[1 + \sin(\omega x + p_1)] \tag{3.18}$$

I_s in Equation (3.18) is the detected amplitude of the modulation and I_B is the contribution to the image that is not modulated, e.g. the background arising from scattering and reflections. In SLIPI measurements the background offset can be divided into three parts:

- The common background that does not originate from the laser, e.g. flame chemiluminescence.
- Laser light that is scattered off walls or particles, i.e. laser light that has lost its modulation before or in the measurement region. This can also give rise to secondary effects such as fluorescence from walls etc.
- Multiple scattering of the signal, i.e. blurring of the signal between the measurement region and the detector due to interactions with particles, walls etc.

Images with a sinusoidal spatial modulation are not very useful. Combining three measurements of the same object with different modulation phases, i.e. the modulation is shifted spatially across the laser sheets, it is possible to reconstruct the image as it would look without the modulation ($I_{Reconstructed}$). If the three phases are equally distributed along a wave, i.e. p = 0°, 120° and 240°, Equation (3.19) can be used. $I_{Reconstructed}$ is mostly used for comparison with normal laser sheet measurements and is just the average of the three images.

$$I_{Reconstructed} = I_B + I_S = \frac{1}{3}(I_1 + I_2 + I_3) \tag{3.19}$$

More significant, however, is that I_s can also be obtained from these three measurements according to Equation (3.20). Equation (3.20) can be derived using standard geometrical formulae starting with Equation (3.18) for the three different phases (p_1 = 0°, p_2 = 120°, p_3 = 240°) [62].

$$I_S = \frac{\sqrt{2}}{3}\sqrt{[(I_1 - I_2)^2 + (I_1 - I_3)^2 + (I_2 - I_3)^2]} \tag{3.20}$$

SLIPI measurements can thus suppress the background from scattered light (I_B) and even secondary fluorescence caused by scattered laser light from the images, to reveal the signal originating directly from the laser sheet. Note that, in an ideal environment without multiple scattering and distortions, $I_{Reconstructed}$ and I_s are identical (see Equation (3.19)). An in-depth description of the SLIPI technique and its applications in spray and combustion diagnostics can be found in the thesis by Kristensson [63].

It is experimentally fairly easy to obtain accurate phases (p = 0°, 120°, 240°) in stable environments. In engine applications, however, it is difficult to maintain them as the movement of the engine induces vibrations in the optical setup. These can cause the lines to shift across the laser sheet, i.e. shifting the phases between the images. For these applications, a new equation with less stringent phase constraints was developed. This equation, Equation (3.21), is based on the work by Cole et al. [64]. Theoretically, any combination of phases is possible but practically the best results were obtained for phase differences between 100 and 140 degrees. This was mostly due to the introduction of higher harmonics in the images that gave some residual line structures when the phases were too far from the ideal phases.

$$I_S = \frac{1}{2\left|\sin\left(\frac{p_1 - p_3}{2}\right)\right|}\left|(I_3 - I_1) + i\left\{\frac{I_1 - I_2}{\tan\left(\frac{p_1 - p_2}{2}\right)} - \frac{I_2 - I_3}{\tan\left(\frac{p_2 - p_3}{2}\right)}\right\}\right| \tag{3.21}$$

Some corrections are necessary to the three images prior to the use of Equation (3.20) or (3.21). The corrections made assume that the signal, I_S, and background, I_B, levels do not change between the images. The only difference between the three images should be due to the different phases. More information regarding the image corrections can be found in [63].

3.5.1 The SLIPI setup

As the SLIPI setup is somewhat different from a normal laser sheet imaging technique (see Section 2.4) it is briefly described here. Figure 3.6 shows an illustration of the experimental setup, reprinted from [63]. The laser beam is first sent through an expanding telescope and a circular aperture in order to obtain a top-hat beam profile before the grating. As sinusoidal gratings are difficult to operate with high-power laser pulses, especially UV pulses, a Ronchi grating is possible to use instead. A Ronchi grating introduces a square wave modulation to the laser beam. Thus, Fourier filtering of the beam after the grating is necessary in order to obtain a sinusoidal modulation with a single frequency.

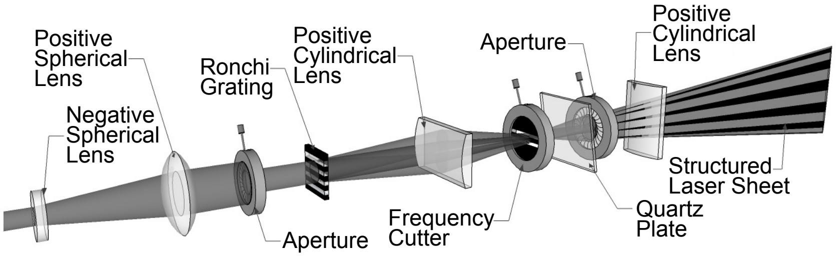

Figure 3.6 Illustration of the experimental setup for SLIPI measurements [63].

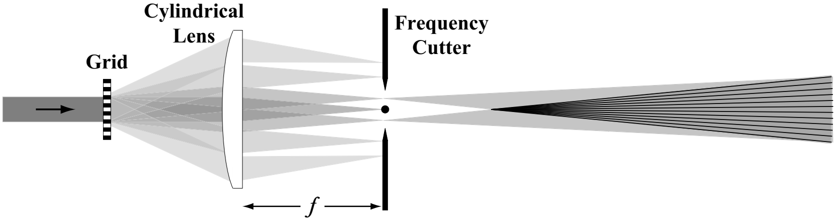

Figure 3.7 Detailed illustration of the grid and the frequency cutter where only the first harmonics (± ω) are allowed to pass. [63]

For this purpose, the beam is first focused using a cylindrical lens, and a frequency cutter is positioned in the focal plane after the lens. The frequency cutter blocks all light except the first harmonics (±ω) from the grating (see Figure 3.7). The frequency cutter consists of a steel wire that block lower frequencies (mainly the zero order) and two razor blades that blocks higher harmonics. All three components are positioned on translation stages with μm precision as their position relative to the laser beam is crucial and very sensitive. As shown in Figure 3.7, the overlap of the two first-order beams will create an interference pattern in the form of a sinusoidal pattern. An aperture is used to remove light outside the overlap region.

A flat quartz plate mounted on a rotation stage is used to parallel translate the entire laser sheet. As the final aperture is positioned after the quartz plate the only relevant contribution of the rotating quartz plate is that the spatial modulation is shifted across the laser sheet. Thus, the three different modulation phases required in Equation (3.21) can be achieved. Choosing the three positions (angles) of the quartz plate to be symmetrical around the incident direction of the laser beam minimizes optical distortions. Thus, at p = 120° the laser beam hits the quartz plate along the surface normal. Finally, a cylindrical lens is used to focus the laser sheet along the non-modulated direction, creating a beam waist in the measurement region.

3.6 Modelling

Computer models that can describe chemical and flow processes in combustion are excellent tools for improving our fundamental understanding of the underlying processes. They can also be used to predict results and can thus be used for optimization.

Several of the papers contained in this thesis include some modelling: from the comparatively simple modelling required for testing that toluene seeding does not significantly alter the internal structure of a laminar flame front (Paper X), to the more comprehensive large eddy simulations of temperature and turbulence effects in HCCI engines (Paper II). Although the modelling in general was performed by others, who are experts in their respective field, this section has been included to help the reader better understand the work presented in the papers.

Three main concepts can be used to model the flows in combustion processes: the Reynolds averaged Navier Stokes (RANS), large eddy simulations (LES) and direct numerical simulations (DNS). All three can be used to solve the Navier-Stokes equations, but take radically different approaches in doing so [65]. A comparison of the advantages and disadvantages of RANS, LES and DNS can be seen in Table 3.3.

Table 3.3 Comparison of the advantages and drawbacks of RANS, LES and DNS

	Advantages	**Drawbacks**
RANS	– Relatively low numerical cost – Coarse grids allow for simulation of large volumes	– Only the mean flow field is resolved – Models required for turbulence
LES	– The most important turbulent features are captured – Reduced modelling impact (compared to RANS)	– Models required for smaller turbulence scales – 3D simulations are costly – Very precise code required
DNS	– No models – Can be used to evaluate other flow models	– Exorbitant numerical cost – Limited to small volumes and “academic” problems

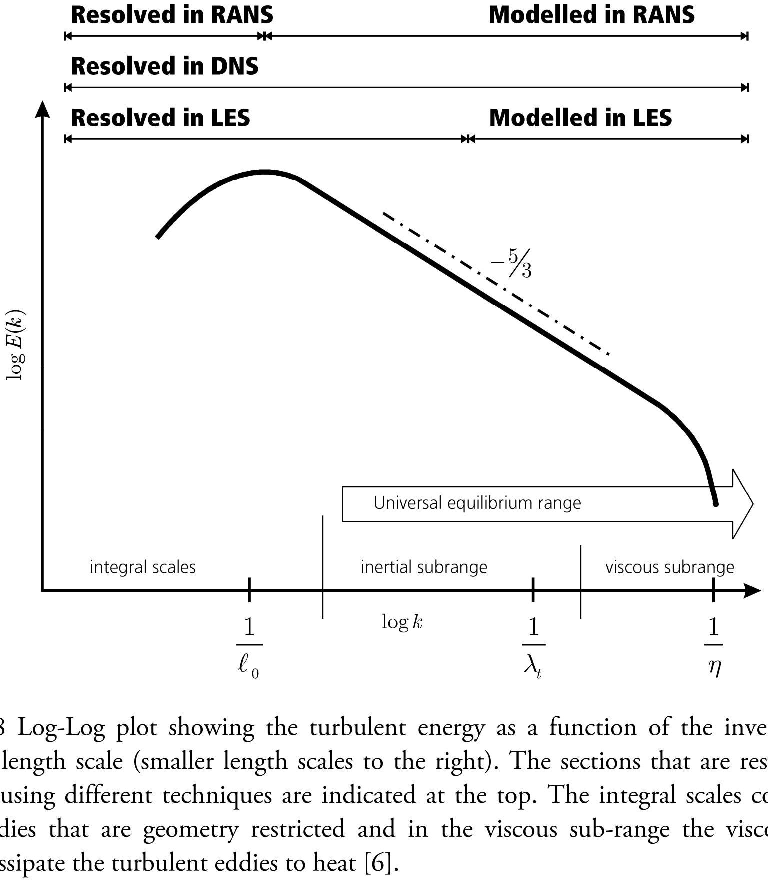

Figure 3.8 Log-Log plot showing the turbulent energy as a function of the inverse of the turbulent length scale (smaller length scales to the right). The sections that are resolved and modelled using different techniques are indicated at the top. The integral scales contain the largest eddies that are geometry restricted and in the viscous sub-range the viscous forces quickly dissipate the turbulent eddies to heat [6].

RANS resolves the mean flow field only. Turbulence effects are only added as submodels that are not spatially resolved. RANS can be applied to large systems as it is relatively cost effective in terms of the required computing power. This can be useful for large parametric studies of, e.g., IC engines, where the exact nature of the turbulence is of less interest. However, effects such as the heat flux to walls and turbulence-chemistry interactions may not be predicted accurately. RANS can also be coupled to rather large chemical models and thus used for the modelling of reacting flows.

DNS, on the other hand, are the diametric opposite of RANS. DNS resolve all turbulence scales, from the largest vortices down to the Kolmogorov scale, where the turbulent energy is dissipated as heat ($1/\eta$ in Figure 3.8). It also resolves the smallest chemical length scales and can be used to follow the internal structure of a turbulent flame front very accurately. This requires very fine numerical grids with high spatial resolution, and thus the simulations are limited to small volumes. This usually limits the use of DNS to "academic" problems where boundary conditions, flow fields and/or chemical conditions can be controlled to some extent.

LES cover the middle ground between the other two techniques. LES resolve larger turbulence eddies and models the smaller length scales, as shown in Figure 3.8. LES are more costly than RANS as the turbulence terms in the Navier-Stokes equations remain. On the other hand, LES can handle much larger systems than DNS. With LES it is, for instance, possible to calculate the turbulent gas flow through an entire engine cycle from intake, via compression to combustion, and finally expansion and gas exchange.

Combustion requires coupling LES to a chemical model that describes the chemical reactions. As LES are fairly costly, a common approach is to use a simplified tabulated chemical model. The chemical state is described by one or two reaction variables and the resulting output (e.g. heat release) from the reactions is looked up in a table for the given parameter set. This significantly accelerates the simulations as all the chemical reactions are not solved for every time step.

Chapter 4 Results – Development of Laser Techniques

4.1 OPO – Multi-YAG

As stated in Section 2.1.5, one option for a high-speed tuneable laser is an OPO coupled to the multi-YAG laser system. Prior to the work presented in Paper IV it was not known how the OPO would react under high repetition rates.

The first test performed was therefore to send two laser pulses through the OPO unit and to vary the temporal separation between the pulses. The combined output energy from both pulses after frequency doubling to 283 nm can be seen as a function of pulse separation in Figure 4.1. The results demonstrated that the OPO unit did not show any significant variation in output power due to changes in pulse separation. The OPO is therefore not limited by depletion effects in the gain medium as are dye lasers. Thus, a single OPO unit could be used to frequency shift all eight pulses from the multi-YAG laser at the same time.

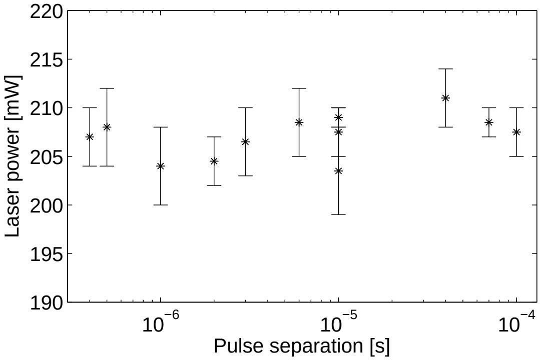

Figure 4.1 OPO output power at 283 nm (after frequency doubling the OPO output beam) as a function of the time between the laser pulses. The error bars indicate the highest and lowest energy detected.

The next step was to apply the OPO for high repetition rate laser diagnostics in combustion environments. OH LIF was selected as a well-known test case. The resulting spectrum from an excitation scan of OH can be seen in Figure 4.2 together with a simulated spectrum which indicated a line width of ~4.2 cm^{-1}.

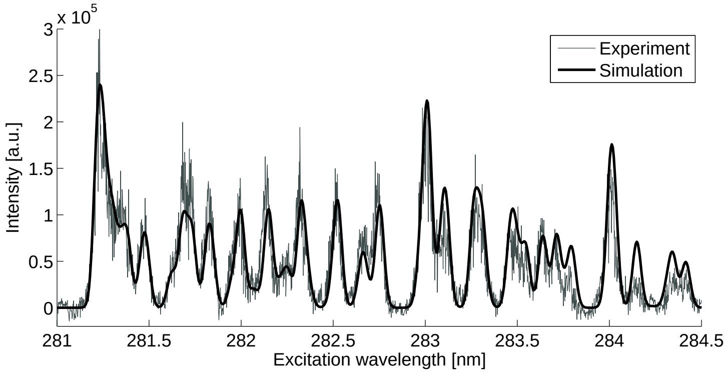

Figure 4.2 Excitation spectrum of OH from 281.1 to 284.5 nm (grey) and simulated spectrum (black).

The OPO was then used for high-speed OH planar LIF (PLIF) using a Bunsen burner and the SIM 8 framing camera. The laser sheet was about 4 cm high, the wavelength was tuned to 282.97 nm and the pulse-to-pulse separation was 139 µs. A sequence of eight images can be seen in Figure 4.3. A background subtraction is the only correction made to the images, which therefore demonstrate the good spatial laser sheet energy profile from the OPO that does not vary significantly over the sequence, either in profile or strength.

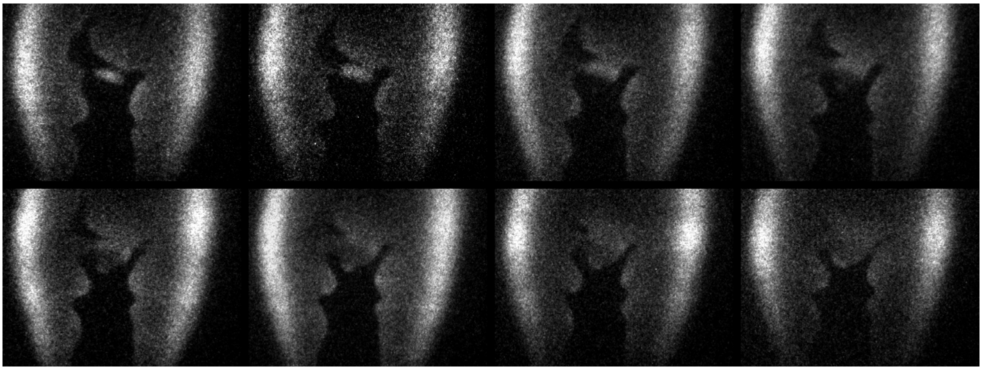

Figure 4.3 Eight OH LIF images obtained using a Bunsen burner. The time between each image was 139 µs and the excitation wavelength was 282.97 nm.

As the initial tests were quite successful, the OPO – multi-YAG system was used for high-speed OH LIF measurements in a high-pressure gas turbine combustor with swirling flow. As the fuel (Jet-A) gave a fluorescence background signal that could not be spectrally or temporally separated from the OH LIF signal, the OPO was used for on – off-resonance measurements of OH LIF. Two resulting series of images can be seen in Figure 4.4. The top series shows on-resonance measurements (OH and fuel LIF contribution) and the bottom series shows off-resonance measurements (fuel LIF contribution only). The two series were not recorded simultaneously but can still be used to qualitatively evaluate the spatial location of the different species.

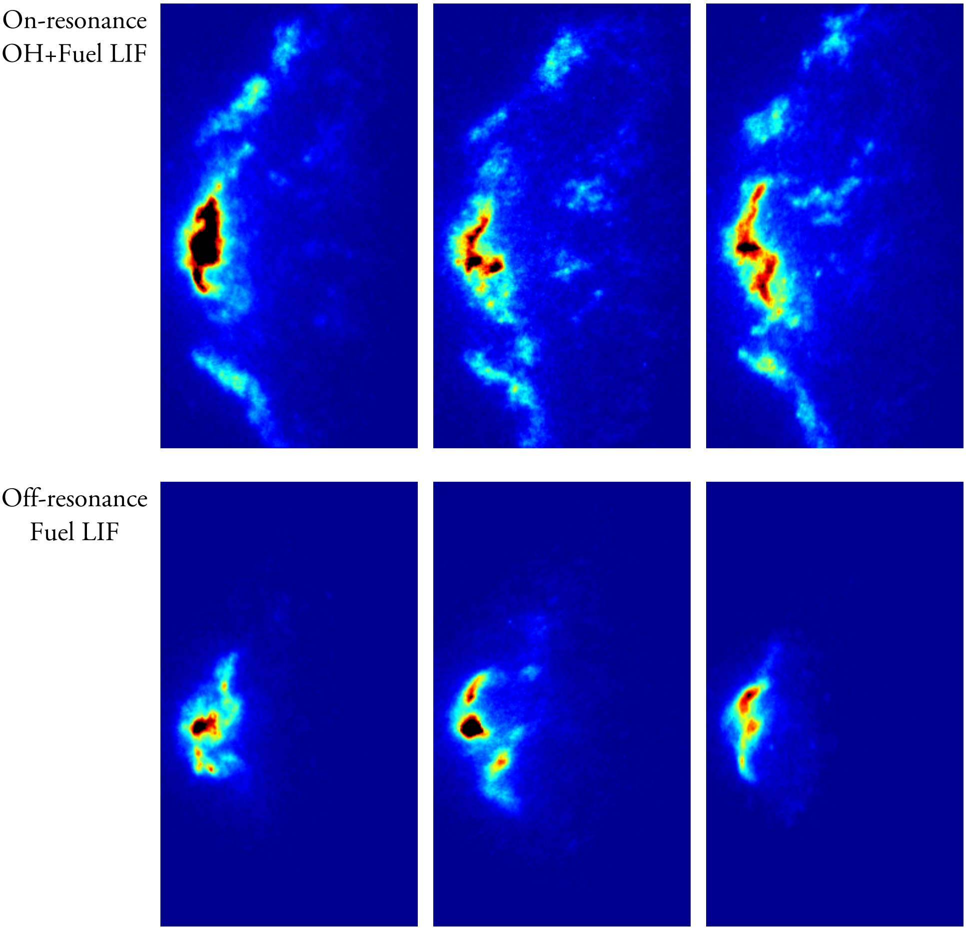

Figure 4.4 High-speed LIF images of OH and fuel LIF (top) and only fuel LIF (bottom) resulting from excitation close to the OH absorption line. The time between frames was 145 µs. The laser sheet enters from below and the burner outlet is positioned to the left of the images.

4.2 Multi-species measurements

Simultaneous measurements of several species are necessary if the interactions between different species in turbulent environments are to be determined. The simultaneous measurement of several species using LIF is by no means a new concept as it can be traced back to the early 1980's [66]. Since then, it has become a fairly common technique for flame visualization, providing information that is otherwise difficult to acquire.

Different combinations involving LIF are often used to correct the LIF signal for, e.g. temperature dependences, through Rayleigh measurements [67]. One approach is to use Raman spectroscopy, a linear technique, to measure the concentrations of all major species allowing for the correction of LIF measurements for varying quenching factors, at least in point measurements [68, 69]. In highly turbulent and wrinkled flames, detecting OH PLIF only can be insufficient for flame front detection. Combining OH and CH can, however, show the position and the orientation of the flame front [70], as well as local flame front extinction [71].

An example of simultaneous LIF measurements is the visualization of the heat release zone in hydrocarbon flames through simultaneous OH and formaldehyde (CH_2O) LIF measurements. Initially, numerical studies indicated good spatial correlation between HCO and the heat release zone in flames. However, as measuring HCO directly is challenging an alternative method was devised based on the major chemical reaction path creating HCO. As this path involves OH and CH_2O, simultaneous LIF measurements of these two species have been used to track the spatial presence of HCO and thus indirectly the heat release zone [72, 73]. Combining OH and CH_2O PLIF with Rayleigh scattering, thus providing an estimate of the temperature field, has also been demonstrated [67, 74].

Previously presented studies on similar turbulent flames to those used in this work have included measurements of simultaneous CH and OH PLIF [75], simultaneous CH and CH_2O PLIF [76], and simultaneous CH_2O and OH PLIF [77]. However, the study presented in Paper X was, to the best of the author's knowledge, the first in which simultaneous 2D measurements using LIF of four species in a flame were made. The selected species gave a rather complete picture of the flame from the unreacted fuel/air mixture (fuel tracer toluene) to the post-flame zone (OH) via the preheating zone (CH_2O) and the high-temperature reaction zones (CH and OH). The experimental setup can be seen in Figure 4.5 and a summary of the wavelengths used for excitation and detection is given in Table 4.1. Further details can be found in Paper X.

Table 4.1 Wavelengths used for excitation and detection in the multi species measurements.

Species	CH	OH	CH_2O	Toluene
Excitation wavelength	431 nm	309 nm	355 nm	266 nm
Detection wavelength	431 ±10 nm	309 ±5 nm	385 – 500 nm	275 – 290 nm

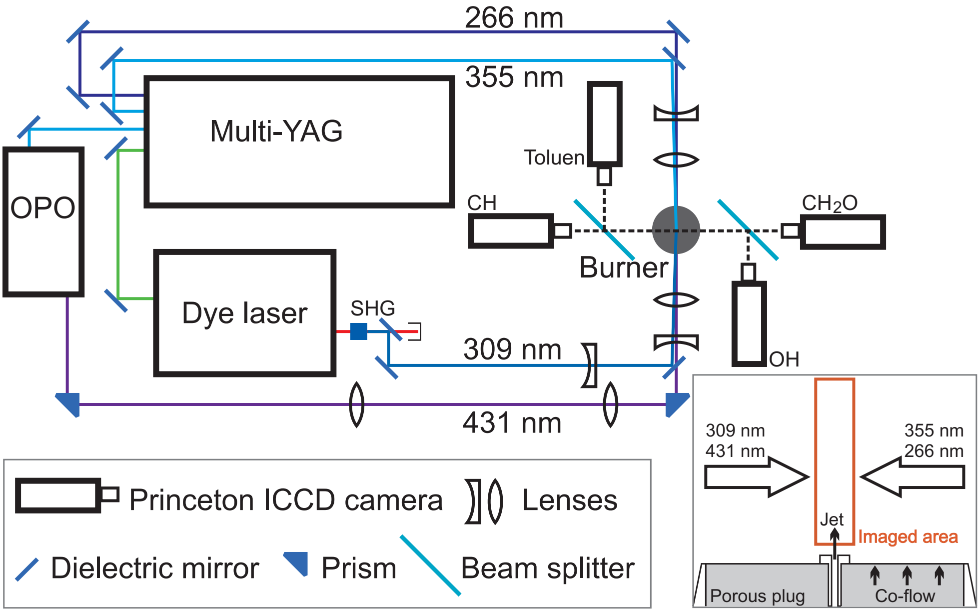

Figure 4.5 Sketch of the optical setup. The insert on the lower right shows the modified McKenna burner (with jet), the imaged area (red square) and the direction of the laser beams.

Four LIF images of OH, CH, CH_2O and toluene, are shown in Figure 4.6. The four images are averages of 100 single-shot LIF images of the laminar, 10 m/s, flame. Note that the background images were recorded with the flat co-flow flame active, which generated a substantial contribution to the signal in the OH background image. Therefore, the OH images (with background subtraction) reflect the increased OH contribution from the jet flame and not the total OH concentration.

The jet flame has an inner core of unreacted premixed gas, as indicated by the toluene LIF image. Surrounding the toluene signal is a thin region of CH_2O indicating the inner flame front and the preheating zone. CH is seen in a narrow band along the flame front, and OH can be seen in the outer flame front and the post-flame gases.

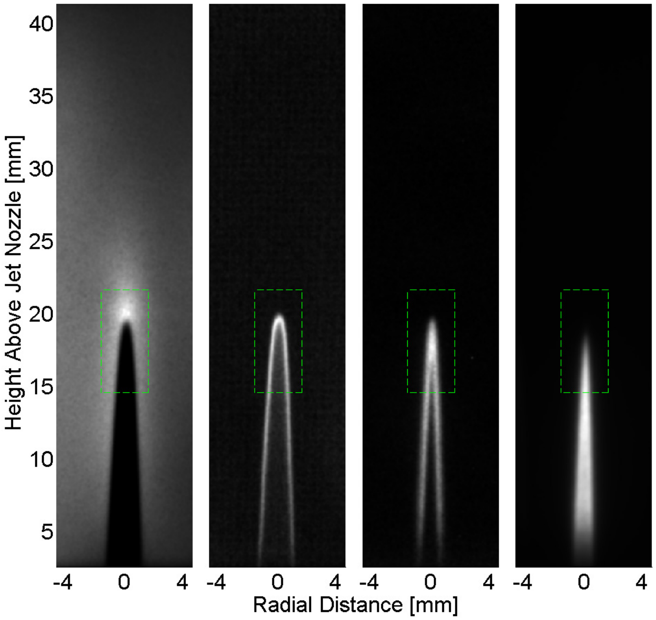

Figure 4.6 Average LIF images (100 shots) of, from left to right, OH, CH, CH_2O and toluene for the laminar, 10 m/s, case. The green dashed lines outline the areas shown in Figure 4.7.

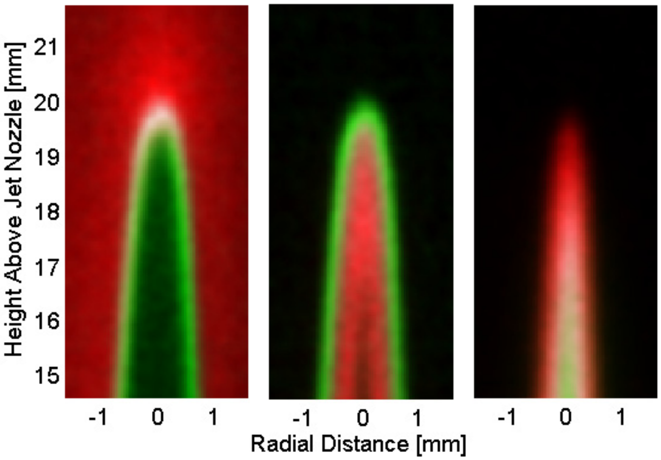

Figure 4.7 Composite images of the laminar flame tip (10 m/s jet flow speed) (see Figure 4.6). Left: OH (red) and CH (green), Middle: CH_2O (red) and CH (green) and Right: CH_2O (red) and toluene (green). The spatial overlap is highlighted in white.

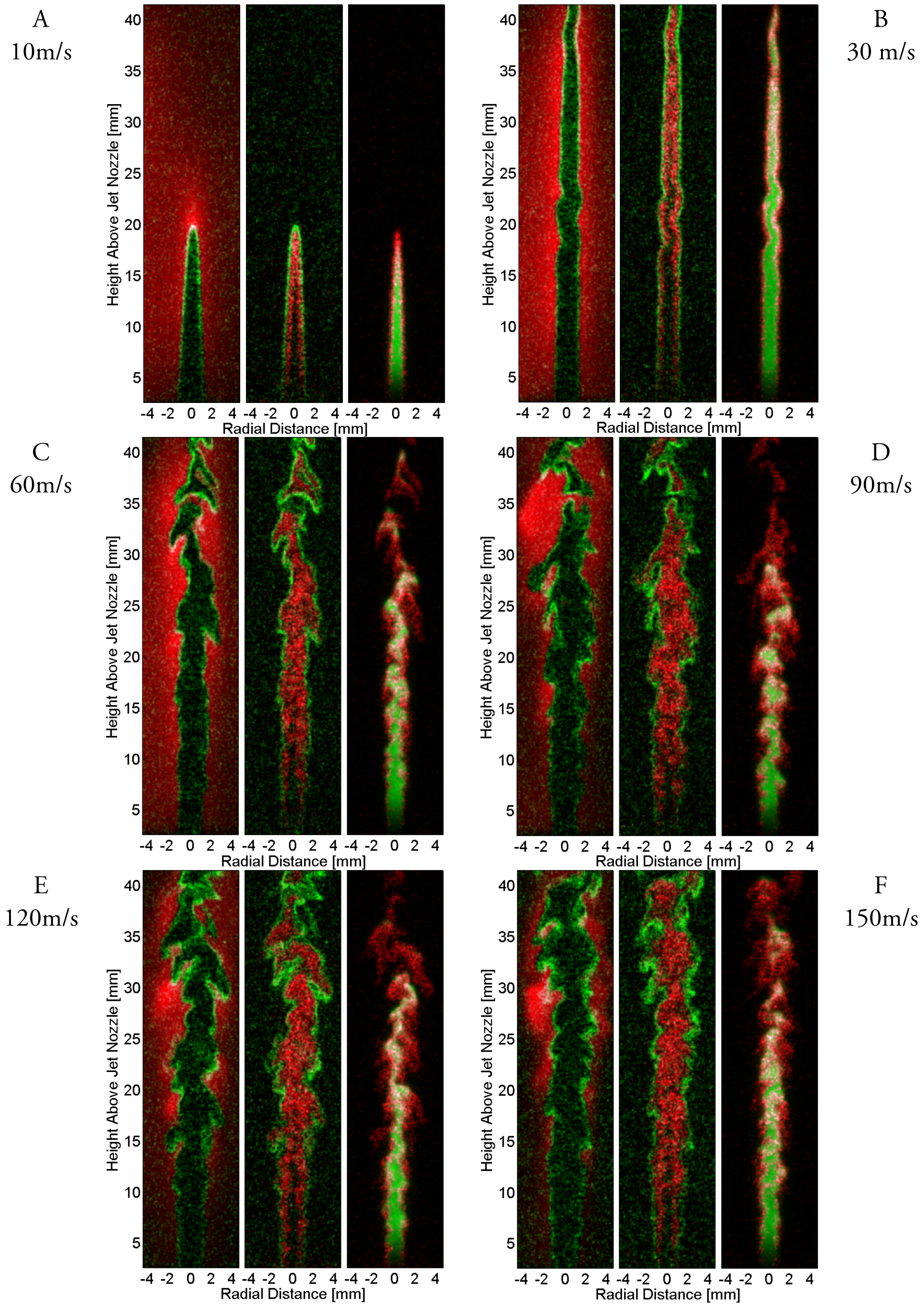

Figure 4.8 Six sets of single-shot images for jet flow speeds from 10 to 150 m/s. Each set contains three images. Left: OH (red) and CH (green), Middle: CH_2O (red) and CH (green), Right: CH_2O (red) and toluene (green), with the overlap between the two images in white.

In order to better visualize the spatial overlap between the four species, a smaller region from the initial images covering the laminar flame tip (indicated by the green boxes in Figure 4.6), is shown in Figure 4.7. Each of the three images in Figure 4.7 is composed of two LIF images. One is coloured black-to-red and one is coloured black-to-green. The spatial overlap between the images (multiplication of the two images) is coloured black-to-white. The left image shows OH (red) and CH (green), the middle image shows CH (green) and CH_2O (red) and the right image shows CH_2O (red) and toluene (green). The smooth gradients seen in Figure 4.7 are partially an averaging effect and partially due to the Gaussian filter that was applied to the images in order to suppress noise.

To see the dynamics of the turbulent jet flame, single-shot images are required. Figure 4.8 show six sets of single-shot images corresponding to jet flow speeds of 10, 30, 60, 90, 120 and 150 m/s. Each set of images was constructed in the same manner as in Figure 4.7. Figure 4.8 shows, as expected, that flame wrinkling and instability increase with increasing jet flow speed, leading to increased local overlap between OH and CH. The overlap between CH_2O and toluene is increased as a consequence of enhanced transfer of mass in the preheating zone by turbulent eddies [76]. In some cases the toluene signal can even be seen outside the CH_2O signal, indicating a very complex turbulent flame structure. Furthermore, the OH distribution becomes thinner and less intense with increasing jet flow speed. But as the CH signal does not weaken significantly, it can be assumed that the flames are not close to extinction.

The images were further binarized using a threshold slightly above the noise level. The integrated area containing a signal above the threshold is shown as a function of jet flow speed in Figure 4.9 A (The OH images are inverted to show the enclosed area). The areas all increase with increasing flow speed due to increasing flame length and flame front wrinkling. Figure 4.9 B shows the integrated area divided by its corresponding edge length. This represents the thickness of the different layers. The essentially flat CH curve indicates that the thickness of the main flame front remains almost constant under these flame conditions.

The overlapping area between different species is presented in Figure 4.9 C. This was calculated by binarizing the images (as in Figure 4.9 A) and then multiplying the images by each other. Note that this evaluation is very sensitive to the detection limit of each species, and can only be performed for simultaneous single-shot measurements. The OH x CH_2O overlapping area (corresponding to the oxidation layer of CH_2O) is small in all cases, and is a very weak function of jet flow speed, correlating well with the CH layer thickness shown in Figure 4.9 B.

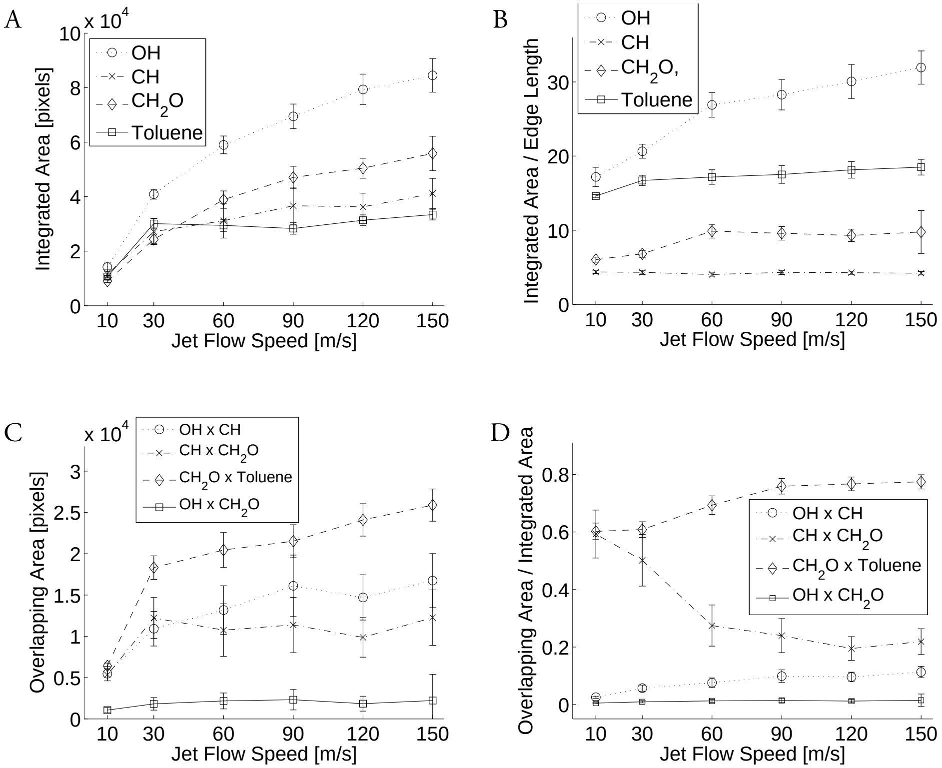

Figure 4.9 Integrated area of the binarized images (the OH images are inverted to show the enclosed area). B. Area divided by the corresponding edge length indicating roughly the width of the different regions. C. Overlapping area between two species (multiplication of binarized images). D. Overlapping area divided by the integrated area (C/A). All curves are shown as a function of jet flow speed (m/s) and the error bars indicate one standard deviation.

Figure 4.9 D shows the overlapping percentage (overlapping area divided by the larger of the two areas). The results for CH_2O x toluene is of particular interest as nearly 80% of the CH_2O zone is also populated with toluene at jet flow speeds above 90 m/s. Due to the rapid increase in the CH_2O area, the CH x CH_2O percentage decreases rapidly as the jet flow speed increases.

The broadened preheating zone (CH_2O) and thin CH layer at high jet speeds indicate that the flame is in the thin reaction zone regime. These results further indicate that the turbulence mainly affects the mixing in the preheating zone of the jet flame.

4.3 CO LIF

Two-photon CO LIF using 230 nm excitation ($B^1\Sigma^+ \leftarrow X^1\Sigma^+$) with detection of the Ångström band ($B^1\Sigma^+ \rightarrow A^1\Pi^u$) at 400 – 600 nm suffers from crosstalk from C_2 LIF. As the C_2 LIF signal overlaps the CO LIF signal temporally, spatially and spectrally in many cases, it can be difficult to remove it from the measurements. Furthermore, excited C_2 can be physically created by the laser pulse, due to the short wavelength used for CO LIF, making it even more difficult to avoid.

In the study presented in Paper XI different excitation-detection schemes (shown in Figure 3.3) were studied in an attempt to circumvent the C_2 interference. Two different excitation wavelengths were used, 230 and 217 nm, and the resulting spectra can be seen in Figure 4.10 (left and right columns respectively). Figure 4.10 A and B show CO LIF spectra from a laminar CO/air flame together with modelled CO and C_2 LIF spectra. This indicates which CO emission lines that might suffer from C_2 LIF interference.

The final four graphs in Figure 4.10 show CO LIF measurements in a laminar methane flame with the laser beam at two different heights above the burner for the two excitation wavelengths. The first position was above the primary flame front in the post-gases (Figure 4.10 C and D). At the other position the laser beam passed through the primary flame front (Figure 4.10 E and F) giving rise to high C_2 interference due to the natural occurrence of C_2 in the flame front and, partially, due to photodissociation of various species.

Some of the CO LIF peaks in Figure 4.10 are labelled with lower-case letters (a – n) and some of the C_2 LIF peaks are labelled with roman numerals (I – III). The peaks labelled a – e in Figure 4.10 C correspond to the third positive band and the peaks labelled f – i correspond to the Ångström band. In Figure 4.10 D, the peaks labelled j – n indicate the signal from the Herzberg band.

It is clear from Figure 4.10 that the detection scheme using the third positive band is better than the Ångström band regarding C_2 interference. However, broad-band emission from PAHs clearly disturbs the signal from the third positive band. The signal from the Herzberg band shows disturbances from both C_2 and PAH.

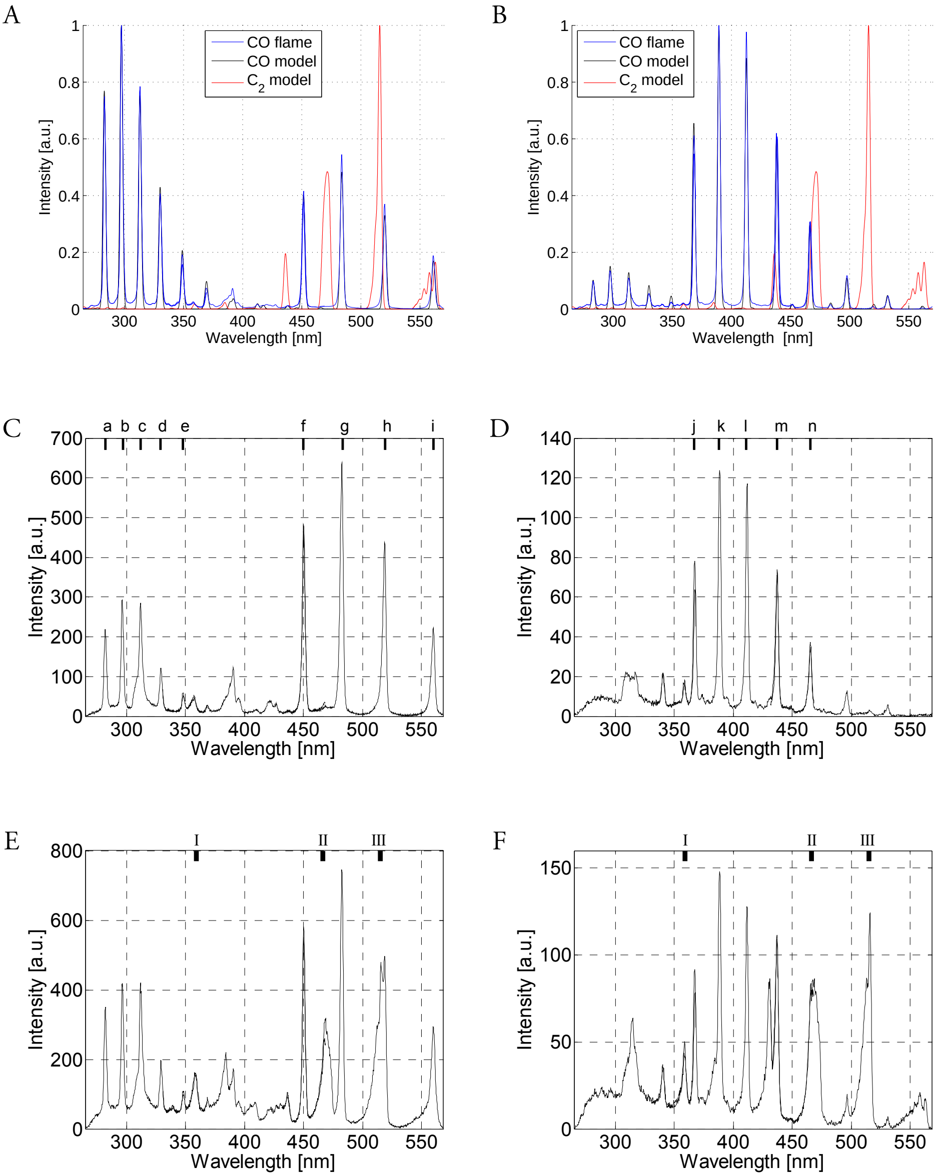

Figure 4.10 A and B: Modelled spectra of CO LIF and C_2 LIF together with measured spectra in a CO flame. C to F show CO LIF measurements in a laminar methane flame at two heights: C and D show measurements above the flame front and E and F show measurements through the primary flame front giving rise to high C_2 interference. The spectra in the left and right columns were recorded with 230 nm excitation (A, C and E) and 217 nm excitation (B, D and F), respectively.

An important issue for CO LIF measurements is the pressure dependence of the LIF signal. The pressure dependence of the CO LIF signal from the Ångström, third positive and Herzberg bands can be seen in Figure 4.11. The measurements were made in a pressure cell containing 0.1 bar CO and an increasing amount of air.

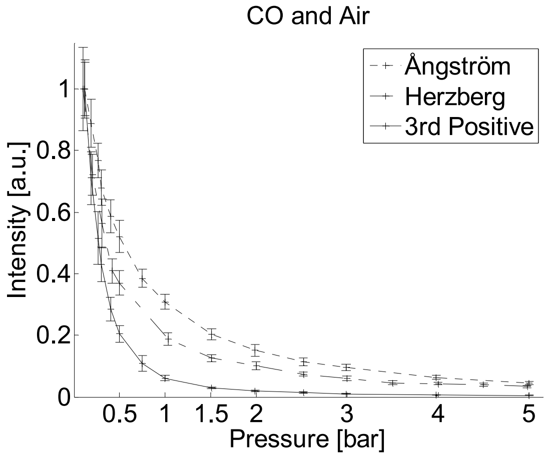

Figure 4.11 . CO LIF signal from the Ångström, third positive (both with 230 nm excitation) and Herzberg bands (217 nm excitation) as a function of total pressure (0.1 bar CO with increasing air partial pressure). The error bars indicate one standard deviation.

It can be seen that the third positive band has a slightly stronger pressure dependence than the other two bands. This would potentially make quantitative CO concentration measurements using the third positive band more difficult but not impossible. Measurements in IC engines at elevated pressures are probably not possible using the third positive band.

The best option (of the cases presented in Figure 4.10) for CO concentration measurements using LIF is to spectrally resolve the full emission spectrum resulting from 230 nm excitation covering both the Ångström and third positive bands. This gives the highest number of undisturbed CO LIF peaks and thus the best signal-to-noise ratio.

4.4 High-speed LII

High-speed LII measurements will suffer from problems due to sublimation, as discussed in Section 3.4.1. As a pre-study for high-speed LII measurements in an optical engine (presented in Section 5.5), the sublimation resulting from multiple pulses was studied in a comparatively slow laminar flame of a McKenna burner.

First, two pulses were sent through the flame with varying time separation and the LII signal from the second pulse was recorded. It can be can be seen in Figure 4.12 that the signal in this case decreased by between 20 and 30% for time separations shorter than 20 ms. This time separation corresponded fairly well to the dwell time of the soot particles in the laser sheet. An increase in LII signal for very short time separations was attributed to crosstalk with the LII signal from the first laser pulse.

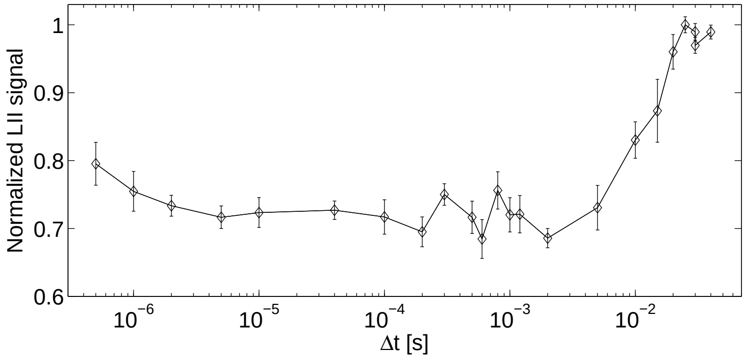

Figure 4.12 Normalized LII signal from the second of two pulses sent through a laminar flame as a function of the time separation, Δt, between the pulses.

As the aim was to achieve high-speed LII with several high-fluence laser pulses, eight pulses from the multi-YAG laser were sent through the same flame and the signal was detected using the SIM 8 framing camera. The resulting curve can be seen in Figure 4.13. The LII signal clearly decreases for the first to the fifth pulse, after which the curve levels out. It is clear that soot is destroyed by the laser pulses in these measurements. It is, however difficult to quantify the soot reduction as morphological effects will change the optical properties of the soot particles together with the reduction in particle mass [60].

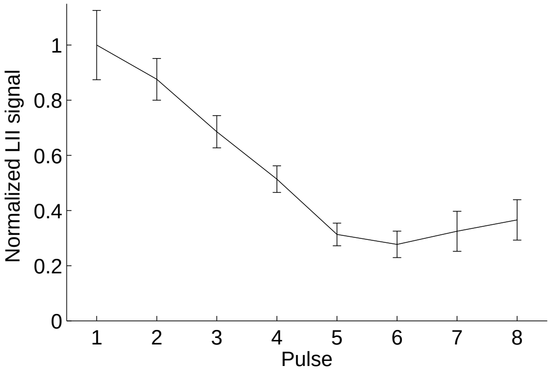

Figure 4.13 Normalized LII signal as a function of laser pulse number. The pulse-to-pulse time separation was 139 µs.

In engine measurements using the same high-speed LII setup, it was difficult to see a clear trend resulting from sublimation during the pulse train. The time-dependent soot formation and oxidation rates as well as the highly fluctuating turbulent mixing were strong enough to overpower sublimation, making direct measurement of its effect impossible. However, using two pulse trains positioned end to end in time could potentially reveal the effect of sublimation regardless of other effects. If the final image of the first pulse train shows a lower signal than the first pulse of the second pulse train, this would indicate a substantial sublimation effect, such as that shown in Figure 4.13.

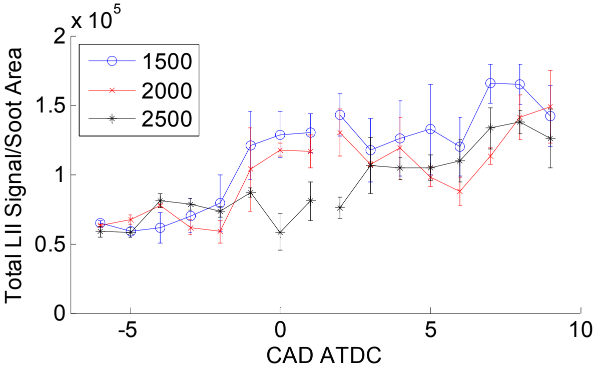

Figure 4.14 LII signal per unit area as a function of CAD ATDC (crank angle degrees after top dead centre) for one early and one late laser pulse train. The three curves represent different injection pressures, from 1500 to 2500 bar.

In Figure 4.14, however, no effect of sublimation was seen at any of the three injection pressures studied. One likely reason for this is the transport of fresh soot from the surrounding soot cloud into the laser sheet through turbulence. However, the absence of sublimation effects on the LII signal was fortunate since it made the high-speed LII measurements easier. Assuming no sublimation effect allowed the images to be analysed as if they were independent of previous images.

4.5 SLIPI –Engine application

The SLIPI measurements presented in Paper VIII represent the first time SLIPI was applied to gas phase LIF and to in-cylinder measurements in an IC engine. These measurements required some development of the SLIPI technique (see Section 3.5 and Equation (3.21)). The measurements were made in an optical Scania D12 heavy duty diesel engine (see Section 2.3.2). The laser sheet alignment relative to the top of the quartz piston can be seen to the left in Figure 4.15, and two raw data images with modulation can be seen on the right, one with DI (top) and one with homogeneous Φ distribution (bottom) through port fuel injection (PFI).

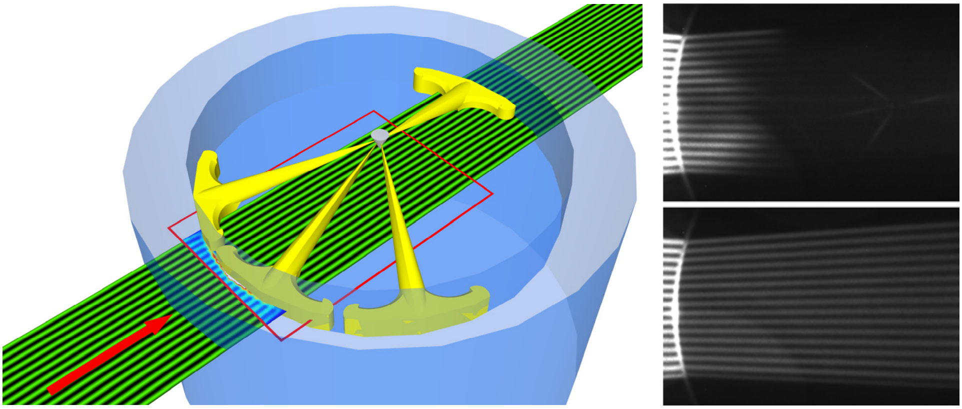

Figure 4.15 Left: Illustration of the piston top (blue), modulated laser sheet (green), DI fuel jets (yellow) and the imaged area (red square). Right: Raw data images with modulated laser sheet using DI (top) and PFI (bottom). The quartz fluorescence can be seen in the left part of the images.

Both SLIPI and regular LIF images were calibrated to show the equivalence ratio, Φ, using PFI to give a homogeneous fuel distribution in the cylinder at top dead centre. The two Φ calibration curves can be seen in Figure 4.16. The difference in slope between the two curves is partially due to higher laser fluence in the LIF images, but is mainly caused by the SLIPI calculations which reject the major part of the signal.

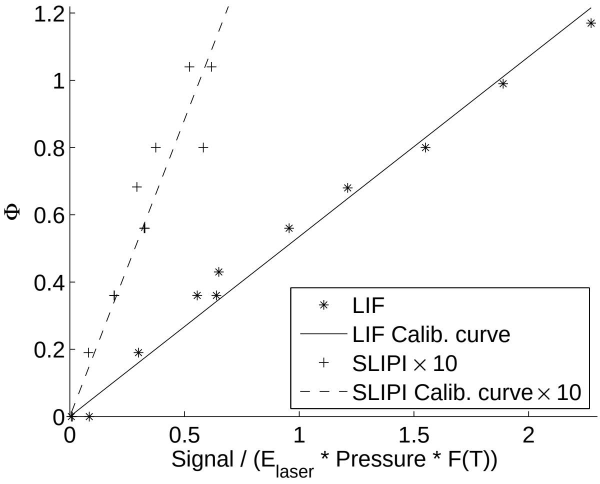

Figure 4.16 Calibration curves for regular LIF and SLIPI showing Φ as a function of signal level divided by the laser energy, in-cylinder pressure and the temperature function (in accordance with Equation (3.15)). The SLIPI signal (x-axis) has been multiplied by a factor of ten for clarity.

Figure 4.17 shows a comparison between the SLIPI (left column) and regular LIF (right column) measurements. The colour scales are the same in all the images and represent Φ values as indicated by the colour bar at the bottom. The first row shows the early fuel jet before wall impingement at -4 CAD ATDC. The next three rows show the evolution of the jet and the recirculation zone between the two fuel jets up to the end of injection (EOI) at 7.7 ±0.1 CAD ATDC. At 14 CAD ATDC fuel is still present mainly in the recirculation zone. The bottom row shows the jet after end of injection.

The comparison in Figure 4.17 between SLIPI and regular PLIF shows that SLIPI gives lower Φ values in the free jet but not in the recirculation zone. To further illustrate this, a path was selected following the average path of the fuel jet (see Figure 4.18 A). The comparison along this path can be seen in Figure 4.18 B and D for 6 CAD ATDC (before EOI) and 14 CAD ATDC (well after EOI).

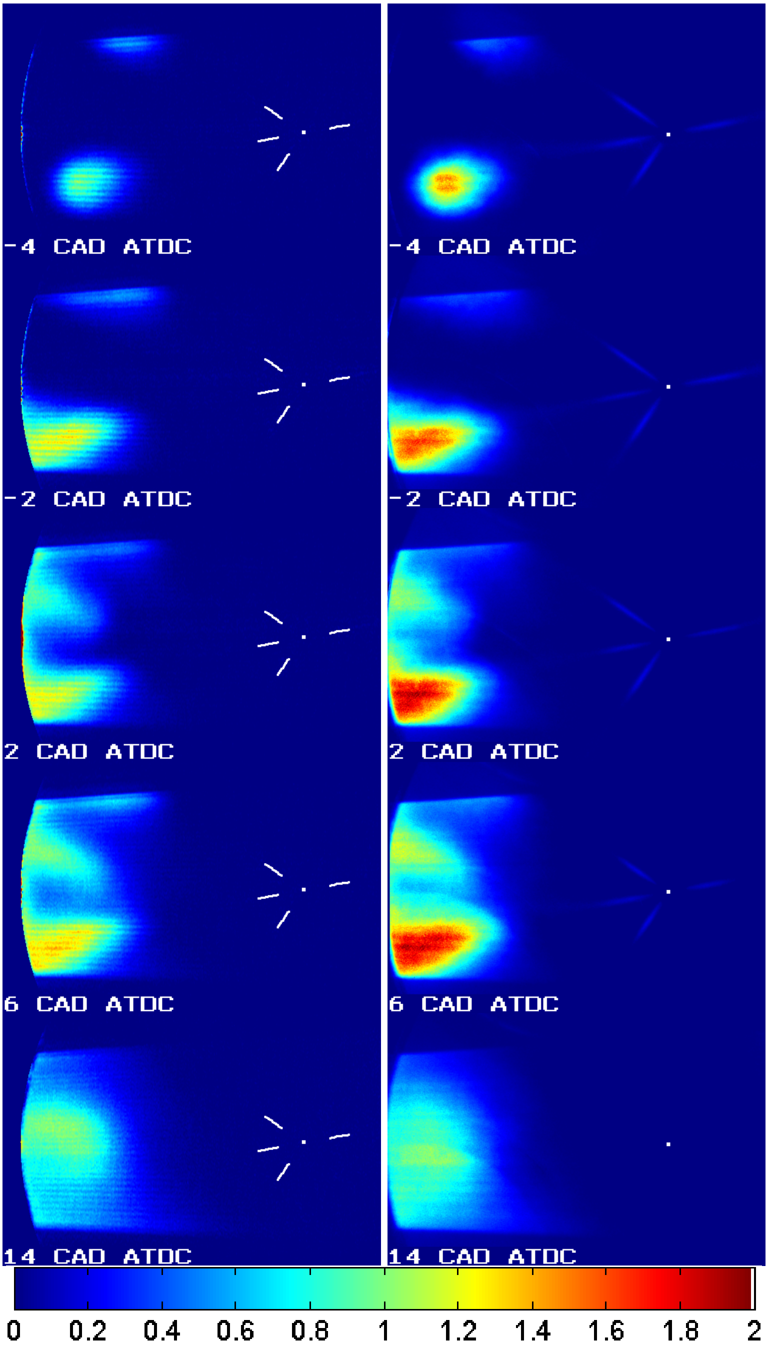

Figure 4.17 Comparison between SLIPI (left) and regular LIF (right) for timings between -4 and 14 CAD ATDC. The colour scale represents Φ values as indicated by the colour bar.

The average values of Φ for SLIPI and regular LIF in the free jet and the recirculation zone were calculated by averaging the signal in two small regions indicated by black squares in Figure 4.18 A. The resulting average Φ values are shown as a function of CAD ATDC in Figure 4.18 C. Figure 4.18 clearly demonstrates that SLIPI gives lower Φ values in the free jet but not in the recirculation zone compared with regular LIF. The reason for this is not clear. One possibility is that the impact of the jet destabilizes the thermal boundary layer close to the bowl wall. This would lower the SLIPI signal as the modulation of the laser sheet is lost as it enters the combustion chamber. However, the images at -4 CAD ATDC, where the jet has not impacted the bowl wall, contradict this theory. Another explanation may be that multiple scattering is stronger in the free jet region, leading to an increased signal in the regular LIF images that is suppressed using SLIPI. This might be due to a larger volume of fuel tracer surrounding the laser sheet in the free jet, thus giving rise to higher levels of secondary fluorescence.

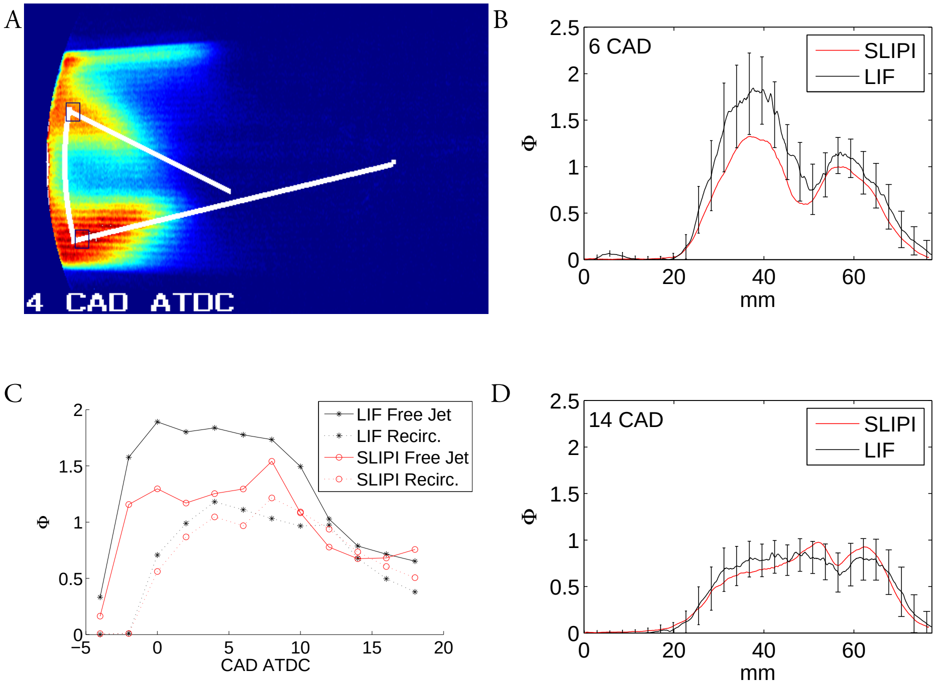

Figure 4.18 A: Image showing the selected regions in the free jet and the recirculation zone (black squares) and the path used in the evaluation (white). C: Average Φ values for SLIPI and regular LIF in the free jet and the recirculation zone as a function of CAD ATDC. B and D: Φ values for SLIPI (red) and regular LIF (black with error bars showing one standard deviation) along the path for 6 CAD ATDC (B) and 14 CAD ATDC (D).

Chapter 5 Results – Engine Measurements

5.1 Introduction

The different measurement campaigns presented in this chapter were conducted in collaboration between the Division of Combustion Physics and the Division of Combustion Engines at Lund University. The measurement campaigns are presented in chronological order. The first papers cover HCCI combustion, where the effects of turbulence and temperature stratification were investigated using high-speed fuel tracer LIF. As the research continued, new low-temperature combustion concepts, with better combustion control and unburned hydrocarbon emissions compared to HCCI, were developed and analysed. As part of this development, spark assisted compression ignition (SACI) was studied using high-speed fuel tracer LIF in an attempt to discern fuel stratification and its effect on SACI combustion.

The activities of the Multi-YAG group then shifted to diesel engine research in collaboration with the Gendies Lab. The main goal was to understand the connections between spray processes and the formation of pollutants such as soot particles and unburned hydrocarbons in diesel engines using optical diagnostics. Raman spectroscopy was first used to measure the fuel-air ratio in an in-cylinder fuel jet. This revealed surprisingly low correlations with engine-out soot and thus further studies were planned. The first was high-speed LII measurements in which the actual soot distribution was measured, cycle resolved, in an attempt to understand the soot formation and oxidation processes. The LII measurements could, however, not reveal the connection between the soot distribution and the underlying mixing processes in the fuel jet. Thus, fuel tracer LIF using SLIPI was applied for measurements of the equivalence ratios in the fuel jets to further increase the understanding of the fuel distribution and its evolution in the combustion chamber.

5.2 HCCI – Turbulence and temperature stratification

Two different HCCI engine configurations were studied; the difference between them being mainly in the piston geometry. One had a flat piston top creating a thin disk-shaped combustion chamber, while the other had a large square bowl in the top of the piston. Both pistons allowed for optical access to the combustion chamber, and in the case of the square bowl piston also into the piston bowl as the entire piston top in this case was made of quartz.

The aim was to study the effect of turbulence on HCCI combustion. The turbulence level was expected to be higher in the square bowl case as the squish flow into the bowl close to TDC should generate a high degree of turbulence at the time of combustion [78, 79]. This squish flow would naturally not be present with the disk piston geometry, resulting in a lower degree of turbulence at TCD.

Figure 5.1 shows the rate of heat release for the two cases. It is clear from these curves that the disk piston gives very rapid combustion, even at the high lambda value used here. The square bowl piston geometry, on the other hand, gives a lower peak value and a longer combustion duration, indicating a strong effect of the piston geometry.

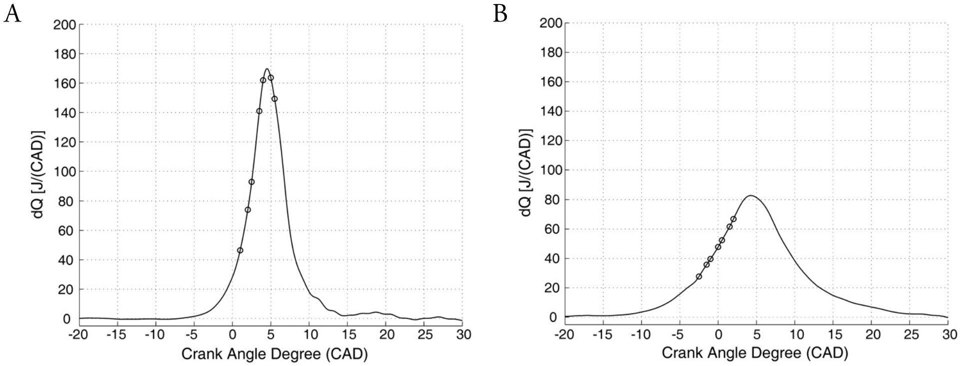

Figure 5.1 Rate of heat release with the disc piston geometry (A) and the square bowl piston geometry (B) for $\lambda = 3.7$ in both cases. The circles indicate the timing of the PLIF images in Figure 5.2.

To understand the effect of the piston geometry on the combustion, high-speed fuel tracer LIF was used. The fuel was ethanol with acetone as fuel tracer, excited using 266 nm laser pulses from the multi-YAG laser and using the Imacon 468 framing camera as detector. The laser sheet was slightly convergent in the square bowl geometry due to the strong lens effect of the piston.

Figure 5.2 shows two series of high-speed fuel tracer LFI images. The top two rows (smaller images) were recorded using the disk piston geometry. The bottom two rows (larger images) were recorded in the square bowl piston with the laser sheet positioned roughly halfway between the top of the piston and the floor of the bowl. Bright areas in the images indicate areas where fuel is present, and darker areas indicate areas where the fuel has burnt or at least started to react. Both series include schematics (lower right) of the combustion chamber geometries, in which the dashed lines indicate the laser sheet positions. The timing of each image is shown in the lower right corner of each image as a function of CAD ATDC. The timing of the images is also indicated in Figure 5.1 as circles along the curves.

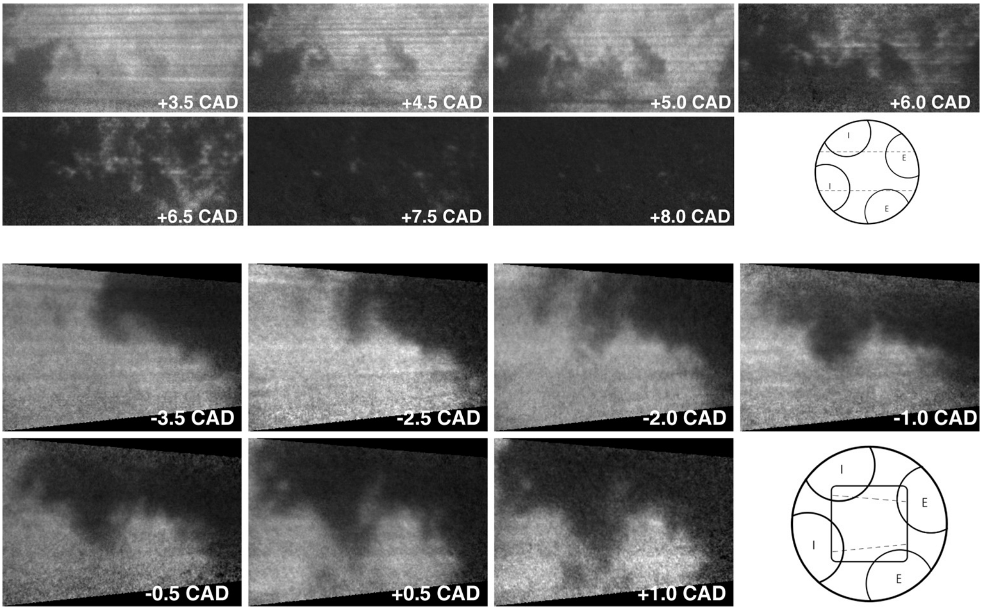

Figure 5.2 Image sequences of single-shot fuel tracer PLIF images for λ = 3.3. The images in the upper sequence were obtained with the disc piston, and the lower sequence with the square bowl piston.

There are clear differences in the combustion behaviour between the two geometries. In the disk geometry, fuel consumption starts at multiple ignition points and the decrease in fuel concentration is gradual, without sharp concentration gradients, clearly showing a lack of flame-front-like propagation. In the square bowl geometry, ignition occurs only at a few positions and the combustion seems to be more flame-front-like, with sharper concentration gradients.

In order to clarify the underlying phenomena resulting in the trends seen in Figure 5.2, LES were made. LES were used as they can provide detailed information on the turbulence and temperature field prior to auto-ignition as well as details regarding the combustion process. The simulations showed that although the instantaneous flow structures in the disc geometry and the square bowl geometry were significantly different, the degree of turbulence (root-mean-square of the resolved velocity field) was fairly similar in the two geometries, as shown in Figure 5.3 A. This indicated that an increase in the amount of turbulence was probably not the main factor responsible for the increase in combustion duration seen with the square bowl geometry (see Figure 5.1).

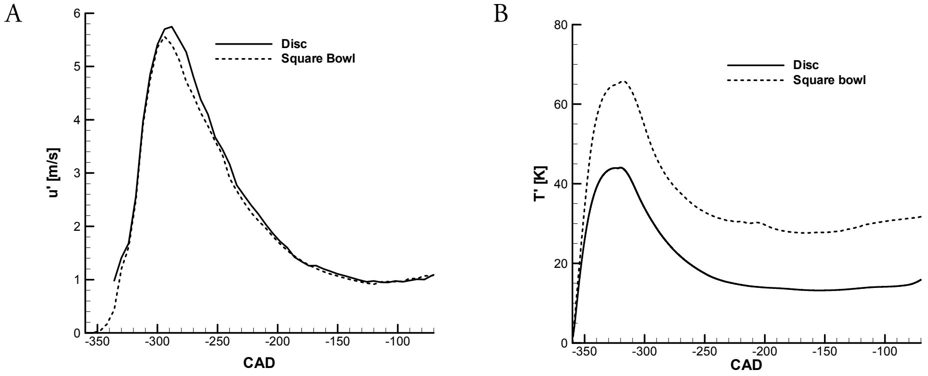

Figure 5.3 Results of LES showing the turbulence (A) and the temperature inhomogeneity (B) as a function of CAD ATDC for the two piston geometries.

Furthermore, LES showed that the temperature inhomogeneities for the two engine geometries were significantly different, as can be seen in Figure 5.3 B. The temperature inhomogeneity in the square bowl geometry was almost twice that in the disc geometry. It was concluded that the difference in temperature inhomogeneity between the two cases was primarily caused by heat transfer from the different piston geometries.

The temperature distributions obtained with LES after the onset of auto-ignition are shown in Figure 5.4 for the same cases as in Figure 5.2. The images in Figure 5.4 for the square bowl geometry (bottom) are composed of two separate geometrical planes, one through the square bowl and the other intersecting the squish region.

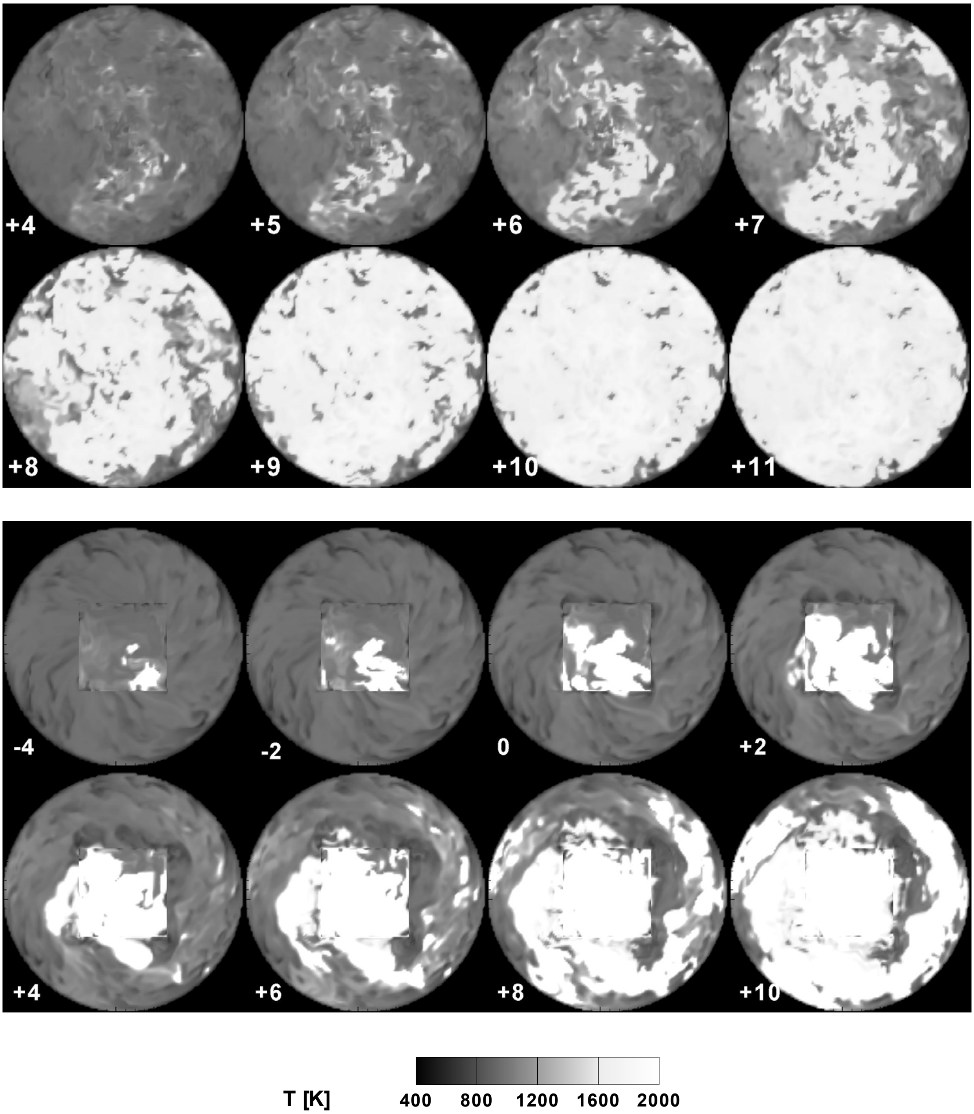

Figure 5.4 Instantaneous temperature fields obtained from LES for the disc geometry (top) and the square bowl geometry (bottom) for λ = 3.3, matching the case shown in Figure 5.2. The timing (CAD ATDC) of each picture is given in the lower left corner.

For the disk geometry (top part of Figure 5.4), the LES results indicated that there were a few locations with locally higher temperature where the mixture tended to ignite first. Increasing heat release then quickly promoted auto-ignition in the entire cylinder.

In the square bowl geometry, the higher temperature that developed in the bowl prior to ignition promoted auto-ignition in the bowl. Similarly to the PLIF images shown in Figure 5.2, combustion started in one corner of the square bowl and then moved across the bowl in a flame-front-like manner following the temperature stratification. At 4 CAD ATDC, the results indicated that the combustion had spread to the squish region.

The drawn conclusion from these results was thus that the square bowl mainly acted as a heater that increased the temperature of the mixture in the bowl significantly during the compression stroke. The effect was mainly due to the large surface area of the bowl walls, but also due to the lower average flow speeds in the bowl during the intake and compression stroke. This, and not increased turbulence, was clearly the reason for the increased combustion duration in the square bowl geometry.

5.3 SACI –Fuel stratification

Spark assisted compression ignition was studied using high-speed fuel LIF in order to investigate the effect of fuel stratification on the SACI combustion process. SACI is a combination, or middle ground, between regular spark ignition (SI) and HCCI and was developed mainly in an attempt to extend the load range of HCCI [80].

The engine rig can be seen in Figure 2.14. The engine was based on a Volvo D5, which was modified for optical measurements with a Bowditch piston extension and a disk-shaped combustion chamber geometry. The engine was also equipped with a pneumatic, fully variable valve train. Direct injection in combination with port fuel injection allowed different fuel stratification levels to be studied.

The fuel used in this study was ethanol with 10% acetone (by volume) added as a tracer. The multi-YAG laser was used for excitation, producing slightly above 10 mJ of 266 nm radiation per pulse with a pulse separation of 1 CAD, i.e. 139 µs. The horizontal laser sheet illuminated almost the entire visible region of the combustion chamber, which in turn was limited by the flat quartz piece in the top of the piston. The camera's field of view can be seen in Figure 5.5. The five-hole direct injector was mounted centrally in the cylinder and the sparkplug was mounted between the intake valves, above the direct injector in the images. A LIF image showing the homogeneous fuel distribution resulting from PFI and the five fuel jets from DI can also be seen in Figure 5.5. The fuel jets are not visible close to the injector due to the downward angle of the jets and the positioning of the laser sheet.

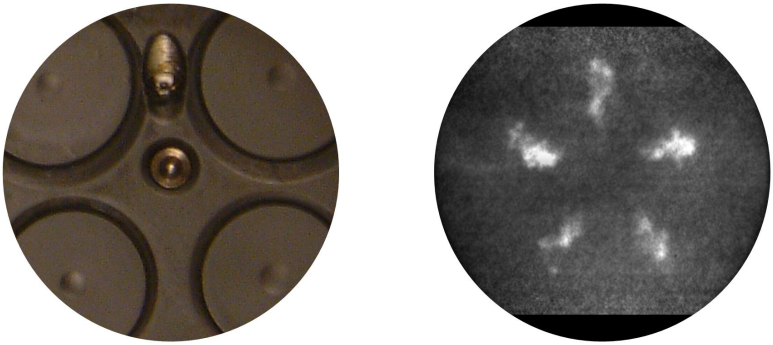

Figure 5.5 Field of view from below through the piston extension (left) and a fuel LIF image showing both the PFI distribution (homogeneous field) and the five DI fuel jets.

Several engine parameters were studied in attempts to reveal temperature and fuel stratification effects on SACI combustion. In this section the DI fraction sweep will be presented. Additional information can be found in Paper III.

The different combustion time scales can be seen in Figure 5.6 for varying DI percentage (the total amount of fuel, DI+PFI, was kept constant). Upon increasing the DI percentage the combustion phasing (CA50) was fairly constant but the combustion duration, defined as the time between CA10 and CA90, increased. The increased combustion duration resulting from increasing stratification (i.e. DI percentage) was counteracted by the PFI point (0% DI). However, this point was run at a slightly lower load, and this in itself gave a longer burn duration.

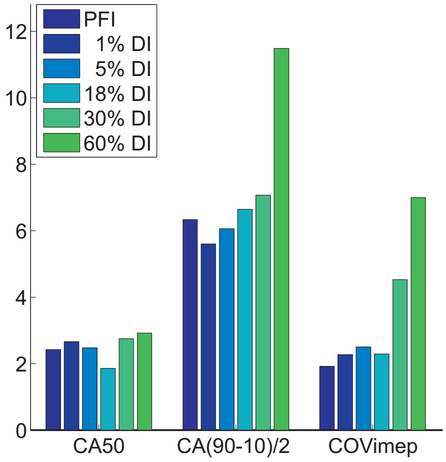

Figure 5.6 Combustion timing, CA50 [CAD ATDC], combustion duration defined as CA(90–10)/2 [CAD] and the combustion instability COVimep [%] for increasing percentages of DI, from 0 (PFI only) to 60%.

At the highest percentage of DI the combustion instability (coefficient of variation for the indicated mean effective pressure COVimep) also increased significantly due to partial burns in some cycles, which also explain the much longer combustion duration in this case. The poor combustion stability was mostly caused by the disk-shaped combustion chamber which allowed the fuel spray to reach the outer walls of the combustion chamber, leading to overlean conditions at the spark plug position and thus poor combustion stability. The partially burned fuel at the higher DI percentages was further reacted during the negative valve overlap (NVO). This was seen in the pressure traces as a positive heat release during the NVO and was expected to increase the temperature of the retained charge in the following compression stroke.

Series of high-speed fuel LIF images can be seen in Figure 5.7. The columns represent, from the left 1, 18, 30 and 60% DI. DI timing, i.e. when injection was started, was –70 CAD ATDC. Note that the total amount of fuel (DI+PFI) was constant during the measurements.

The images show that for these combined PFI/DI strategies a very high level of fuel stratification can be created without shifting the combustion phasing (see also Figure 5.6). The images further show an increase in the number of fuel ignition sites with increasing DI percentage. However, it is not the fuel-rich zones that appear to ignite first. The high heat of vaporization probably lowers the local temperature in these zones to an extent that it inhibits early ignition [81]. Ignition instead occurs in the mixing region between the rich and the lean zones. This probably corresponds to the optimum regions in terms of fuel concentration and temperature. The overlean regions probably have a higher temperature and possibly also higher levels of residual radicals from previous cycles as a rather large NVO was used in this study.

Although these regions become more abundant with increasing stratification, the combustion processes must still proceed to the leaner and richer regions. As this clearly takes more time than the fast HCCI-like combustion seen for the more homogeneous cases, this explains the increased combustion duration for increased amounts of DI.

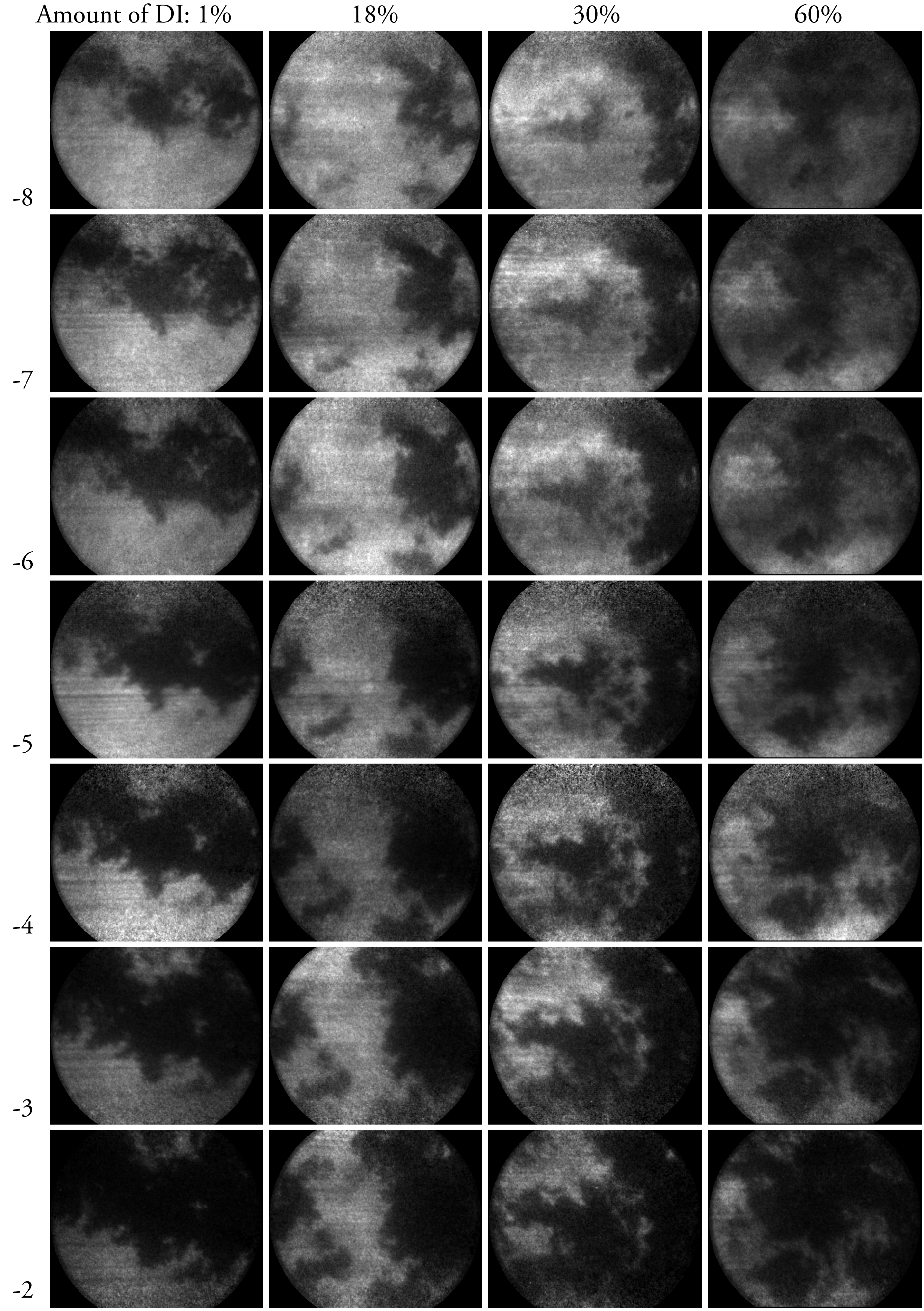

Figure 5.7 Series of high-speed PLIF images with varying amounts of DI as indicated at the top of each column. The timing (CAD ATDC) is shown at the left of each row. Each column represents a single cycle and has a normalized greyscale. The DI timing was –70 CAD ATDC.

5.4 Local Φ in a CI engine using Raman spectroscopy

Measurements of the fuel-air ratio inside a fuel jet and correlations with the engine-out emissions are presented in Paper V. Raman spectroscopy was used for the measurements since it can measure the concentration of all major species simultaneously (see Section 3.2). As the problem at hand was inherently very complex, some limitations were imposed on the setup. The original diesel fuel was replaced by a single-component fuel to avoid problems associated with fluorescence and other interfering signals that might have overwhelmed the week Raman signal.

The setup was first tested using reacting fuel jets, but this led to too much beam steering and LIF backgrounds that effectively prevented the measurements. Thus, a non-reacting fuel, pure isooctane was selected (isooctane did not ignite under the low oxygen conditions used). The removal of the flame surrounding the fuel jet led to significant changes. It was, for instance, expected to significantly increase the amount of oxygen being mixed into the centre of the fuel jet from the surrounding gas, at least downstream of the previous lift-off length. As the measurements presented in Paper V were made only a few millimetres after the lift-off length in most cases, it was expected that the change to non-reacting conditions would only introduce a minor deviation, and that the trends in the data would still be valid. The emission level measurements were made with 70% n-heptane and 30% isooctane producing reacting conditions.

Design of Experiments (DoE) was used to create a measurement plan based on a central composite design with three parameters: injection pressure, oxygen fraction and TCD density (boost level). A graphical representation of the DoE setup and the parameter values used can be seen in Figure 5.8. Using DoE it was possible to reduce the number of measurement points from 27 (3^3) to 15, with a corresponding reduction in measurement time, without losing significant information.

The laser beam was aligned perpendicular to one of the fuel jets from a symmetrical three-hole injector. The laser beam intersected the fuel jet 23.5 mm downstream of the injector nozzle. A wavelength of 266 nm was used to exploit the benefit of the increased Raman cross section at shorter wavelengths, and the multi-YAG laser was used to obtain a higher total laser energy (1 W in total) in the measurement region, without damaging the optical components or causing optical breakdown in the measurement region. The entire pulse train of eight pulses was 52,5 μs long.

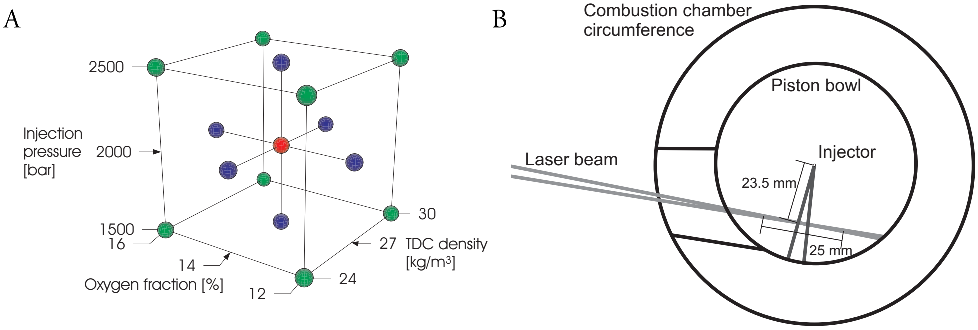

Figure 5.8 A Graphical depiction of the experimental factors and their values, Green represents corner points, red represents the centre point and blue represents axial points in the central composite design. B Sketch of the combustion chamber, laser beam, and one fuel jet. The measurement zone was 25 mm long and was positioned 23.5 mm from the injector.

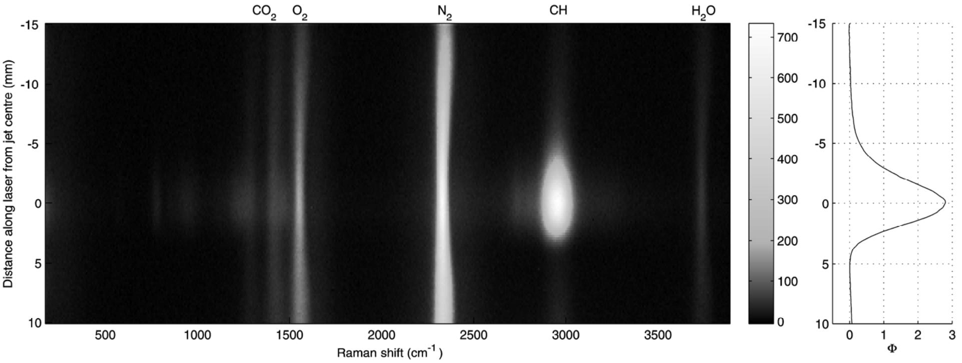

Figure 5.9 A Raman spectrum recorded in the engine. The y-axis shows distance along the laser beam in mm from the centre of the fuel jet, and the x-axis indicates the Raman shift in cm^{-1}. The graph to the right shows the corresponding Φ values.

Figure 5.9 shows a resulting average image of the Raman spectrum along the laser beam. The different species that could be detected are shown at the top of the image, and 0 mm on the vertical axis represents the centre of the jet, as indicated by the CH stretch at 2903 cm^{-1}. The graph on the right shows the corresponding Φ values across the jet. These values were calculated directly from the Raman images (with a calibration measurement using PFI) using the O_2 and CH emission lines at 1556 cm^{-1} and 2930 cm^{-1}, respectively. Thus, for the single shot images, this method automatically corrected for variations in laser power, etc. The Φ curve across the jet was found to follow a slightly skewed Gaussian profile for all measurement points due to the swirling flow in the combustion chamber.

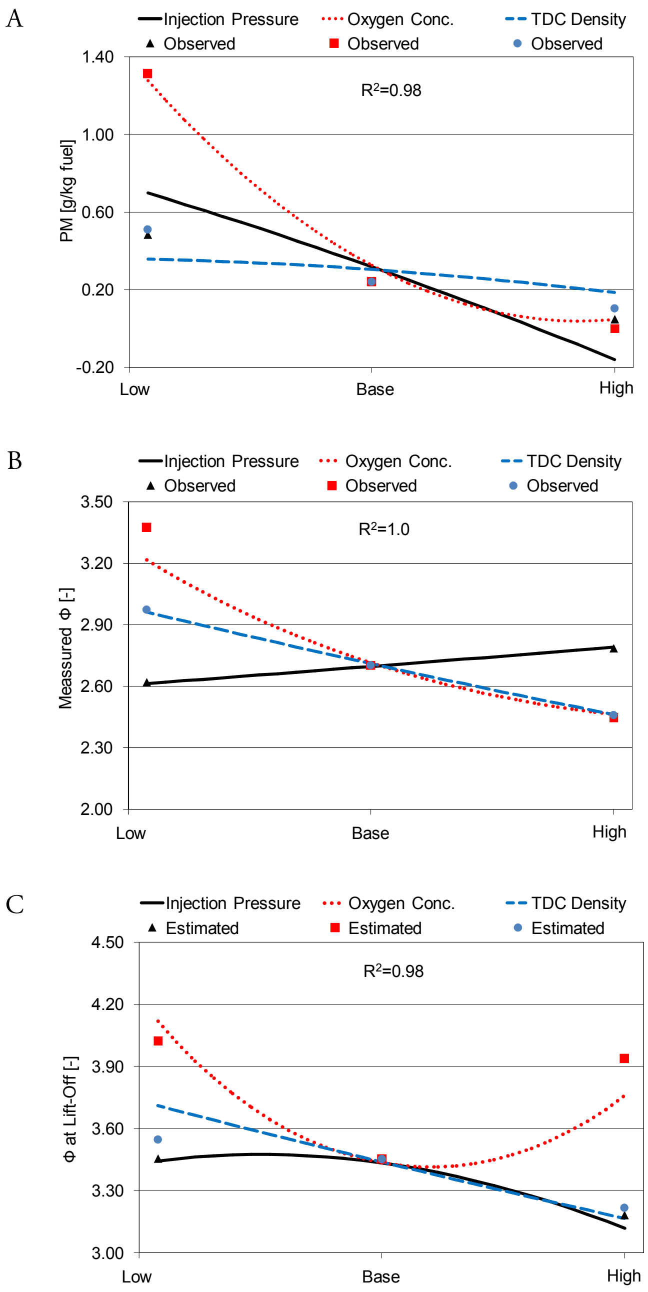

Figure 5.10 Particulate matter (PM) emissions (A), Φ values in the centre of the jet at 23.5 mm (B) and Φ values scaled to the lift-off region (C) as a function of: injection pressure, oxygen concentration and density at TDC. The symbols show the measured values and the curves were obtained from the regression model.

The errors in the Raman measurements were evaluated using the ratio between the N_2 and O_2 signals as this is independent of the fuel mixing processes. The analysis showed that the systematic measurement error was around 4%. The standard deviation of the measured Φ values was roughly 10%; the increase in variation being attributed to variations in the fuel-air mixing process

Figure 5.10 shows a compilation of the results from the measurements. The symbols in these graphs correspond to the measurement values from the axial points in the DoE setup (see Figure 5.8 A). The curves represent the DoE regression model that was fitted to the entire data set, containing all 15 measurement points.

Figure 5.10 A shows the particulate matter (PM) emissions from the engine, using the reactive fuel mixture. It can be seen that the PM leaving the engine decreased with increasing inlet oxygen concentration, increased density at TDC, and increased injection pressure; inlet oxygen concentration having the strongest impact.

Figure 5.10 B shows the measured Φ values, determined from the Raman spectroscopy data in the centre of the jet, 23.5 mm from the injector. Increased oxygen concentration, naturally, led to a decrease in the local Φ value. The decreasing trend in Φ for increasing TDC density indicated a higher entrainment rate into the jet at higher density. The data also showed a weakly increasing trend in Φ with increasing injection pressure. This suggests that the increasing velocity dominates over the increasing mixing rate, resulting in higher Φ values at the measurement location, at higher injection pressures. Figure 5.10 C finally shows the Φ values at the lift-off length. These were obtained by scaling the Φ values at the measurement point using a relation given by Siebers [82]. The lift-off length was measured using OH chemiluminescence.

Some similarities can be seen between the PM emissions and the Φ values at the lift-off length in Figure 5.10 A and C, but the differences are more interesting. At high oxygen concentrations, the Φ values at the lift-off length are high due to the shortened lift-off length. High Φ values in combination with high oxygen concentrations should lead to a high soot formation rate. However, the PM emissions are zero at this point. This strongly indicates that the soot formation rate is not the dominating factor behind the PM emissions leaving the engine.

A correlation analysis further confirmed this hypothesis. In Figure 5.11 the correlation coefficients between engine-out PM and various parameters can be seen. For this data set the correlation coefficient should be higher than 0.45 to be statistically significant. The only factors in Figure 5.11 that show a significant correlation to the PM emissions are the engine-out UHC (unburned hydrocarbons), the engine-out CO and the heat released after end of injection. These parameters are all associated with the soot oxidation process. The Φ values at the lift-off position, which are associated with the early soot formation process, show a very low correlation coefficient with engine-out PM. This suggests that the soot oxidation process is more important than the soot formation process for engine-out PM.

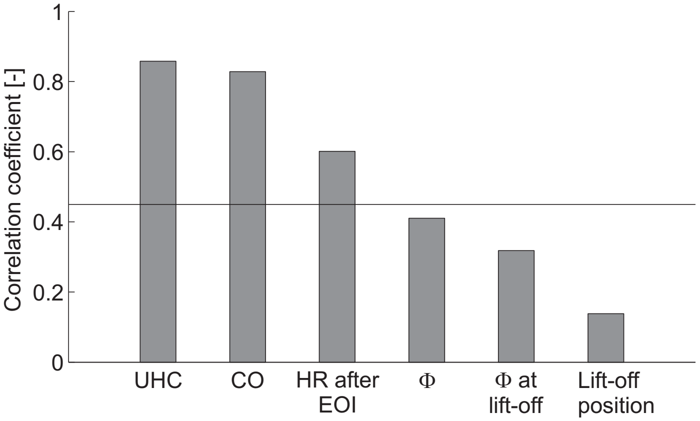

Figure 5.11 Correlation coefficients between engine-out PM and from the left: UHC, carbon monoxide, heat released (HR) after end of injection (EOI), measured Φ at 23.5 mm, Φ at the lift-off position and, finally, the lift-off position. Correlation coefficients should be above 0.45 to be statistically significant.

5.5 High-speed LII – EGR effects

Following the previous Raman spectroscopy measurements, which showed a low correlation between Φ values and engine out soot from the heavy duty diesel engine, measurements of the actual soot distribution were deemed necessary. High-speed LII was chosen since it was also deemed necessary to follow the soot evolution within a single cycle in the diesel engine. Questions regarding the LII technique and its applicability for high-speed in-cylinder measurements have been addressed in Section 3.4.1 and 4.4. In this section the results from the engine tests with varying percentages of oxygen will be presented.

The oxygen percentage was regulated using an external EGR source consisting of a diesel furnace. The inlet was also pressure and temperature regulated using a two-stage compressor and an external heating system. The start and end of injection (SOI and EOI) were varied in order to maintain the combustion phasing (CA50) over the oxygen percentage sweep. The SOI was between –15 and –9 CAD ATDC and the EOI was between 12 and 18 CAD ATDC.

The engine-out smoke as a function of oxygen percentage in the inlet is shown in Figure 5.12 A. As the O_2 percentage was lowered from 21% the engine-out smoke increased from an FSN (filtered smoke number) of zero up to a peak of FSN = 2 at 11% O_2. Below 11% O_2 the FSN values rapidly decreased down to almost zero again at 9% O_2.

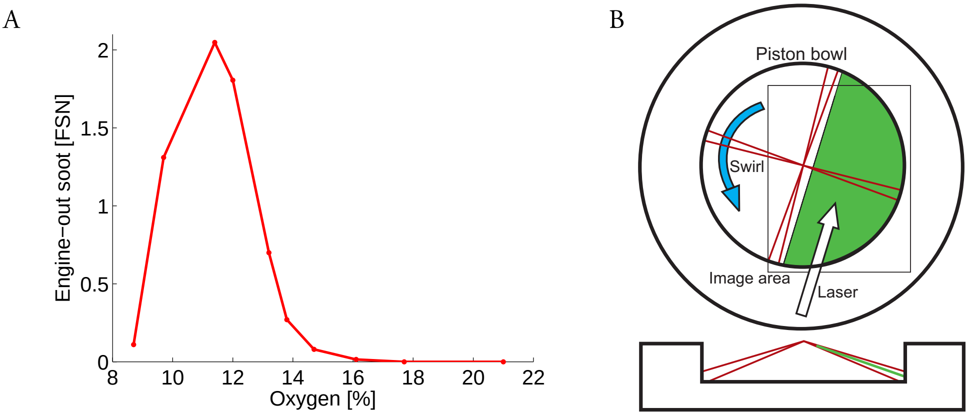

Figure 5.12 A Engine out emissions of soot (FSN) as a function of percentage O_2 in the inlet. B Alignment of the The laser sheet (green) relative to the piston bowl and the fuel jets (red). The imaged area is indicated by the black rectangle.

A sketch of the laser sheet alignment can be seen in Figure 5.12 B. The laser sheet was tilted to follow one of the fuel jets from the injector to the bowl wall. The laser sheet also intersected the recirculation zones on either side of the main fuel jet where the wall jets from neighbouring fuel jets collide. As high-speed LII measurements were called for, the multi-YAG laser was used, producing pulse trains of eight pulses with pulse separations of 1 CAD or 139 µs. The laser sheet was about 1 mm thick and had a top hat energy profile.

Two series of high-speed LII images are shown in Figure 5.13 for 14% O_2 in the inlet. The images were recorded between –6 and 9 CAD ATDC or between 8 and 23 CAD ASOI (after start of injection). The data have not been recalculated to give quantitative values (soot volume fraction) and thus the grey scale at the bottom represents the signal intensity.

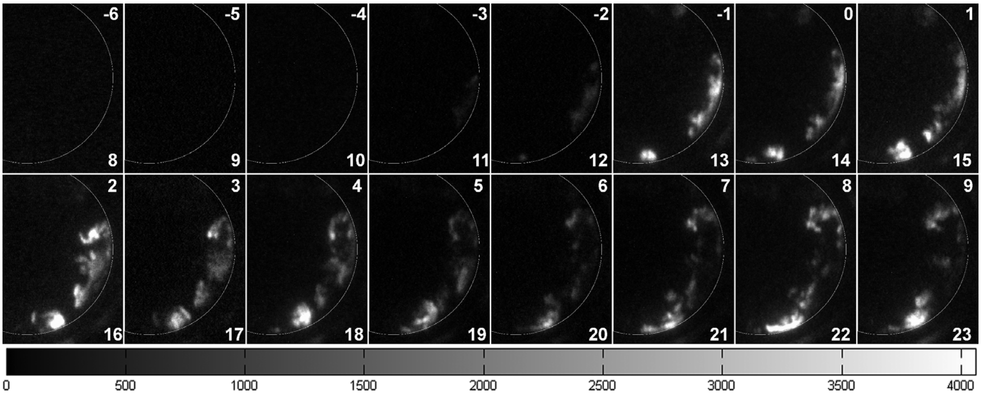

Figure 5.13 Two series of LII images taken with 14% O_2 and 2000 bar injection pressure. The numbers in the upper right corners indicate CAD ATDC and the numbers in the lower right corners indicate CAD ASOI. The grey scale represents the signal intensity.

As the fuel jet from the injector collides with the wall, the first evidence of soot can just be discerned in the image, at 11 CAD ASOI. The first appearance of soot was seen slightly after the start of the mixing-controlled combustion at all O_2 fractions, i.e. after the end of the premixed combustion phase. As n-heptane was used, the soot production was probably delayed compared to traditional diesel combustion.

After its first appearance the soot distribution elongates along the bowl wall, following the general flow direction of the wall jets. At 13 CAD ASOI the wall jet from the neighbouring jet can be clearly seen at the bottom edge of the images. At 18 to 19 CAD ASOI the two wall jets collide forming a recirculation zone between the two jets. These series thus cover a large section of the premixed and the spray-driven stages of the combustion process.

The initial soot area growth rate, shown in Figure 5.14, was calculated from the first five images showing an LII signal for all oxygen percentages studied. The soot areas were calculated by applying a threshold of 2.5% of the dynamic range to each image, and the growth rate was calculated from the slope of a linear-fit to the accumulated soot area values.

The soot area growth rate increased as the percentage O_2 was reduced from 21%, and peaked at 13% O_2. Below 13% O_2 the soot area growth rate decreased again. At higher oxygen percentages, the soot oxidation process probably influences the soot area growth rate. As oxidation counteracts soot formation the soot area growth rate is lowered at high oxygen levels. For O_2 percentages below 13%, the soot oxidation process should be limited or at least slower. Thus, the lower area growth rates below 13% O_2 must be due to reduced soot formation. The similarity between Figure 5.14

and the FSN curve showed in Figure 5.12 A is striking but it does not tell the entire story.

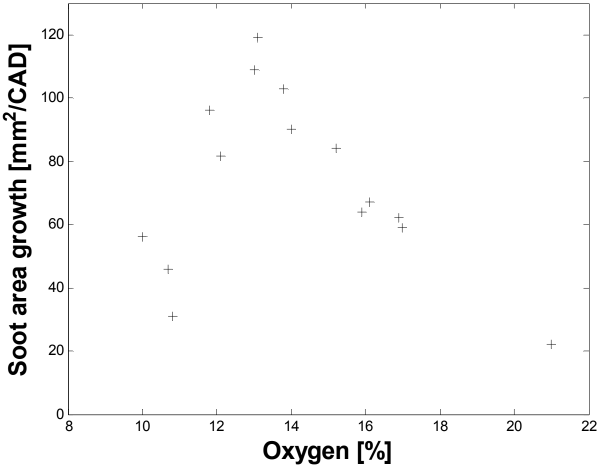

Figure 5.14 Soot area growth rate during the first 5 CAD with an LII-signal when increasing the O_2 from 10 to 21% O_2.

The soot area for 21, 14, 12 and 10% O_2 as a function of CAD ASOI can be seen in Figure 5.15. The first five points on these curves lie under the calculations presented in Figure 5.14 for each oxygen level. Note also that SOI was shifted to later times for increasing percentage of oxygen. At higher O_2 percentages, the soot area grows reaching a peak, after which it decreases. It is, however, difficult to relate the area decrease after the peak to soot oxidation or formation processes, since signal trapping had considerable effects on the data evaluation under these conditions. For O_2 levels below 13% O_2, the soot area grows steadily as a function of time and no peak is evident.

It could also be seen that the first evidence of soot was moved downstream at lower oxygen levels. For 21% O_2 soot started to form well before the jet interacted with the wall. With 14% O_2, the soot started to form at the jet-wall interaction point. At 12% O_2, the soot started to form after the wall interaction but rather close to the jet-wall interaction point. Finally, at 10% O_2 the soot did not form until the recirculation zones between adjacent jets. The LII signal was also weaker in this case than in the other cases.

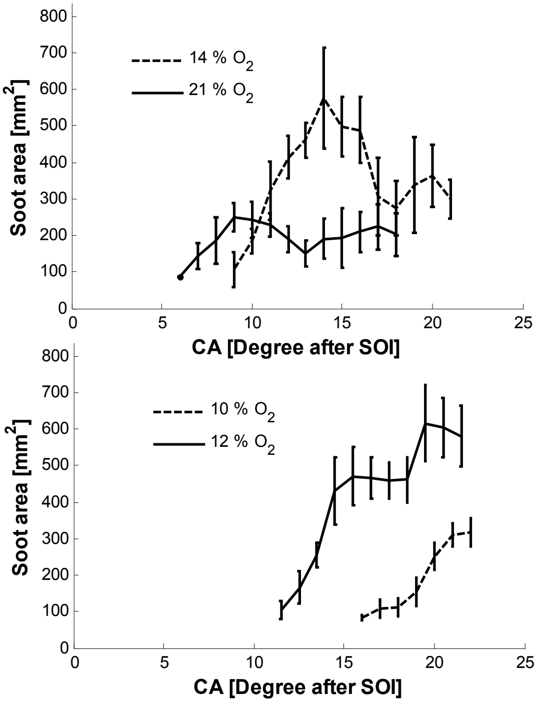

Figure 5.15 Soot area as a function of CAD ASOI for 21, 14, 12, and 10% O_2.

The high-speed LII images also showed that the soot clouds never reached a stationary phase, despite the fact that a long injection duration of 27 CAD was used.

The conclusion drawn was that for high O_2 percentages, above 13%, increased net soot production with decreasing O_2 is the factor behind the increase in engine-out smoke. It is, however, reasonable to assume that reduced soot oxidation at lower O_2 levels also contributes to this effect, although this could not be verified from the data.

At lower O_2 percentages, below the peak in smoke emissions, the total net soot formation decreases. As for the higher O_2 levels, the soot oxidation process should be reduced by lowering the O_2 level. Thus, the decreasing soot trend shows that the decrease in soot formation is more important than the decrease in soot oxidation for very low oxygen levels.

5.6 Gendies –SLIPI in diesel engine

The results from the measurements of the equivalence ratio at the lift-off length (Section 5.4) and time-resolved measurements of the soot distribution (Section 5.5) led to the conclusion that further analysis of the wall jet and the recirculation zone would be of interest. The optical techniques used in this campaign, fuel-tracer LIF and SLIPI, have been discussed in Section 3.3.6, 3.5 and 4.5 and only the relevant engine data will be given here. Further details can also be found in Paper XI.

Two different injector geometries and three different injector pressures were studied. Illustrations of the two injector and fuel jet geometries can be seen in Figure 5.16. Both injectors were four-hole injectors, one symmetrical, with 90° inter-jet angles, and the other asymmetrical, with 45° and 135° inter-jet angles.

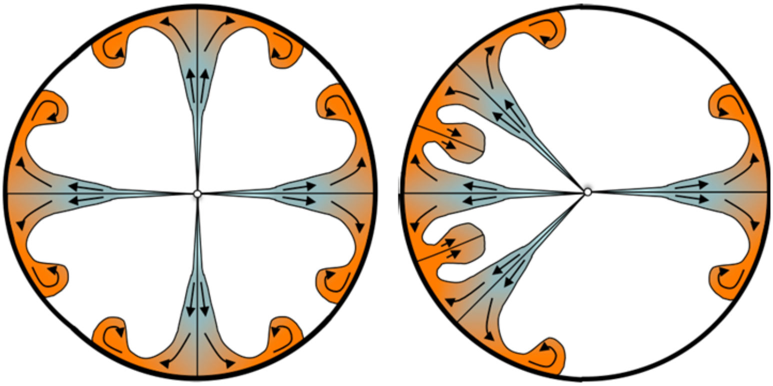

Figure 5.16 Illustration of the symmetrical injector geometry (left), with 90° inter-jet angles, and the asymmetrical injector geometry (right), with 45° and 135° inter-jet angles.

The temporal progression of the asymmetrical injector can be seen in Figure 5.17. The directions of the four fuel jets are indicated to the right in the images as a white “chicken foot“. The timing for each frame is given as the time ASOI and as time AEOI when relevant.

The first images show the leading part of the jet before it impinges on the bowl wall. In the middle row (1.32 to 1.88 ms ASOI), the recirculation zone between the two fuel jets is clearly seen. After EOI (bottom row 2.15 to 2.71 ms ASOI) the region of the free jet (before wall impingement) shows a rapid decrease in Φ. This is probably indicative of an entrainment wave after the end of injection [83].

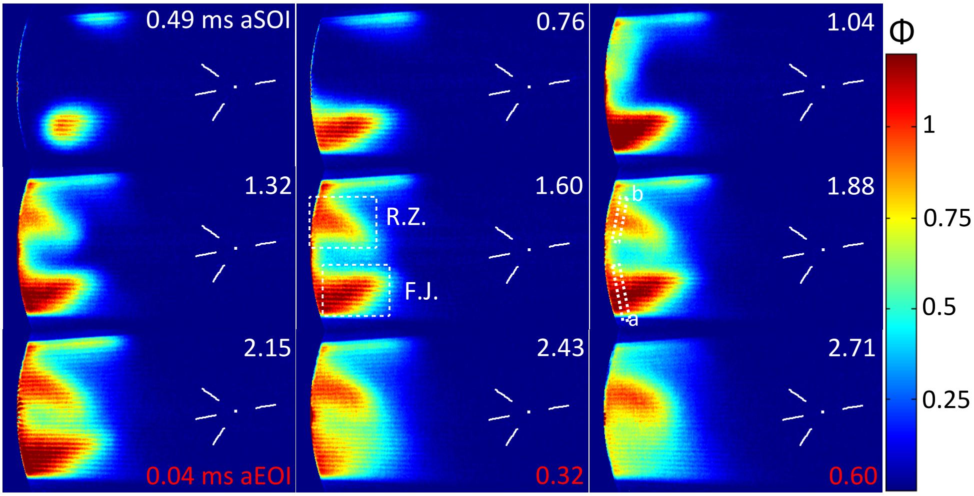

Figure 5.17 SLIPI LIF images (averages) showing the Φ distribution for the asymmetric nozzle at 2000 bar injection pressure. The acquisition time is indicated at the top of each frame as ASOI and AEOI at the bottom of the relevant frames. The parts of the images containing the free jet (F.J.) and the recirculation zone (R.Z.) are indicated in the centre frame. The colour scale indicates the local equivalence ratio, as shown by the colour bar on the right.

From the fuel-LIF images it was possible to study the mixing process between the surrounding gas and the fuel jet. The effect of the interaction between the bowl wall and the fuel jet was of primary interest and in order to illustrate this effect, two regions were selected. One region was positioned just before the impingement of the fuel jet on the bowl wall, indicated by “a” in the sixth frame of Figure 5.17, and the second was positioned just after the region where the two adjacent fuel jets collide and form a recirculation zone. This region is indicated by “b” in the sixth frame of Figure 5.17. As the zones covered the entire width of the fuel jet, the measured Φ values correspond to the average cross-sectional fuel distribution. In between these two zones the fuel jet will have travelled along the bowl wall creating wall jets. The combined data from these two zones could therefore be used to illustrate how the bowl wall effects the mixing process.

Figure 5.18 shows the Φ values for the free jet (Figure 5.18 A) and the recirculation zone (Figure 5.18 B) for the asymmetric injector with a 45° inter-jet angle as a function of time ASOI. Figure 5.19 shows the corresponding graphs for the symmetrical injector with 90° inter-jet angle.

A general trend can be seen for the free jet in Figure 5.18 A. An initial bump at the time of wall impingement is followed by a plateau and then a rapid decrease in equivalence ratio after the end of injection. It is interesting to note that there is no significant difference between the Φ values for different injection pressures for either injector, especially in the recirculation zone. Thus, there does not appear to be an increase in mixing in the wall jet at increased injection pressure. It can be hypothesized that the confined nature of the wall jet in the engine geometry is the reason for this.

The plateau region in the free jet (Figure 5.18 A) before EOI is actually not flat but increases slightly in all cases. This is due to fuel re-entering the free jet from the recirculation zone upstream of the measurement region (see e.g. the lower left frame in Figure 5.17, 2.15 ms ASOI). This trend is not seen in Figure 5.19 as the distance between the recirculation zone and the free jet is large enough to eliminate any feedback to the free jet before the EOI for 90° inter-jet angles.

The rapidly decreasing trend in Φ, seen both in Figure 5.18 A and Figure 5.19 A, after EOI is interesting in terms of mixing process. The decreasing trend appears before the tail of the jet would normally reach the region after EOI. This trend is thus indicative of an entrainment wave [83]. It is most interesting to note that this entrainment wave is not apparent at the start of the recirculation zone for either injector (see Figure 5.18 B and Figure 5.19 B). This implies that the enhanced mixing after EOI is not transmitted via the wall jet to the recirculation zone. The recirculation zones are therefore not affected by this enhanced mixing, which could be beneficial for soot oxidation.

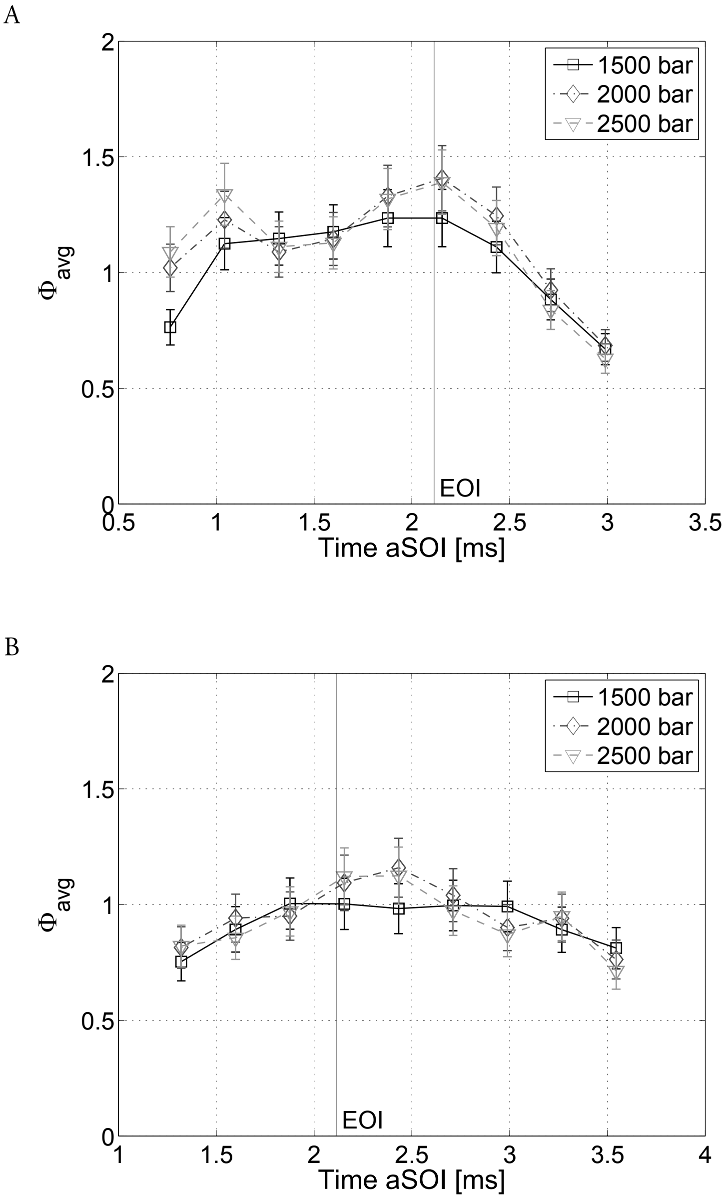

Figure 5.18 Φ values for the asymmetric injector with 45° inter-jet angle. The upper graph (A) shows Φ values from the free jet region prior to wall impact, and the lower graph (B) shows Φ values in the recirculation zone after the wall jet.

A

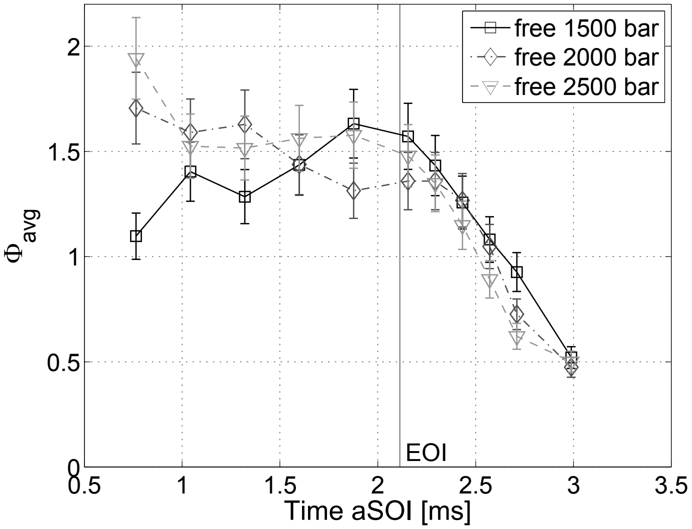

B

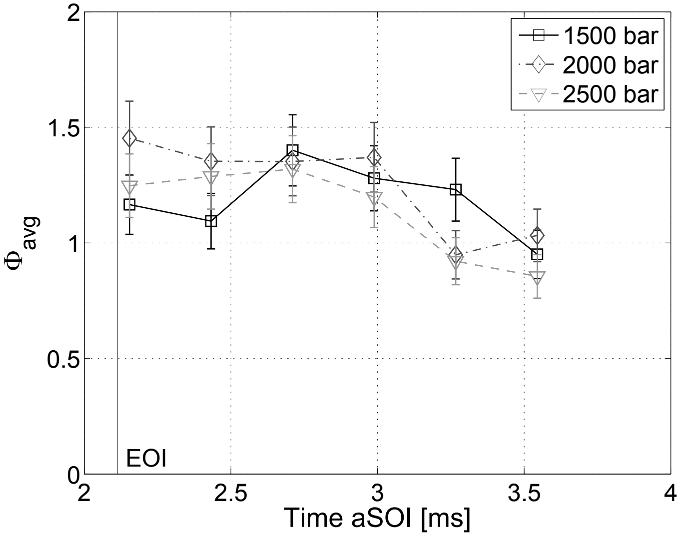

Figure 5.19 Φ values for the symmetrical injector with 90° inter-jet angle. The upper graph (A) shows Φ values from the free jet region prior to the wall impact, and the lower graph (B) shows the Φ values in the recirculation zone after the wall jet.

Equivalence ratios were predicted according to the model developed by Siebers [82, 84] in order to compare the fuel jet in the engine with a theoretical free jet without any jet-wall interactions. The experimental data shown in Figure 5.18 and Figure 5.19 are cross-sectional average Φ values that thus match the predicted values from the model. Several of the model's parameters are difficult to determine and the characteristic length (x^+) could therefore not be calculated a priori. However, knowing the Φ values in the free jet before wall impingement makes it possible to experimentally determine x^+ for each case. Thus, the theoretical equivalence ratio in a fuel jet under identical conditions to those in the experiments, but without the jet-wall interaction could be calculated.

Figure 5.20 shows the ratio between the measured and the predicted Φ values in the recirculation zone for several different cases. The cases with 90° inter-jet spacing and 1500 and 2000 bar injection pressure are not included as a recirculation zone was not formed until around the EOI. Thus the evaluation was not possible for these cases as both zones have to contain a spray-driven fuel jet at the same time for the evaluation to be valid. All the cases presented in Figure 5.20 show a significantly higher Φ value at the start of the recirculation zone compared to the modelled free jet. The 90° inter-jet angle case, with a long section of wall jet, showed a 50% increase. The 45° inter-jet angle cases show similar trends, but to a lesser degree due to the shorter wall jet section before the recirculation zone. This implies that mixing in the wall jet is lower than in a free jet. The confined geometry in the combustion chamber is probably the main reason for this phenomenon.

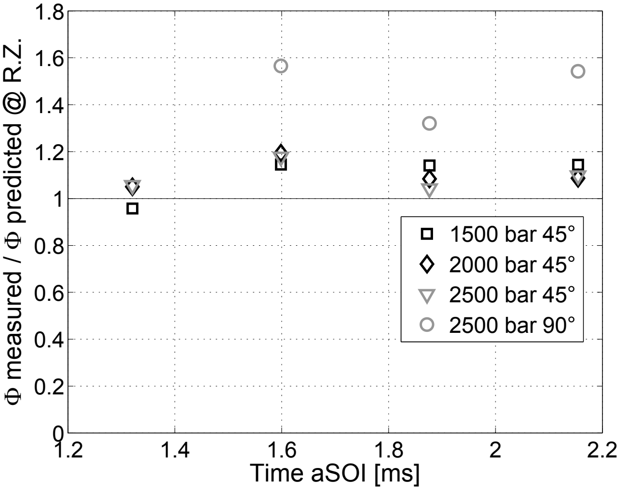

Figure 5.20 Ratio between the measured Φ values in the recirculation zone and the predicted Φ values in a free-jet according to Siebers model at the same downstream distance. The model uses the measured Φ values from the free jet prior to wall impingement to calculate x^+.

Chapter 6 Summary and Outlook

High repetition rate laser diagnostics has been successfully applied to the study of various phenomena in combustion applications. Using a multi-YAG laser and a framing camera allowed the recording of eight images of e.g. PLIF with very high repetition rates (up to 100 MHz, but usually around 10 kHz). This has been used for, e.g., cycle resolved measurements in optical engines.

6.1 Experimental improvements

The improvement between the old and the new multi-YAG laser system was mainly in the pulse power, which increased on average by more than a factor of two (see Table 2.1). Increasing this further in coming generations of multi-YAG systems might be of interest for applications requiring very high repetition rates (>100 kHz), or in applications requiring very large laser sheets, e.g. inside large ship engines.

Increasing the number of pulses may also be of interest. If the flash lamp duration could be extended, more than two pulses could be generated under one flash lamp discharge, in a similar manner to pulse burst systems [14-17]. Alternatively, five or more lasers could be combined into one system. However, increasing the number of pulses requires a similar increase in performance in detectors (framing cameras with more ICCDs) or changing to the use of high repetition rate cameras using CMOS chips. However, extending the number of pulses is associated with a considerable increase in cost. Another option is to use two multi-YAG systems together.

Significant improvements could be made to the sensitivity and resolution of framing cameras. As framing cameras require an additional intensifier to be UV-sensitive some resolution is lost. Developing an intensifier with better resolution might be beneficial in some applications. Another improvement to the framing cameras would be separate optical filters on each channel (ICCD). This would allow for multi spectral detection, e.g. multi-species measurements or two line temperature measurements, using just one framing camera as detector.

Additionally, a substantial amount of time is needed to transfer the large volume of data generated by framing cameras to a computer. Improving the readout time would increase the throughput and thus the ability to record larger data sets with better statistical quality. This also applies to high-speed CMOS cameras, which can generate truly gargantuan amounts of data during a single measurement.

Regarding high-speed COMS cameras, the development of the new scientific CMOS (sCMOS) concept could prove to be interesting. sCMOS cameras clearly demonstrate good resolution and signal-to-noise at increased frame rates compared to normal interline CCD cameras. For combustion applications, however, the necessity for a short time gate for background rejection requires that the sCMOS is equipped with an intensifier. As the intensifier is clearly the limiting factor regarding noise, linearity and resolution for ICCD cameras, this will severely hinder the sCMOS in the same manner. The only remaining benefit of the sCMOS compared to ICCDs for combustion applications is then the slightly increased frame rate. However, further development might make the sCMOS an attractive alternative to today's CCD cameras.

For kHz laser systems, one limitation today is the available pulse energy. Although the system in Lund can produce around 120 W at 532 nm, this is still only 12 mJ/pulse at 10 kHz. This limits the experimental setup, e.g. small laser sheets and the selection of species that can be studied. Future improvements of these systems will probably include higher pulse energies. It is also possible that even higher repetition rates will be achieved, although this is not as interesting in combustion applications. However, at the moment, the intensifier in the high-speed CMOS cameras appears to be the main limitation regarding combustion applications [26]. Improvements in this field are necessary if kHz systems are to gain credibility.

Regarding studies on optical engines, it will be interesting to study the new combustion concept called partially premixed combustion (PPC) using e.g. high-speed measurements of fuel tracer PLIF, formaldehyde PLIF and OH PLIF. PPC shows great potential in minimizing emissions, similar to HCCI but it does not suffer from the lack of combustion control inherent in HCCI. The fundamental understanding of the concept is, however, still incomplete, and laser measurements could certainly improve our knowledge.

Improvements in the design of the optical engines are also forthcoming. Increased peak pressure and longer lifetimes of optical components through modified design of the optical components are the main objectives. This would increase the validity of optical engine measurements, as operating points closer to more realistic scenarios could be selected, e.g. more transient phenomena and higher loads.

6.2 Future measurements

Some suggestions for future measurements by the high-speed diagnostic group at the Division of Combustion Physics are given below.

Combined high-speed 266 nm and 532 nm excitation.

It is possible, with some modifications, to extract both the 266 nm and the 532 nm beams from the Multi-YAG system. Combining the two beams in one laser sheet would allow for simultaneous high-speed droplet tracking (Mie scattering with 532 nm) and fuel vapour measurements in applications where the 266 nm radiation is spectrally overlapped by various LIF signals. This might be interesting for diesel engine applications where small droplets in the fuel jet might adversely affect the PLIF measurements. Another application could be high-speed LII (532 nm excitation) simultaneously with high-speed fuel tracer LIF (266 nm excitation). The introduction of a delay line on one channel would be necessary to avoid cross talk.

The framing camera in these setups would be equipped with a stereoscope or both framing cameras could be used simultaneously. Alternatively, a high-speed CMOS camera could be docked to the SIM 8 camera. This can, however, only be done in applications with sufficient signal, as an extra beam splitter for the auxiliary port would have to be mounted in the SIM 8, effectively reducing the detected signal level by a factor of two.

Lean and rich zones in combustion

Single-shot imaging of the rich (through CO LIF) and the lean (through CH_2O LIF) zones in IC engines would be interesting. As both measurements will probably suffer from interference from other species, e.g. PAHs, on-off resonance measurements would be required. This could be done using the multi-dye system with two dye lasers operating with pyridine 1 or pyridine 2, generating ~708 nm, and two dye lasers operating with coumarine 460, generating ~460 nm. Since all four lasers would require frequency doubling the beams could be overlapped in a manner similar to that shown in Figure 2.5. Rather extensive modifications to two of the dye lasers, for >700 nm operation, and new dielectric mirrors and SHG crystals, for overlapping, would be required. Either both framing cameras or four separate PI MAX cameras would be required for detection.

Double OPO systems.

High-speed on-off resonance measurements could be made with two OPO systems pumped by the multi-YAG. This could generate time-resolved (four double shots) on-off resonance images of different species. A possible application would be OH LIF using realistic fuels, such as kerosene or gasoline. The background from fuel LIF could then be easily subtracted.

Combined detection

The SIM 8 camera has an auxiliary port that allows a second camera to be mounted on the side of it (see Figure 2.10). This could be used to combine the SIM 8 camera with e.g. a high-speed CMOS camera. This would allow for simultaneous detection of, for instance, flame luminescence (high-speed video) and OH fuel tracer LIF (SIM 8). Another option is to dock a spectrometer (with an ICCD camera) onto the SIM 8 camera allowing spectral information to be obtained for one frame of the eight.

Acknowledgements

I seriously considered just saying: Thank you everybody, but as someone pointed out, that would have been the easy way out! So here is a list of the people I would especially like to thank.

Mattias Richter

Employing a student from Chalmers must have taken some persuasion from Marcus side. Anyway, thank you for giving me a chance. My time in Lund has been very interesting and rewarding, much thank to you. I have travelled around nine states in North America as your navigator and taken your brake disks through customs in my bag. I am only sorry that I did not get to see that GT40 operational, but maybe some time…

Marcus Aldén

Thank you for taking me in all those years ago. This period of my life included the greatest changes but working at your department has made the time fly by, as it tends to do when you are having fun. The work has been diverse, challenging and interesting, and as it now draws to an end, I can only say, thank you for giving me this opportunity.

Johannes Lindén

You are an endless source of interesting facts. It was always a bit more interesting to come to work when you were around. Thank you for all our stimulating conversations, and for coping with so much second-hand P3 music; that can't have been easy.

Clément Chartier

Long and many are the hours we have spent in the lab together. Thank you for making the long hours a bit more interesting, and for introducing me to the world of an audiophile.

Andreas Lantz

You're a good friend and colleague. We have had many interesting discussions on both large and small things, especially at the end where we happened to be walking the path towards the finish line at the same time.

Elias Kristensson

We started working together on SACI and ended up with SLIPI, and it was quite easy to see what you preferred. You are excellent at what you do and I am grateful for having worked with you.

Ronald Whiddon

You are an endless source of computer trivia. It is a shame that my computer at work never happened to jump into the path of a truck so we could have had more discussions on what to buy instead.

Jan-Erik Nilsson, Kjell Jonholm and Rutger Lorentsson

Thank you for your assistance in the lab. Without you, my work would have progressed much more slowly during these years. To all the other Ph.D. students at the division; know what you are asking for or you might get exactly that, with a little side order of irony that is.

VOKarna

The PhD students at the Division of Combustion Engines with whom I have had the pleasure of working in the engine rigs: Andreas Vressner, Håkan Persson Ulf Aronsson and Yann Gallo: it has been a fun ride.

To everyone at the Division of Combustion Physics

You are too many to mention by name so I take a step back and bow deeply to you all. I have always looked forward to the next day at the office as I knew that I would be surrounded by interesting and intelligent people. Thank you all!

To my family

I would like to express my most sincere thanks to the love of my life, Agneta. Thank you for your love and support during the entire time of my studies, but especially during these last few months, which have been something rather extraordinary. And thank you Viktor, for always making me smile at just the right moment.

References

[1] IEA, *Key World Energy Statistics*, IEA, 2011.

[2] WHO, *WHO Air quality guidelines for particulate matter, ozone, nitrogen dioxide and sulfur dioxide, Global update 2005, Summary of risk assessment*, World Health Organization, 2006.

[3] Kohse-Höinghaus, K. and Jeffries, J.B., editors, *Applied Combustion Diagnostics*, Taylor and Francis, New York, 2002.

[4] Borghi, R. and Destriau, M., *Combustion and Flames, Chemical and Physical Principles*, Paris, Éditions Technip, 1998.

[5] Pope, S.B., *Turbulent Flows*, Cambridge, Cambridge University Press, 2000.

[6] Joelsson, T., *Large Eddy Simulation of Turbulent Reactive Flows under HCCI Engine Conditions* Department of Energy Sciences, Lund University, Lund, 2011

[7] Kiss, Z.J. and Pressley, R.J., *Crystalline Solid Lasers,* Appl. Opt., **5**(10): p. 1474-1486, 1966.

[8] Geusic, J.E., Marcos, H.M. and Uitert, L.G.V., *Laser Oscillations in Nd-Doped Yttrium Aluminum, Yttrium Gallium and Gadolinium Garnets,* Appl. Phys. Lett., **4**: p. 182, 1964.

[9] Sick, V., Drake, M. and Fansler, T., *High-speed imaging for direct-injection gasoline engine research and development,* Experiments in Fluids, **49**(4): p. 937-947, 2010.

[10] Peterson, B. and Sick, V., *Simultaneous flow field and fuel concentration imaging at 4.8 kHz in an operating engine,* Applied Physics B: Lasers and Optics, **97**(4): p. 887-895, 2009.

[11] Böhm, B., Heeger, C., Boxx, I., Meier, W. and Dreizler, A., *Time-resolved conditional flow field statistics in extinguishing turbulent opposed jet flames using simultaneous highspeed PIV/OH-PLIF,* Proceedings of the Combustion Institute, **32**(2): p. 1647-1654, 2009.

[12] Cundy, M. and Sick, V., *Hydroxyl radical imaging at kHz rates using a frequency-quadrupled Nd:YLF laser,* Applied Physics B: Lasers and Optics, **96**(2): p. 241-245, 2009.

[13] Cundy, M., Trunk, P., Dreizler, A. and Sick, V., *Gas-phase toluene LIF temperature imaging near surfaces at 10 kHz,* Experiments in Fluids, **51**(5): p. 1169-1176, 2011.

[14] Wu, P.P. and Miles, R.B., *High-energy pulse-burst laser system for megahertz-rate flow visualization,* Opt. Lett., **25**(22): p. 1639-1641, 2000.

[15] Jiang, N., Webster, M.C. and Lempert, W.R., *Advances in generation of high-repetition-rate burst mode laser output,* Appl. Opt., **48**(4): p. B23-B31, 2009.

[16] Thurow, B.S., Satija, A. and Lynch, K., *Third-generation megahertz-rate pulse burst laser system,* Appl. Opt., **48**(11): p. 2086-2093, 2009.

[17] Thurow, B.S., Lynch, K.P., Williams, S.T. and Melnick, M.B. *3-D flow imaging using a MHz-rate pulse burst LASER system*, 15th Int Symp on Applications of Laser Techniques to Fluid Mechanics, Lisbon, Portugal, 2010.

[18] Düwel, I., Drake, M.C. and Fansler, T.D. *High-Speed, High-Resolution Laser Imaging of Multihole Fuel Sprays in a Firing Spray-Guided Direct-Injection Gasoline Engine*, ILASS-Europe 19th Annual Conference, Nottingham, England, 2004.

[19] Reeves, M., Towers, D.P., Tavender, B. and Buckberry, C.H., *A high-speed all-digital technique for cycle-resolved 2-D flow measurement and flow visualisation within SI engine cylinders,* Optics and Lasers in Engineering, **31**(4): p. 247-261, 1999.

[20] Theocaris, P.S., Serafetinides, A.A. and Andrianopoulos, N.P., *A high-power multiple ruby laser system for recording dynamic events,* Journal of Physics E: Scientific Instruments, **14**(6): p. 705, 1981.

[21] Hult, J., Richter, M., Nygren, J., Aldén, M., Hultqvist, A., Christensen, M. and Johansson, B., *Application of a High-Repetition-Rate Laser Diagnostic System for Single-Cycle-Resolved Imaging in Internal Combustion Engines,* Applied Optics, **41**(24): p. 5002-5014, 2002.

[22] Hult, J., *Development of Time Resolved Laser Imaging Techniques for Studies of Turbulent Reacting Flows*, Department of Physics, Lund University, Lund, 2002.

[23] Miller, J.D., Engel, S.R., Meyer, T.R., Seeger, T. and Leipertz, A., *High-speed CH planar laser-induced fluorescence imaging using a multimode-pumped optical parametric oscillator,* Opt. Lett., **36**(19): p. 3927-3929, 2011.

[24] Duarte, F.J., *Dye lasers*, in *Tunable Lasers Handbook*, Elsevier Inc. p. 167-218, 1995.

[25] Olofsson, J., *Laser Diagnostic Techniques with Ultra-High Repetition Rate for Studies in Combustion Environments*, Department of Physics, Lund University, Lund, 2007.

[26] Weber, V., Brübach, J., Gordon, R. and Dreizler, A., *Pixel-based characterisation of CMOS high-speed camera systems,* Applied Physics B: Lasers and Optics, **103**(2): p. 421-433, 2011.

[27] Folkierski, A., *Report on high-speed photography,* Nuclear Instruments and Methods, **4**(5): p. 346-351, 1959.

[28] Ralchenko, Y., Kramida, A., Reader, J. and Team, N.A., *NIST Atomic Spectra Database (version 4.1)*, http://physics.nist.gov/asd, National Institute of Standards and Technology, 2011.

[29] Bowditch, F.W., *A new tool for combustion research - A quartz piston engine,* SAE Transaction, **69**: p. 17-23, 1961.

[30] Aronsson, U., Chartier, C., Horn, U., Andersson, Ö., Johansson, B. and Egnell, R., *Heat Release Comparison Between Optical and All-Metal HSDI Diesel Engines,* SAE Technical Paper 2008-01-1062, 2008.

[31] Hanson, R.K., *Combustion diagnostics: Planar imaging techniques,* Symposium (International) on Combustion, **21**(1): p. 1677-1691, 1988.

[32] Long, D.A., *Raman Spectroscopy*, London, McGraw-Hill International Book Company, 1977.

[33] Eckbreth, A.C., *Laser diagnostics for combustion temperature and species*, 2nd edition, Amsterdam, Gordon & Breach, 1996.

[34] Herzberg, G., *Molecular spectra and molecular structure. Volume 2, Infrared and Raman spectra of polyatomic molecules*, New York, D. Van Nostrand company, 1962.

[35] Faris, G.W. and Copeland, R.A., *Ratio of oxygen and nitrogen Raman cross sections in the ultraviolet,* Appl. Opt., **36**(12): p. 2684-2685, 1997.

[36] Li, Z.S., Kiefer, J., Zetterberg, J., Linvin, M., Leipertz, A., Bai, X.S. and Aldén, M., *Development of improved PLIF CH detection using an Alexandrite laser for single-shot investigation of turbulent and lean flames,* Proceedings of the Combustion Institute, **31**(1): p. 727-735, 2007.

[37] Ditchburn, R.W. and Young, P.A., *The absorption of molecular oxygen between 1850 and 2500 Å,* Journal of Atmospheric and Terrestrial Physics, **24**(2): p. 127-139, 1962.

[38] Aldén, M., Wallin, S. and Wendt, W., *Applications of two-photon absorption for detection of CO in combustion gases,* Applied Physics B: Lasers and Optics, **33**(4): p. 205-208, 1984.

[39] Linow, S., Dreizler, A., Janicka, J. and Hassel, E.P., *Comparison of two-photon excitation schemes for CO detection in flames,* Applied Physics B: Lasers and Optics, **71**(5): p. 689-696, 2000.

[40] Olofsson, J., Seyfried, H., Richter, M., Aldén, M., Vressner, A., Hultqvist, A., Johansson, B. and Lombaert, K., *High-Speed LIF Imaging for Cycle-Resolved Formaldehyde Visualization in HCCI Combustion*, 2005.

[41] Clouthier, D.J. and Ramsay, D.A., *The Spectroscopy of Formaldehyde and Thioformaldehyde,* Annual Review of Physical Chemistry, **34**: p. 31-58, 1983.

[42] Brackmann, C., Nygren, J., Bai, X., Li, Z.S., Bladh, H., Axelsson, B., Denbratt, I., Koopmans, L., Bengtsson, P.-E. and Aldén, M., *Laser-induced fluorescence of formaldehyde in combustion using third harmonic Nd:YAG laser excitation,* Spectrochimica Acta Part A: Molecular and Biomolecular Spectroscopy, **59**(14): p. 3347-3356, 2003.

[43] Fansler, T.D., French, D.T. and Drake, M.C., *Fuel Distributions in a Firing Direct-Injection Spark-Ignition Engine Using Laser-Induced Fluorescence Imaging,* SAE Technical Paper 950110, 1995.

[44] Schulz, C. and Sick, V., *Tracer-LIF diagnostics: quantitative measurement of fuel concentration, temperature and fuel/air ratio in practical combustion systems,* Progress in Energy and Combustion Science, **31**(1): p. 75-121, 2005.

[45] Ma, X., He, X., Wang, J.-x. and Shuai, S., *Co-evaporative multi-component fuel design for in-cylinder PLIF measurement and application in gasoline direct injection research,* Applied Energy, **88**(8): p. 2617-2627, 2011.

[46] Williams, B., Ewart, P., Wang, X., Stone, R., Ma, H., Walmsley, H., Cracknell, R., Stevens, R., Richardson, D., Fu, H. and Wallace, S., *Quantitative planar laser-induced fluorescence imaging of multi-component fuel/air mixing in a firing gasoline-direct-injection engine: Effects of residual exhaust gas on quantitative PLIF,* Combustion and Flame, **157**(10): p. 1866-1878, 2010.

[47] Sahoo, D., Petersen, B. and Miles, P., *Measurement of Equivalence Ratio in a Light-Duty Low Temperature Combustion Diesel Engine by Planar Laser Induced Fluorescence of a Fuel Tracer,* SAE Int. J. Engines 4(2): p. 2312-2325 2011.

[48] Mueller, M., *General Air Fuel Ratio and EGR Definitions and their Calculation from Emissions,* SAE Technical Paper 2010-01-1285, 2010.

[49] Reboux, J., Puechberty, D. and Dionnet, F., *A New Approach of Planar Laser Induced Fluorescence Applied to Fuel/Air Ratio Measurement in the Compression Stroke of an Optical S.I. Engine,* SAE Technical Paper, 941988, 1994.

[50] Koban, W., Koch, J.D., Hanson, R.K. and Schulz, C., *Oxygen quenching of toluene fluorescence at elevated temperatures,* Applied Physics B: Lasers and Optics, **80**(6): p. 777-784, 2005.

[51] Grossmann, F., Monkhouse, P.B., Ridder, M., Sick, V. and Wolfrum, J., *Temperature and pressure dependences of the laser-induced fluorescence of gas-phase acetone and 3-pentanone,* Applied Physics B: Lasers and Optics, **62**(3): p. 249-253, 1996.

[52] Bladh, H., *On the use of Laser-Induced Incandescence for Soot Diagnostics*, Department of Physics, Lund university, Lund, 2007.

[53] Melton, L.A., *Soot Diagnostics Based on Laser-Heating,* Applied Optics, **23**(13): p. 2201-2208, 1984.

[54] Bladh, H., Johnsson, J. and Bengtsson, P.-E., *On the dependence of the laser-induced incandescence (LII) signal on soot volume fraction for variations in particle size,* Applied Physics B: Lasers and Optics, **90**(1): p. 109-125, 2008.

[55] Dec, J.E., *Soot distribution in a D. I. diesel engine using 2-D imaging of laser-induced incandescence, elastic scattering, and flame luminosity,* SAE Technical Paper 920115, 1992.

[56] Zhao, H. and Ladommatos, N., *Optical diagnostics for soot and temperature measurement in diesel engines,* Progress in Energy and Combustion Science, **24**: p. 221-255, 1998.

[57] Inagaki, K., Takasu, S. and Nakakita, K., *In-cylinder quantitative soot concentration measurement by laser-induced incandescence,* SAE Technical Paper 1999-01-0508, 1999.

[58] Francqueville, L., Bruneaux, G. and Thirouard, B., *Soot Volume Fraction Measurements in a Gasoline Direct Injection Engine by Combined Laser Induced Incandescence and Laser Extinction Method,* SAE Technical Paper 2010-01-0346, 2010.

[59] Bladh, H., Hildingsson, L., Gross, V., Hultqvist, A. and Bengtsson, P.-E. *Quantitative soot measurements in an HSDI Diesel engine*, Proceedings of the 13th International Symposium on Applications of Laser Techniques to Fluid Mechanics, Lisbon, Portugal, 2006.

[60] De Iuliis, S., Cignoli, F., Maffi, S. and Zizak, G., *Influence of the cumulative effects of multiple laser pulses on laser-induced incandescence signals from soot,* Applied Physics B: Lasers and Optics, **104**(2): p. 321-330, 2011.

[61] Yoder, G.D., Diwakar, P.K. and Hahn, D.W., *Assessment of soot particle vaporization effects during laser-induced incandescence with time-resolved light scattering,* Applied Optics, **44**(20): p. 4211-4219, 2005.

[62] Neil, M.A.A., Juskaitis, R. and Wilson, T., *Method of obtaining optical sectioning by using structured light in a conventional microscope.,* Opt. Lett., **22**: p. 1905-1907, 1997.

[63] Kristensson, E., *Structured Laser Illumination Planar Imaging SLIPI Applications for spray diagnostics*, Department of Physics, Lund University, Lund, 2012.

[64] Cole, M.J., Siegel, J., Webb, S.E.D., Jones, R., Dowling, K., Dayl, M.J., Parsons-Karavassilis, D., French, P.M.W., M.J., L., Sucharov, L.O.D., Neil,

M.A.A., Juskaitis, R. and Wilson, T., *Time-Domain Whole-Field Fluorescence Lifetime imaging with optical sectioning.,* J. Microsc., **203**: p. 246-257, 2000.

[65] Poinsot, T. and Veynante, D., *Theoretical and Numerical Combustion*, Philadelphia, Edwards Inc., 2001.

[66] Aldén, M., Edner, H. and Svanberg, S., *Simultaneous, Spatially Resolved Monitoring of C2 and OH in a C2H2/O2 Flame Using a Diode Array Detector,* Applied Physics B: Lasers and Optics, **29**(2): p. 93-97, 1982.

[67] Gordon, R.L., Masri, A.R. and Mastorakos, E., *Simultaneous Rayleigh temperature, OH- and CH2O-LIF imaging of methane jets in a vitiated coflow,* Combustion and Flame, **155**(1-2): p. 181-195, 2008.

[68] Barlow, R.S., Dibble, R.W. and Lucht, R.P., *Simultaneous measurement of Raman scattering and laser-induced OH fluorescence in nonpremixed turbulent jet flames,* Opt. Lett., **14**(5): p. 263-265, 1989.

[69] Barlow, R.S. and Carter, C.D., *Raman/Rayleigh/LIF measurements of nitric oxide formation in turbulent hydrogen jet flames,* Combustion and Flame, **97**(3-4): p. 261-280, 1994.

[70] Donbar, J.M., Driscoll, J.F. and Carter, C.D., *Reaction zone structure in turbulent nonpremixed jet flames--from CH-OH PLIF images,* Combustion and Flame, **122**(1-2): p. 1-19, 2000.

[71] Stårner, S.H., Bilger, R.W., Dibble, R.W., Barlow, R.S., Fourguette, D.C. and Long, M.B., *Joint planar CH and OH LIF imaging in piloted turbulent jet diffusion flames near extinction,* Symposium (International) on Combustion, **24**(1): p. 341-349, 1992.

[72] Paul, P.H. and Najm, H.N., *Planar laser-induced fluorescence imaging of flame heat release rate,* Symposium (International) on Combustion, **27**(1): p. 43-50, 1998.

[73] Ayoola, B.O., Balachandran, R., Frank, J.H., Mastorakos, E. and Kaminski, C.F., *Spatially resolved heat release rate measurements in turbulent premixed flames,* Combustion and Flame, **144**(1-2): p. 1-16, 2006.

[74] Böckle, S., Kazenwadel, J., Kunzelmann, T., Shin, D.-I., Schulz, C. and Wolfrum, J., *Simultaneous single-shot laser-based imaging of formaldehyde, OH, and temperature in turbulent flames,* Proceedings of the Combustion Institute, **28**(1): p. 279-286, 2000.

[75] Kiefer, J., Li, Z.S., Zetterberg, J., Bai, X.S. and Aldén, M., *Investigation of local flame structures and statistics in partially premixed turbulent jet flames using simultaneous single-shot CH and OH planar laser-induced fluorescence imaging,* Combustion and Flame, **154**(4): p. 802-818, 2008.

[76] Li, Z.S., Li, B., Sun, Z.W., Bai, X.S. and Aldén, M., *Turbulence and combustion interaction: High resolution local flame front structure visualization*

using simultaneous single-shot PLIF imaging of CH, OH, and CH2O in a piloted premixed jet flame, Combustion and Flame, **157**(6): p. 1087-1096, 2010.

[77] Duwig, C., Li, B., Li, Z.S. and Aldén, M., *High resolution imaging of flameless and distributed turbulent combustion,* Combustion and Flame, **159**(1): p. 306-316, 2012.

[78] Christensen, M. and Johansson, B., *The Effect of In-Cylinder Flow and Turbulence on HCCI Operation,* SAE Technical Paper 2002-01-2864, 2002.

[79] Christensen, M., Johansson, B. and Hultqvist, A., *The Effect of Combustion Chamber Geometry on HCCI Operation,* SAE Technical Paper 2002-01-0425, 2002.

[80] Persson, H., *Spark Assisted Compression Ignition SACI*, Department of Energy Sciences, Lund University, Lund, 2008.

[81] Sjöberg, M. and Dec, J.E., *Smoothing HCCI Heat Release with Vaporization-Cooling-Induced Thermal Stratification using Ethanol,* SAE Int. J. Fuels Lubr., **5**(1): p. 7-27, 2011.

[82] Siebers, D.L., *Scaling Liquid-Phase Fuel Penetration in Diesel Sprays Based on Mixing-Limited Vaporization,* SAE Technical Paper 1999-01-0528, 1999.

[83] Musculus, M.P.B. and Kattke, K., *Entrainment Waves in Diesel Jets,* SAE Int. J. Engines, **2**(1): p. 1170-1193, 2009.

[84] Naber, J.D. and Siebers, D.L., *Effects of Gas Density and Vaporization on Penetration and Dispersion of Diesel Sprays,* SAE Technical Paper 960034, 1996.

Summary of the Papers

Paper I

In this study high-speed fuel tracer LIF was used to investigate geometry-generated turbulence effects in an HCCI engine. Two different piston geometries were used, one with a flat top, creating a thin disk-shaped combustion chamber, and one with a large square bowl in the piston.

I performed the laser measurements together with Jimmy Olofsson and Hans Seyfried. The engine rig was operated by Andreas Vressner. I performed the post-processing of the LIF data. Jimmy Olofsson and Hans Seyfried had the main responsibility for writing the manuscript to which I contributed the data images.

Paper II

In this study, the high-speed fuel tracer LIF measurements presented in Paper I were compared to LES of the HCCI engine with the same piston geometries. It was shown that temperature and not turbulence was the main cause of the flame-front-like combustion in the square bowl geometry.

I performed the laser measurements, together with Jimmy Olofsson and Hans Seyfried, and performed the post-processing of the LIF data. The LES were performed by Rixin Yu, and the engine rig was operated by Andreas Vressner. Rixin Yu and Xue-Song Bai had the main responsibility for writing the manuscript, to which I mainly contributed the LIF data images.

Paper III

Spark assisted compression ignition was studied using high-speed fuel tracer LIF in order to investigate the effects of fuel stratification. The results showed that increased stratification led to significant changes in the SACI combustion.

I performed the laser measurements and the post processing of the LIF data, together with Elias Kristensson. The engine rig was operated by Håkan Persson who also performed the pressure trace analysis. The responsibility for writing the manuscript was shared between Håkan Person, me and Elias Kristensson.

Paper IV

An OPO unit was tested and evaluated regarding high-speed fluorescence measurements. The OPO unit was operated together with the multi-YAG laser system and performed well under very high repetition rate pumping.

I performed the measurements together with Elias Kristensson and Guido Göritz and Kai Knebel who operated and installed the OPO unit. I performed the post-processing of the data and was responsible for writing the manuscript.

Paper V

Fuel-air ratios inside a fuel jet in a heavy-duty diesel engine were measured using Raman spectroscopy. A DoE setup was employed to show the effects from oxygen level, injection pressure and ambient density on the mixing between the fuel and the surrounding gas in the lift-off region. The measurements showed a low correlation between the equivalence ratio in the lift-off region and engine-out smoke.

I performed the measurements together with Ulf Aronsson and Clément Chartier. I had the main responsibility for the laser diagnostics, while Ulf and Clément were responsible for the engine rig. I performed the post-processing of the Raman data, and Ulf and Öivind Andersson performed the DoE analysis correlating the data to different engine parameters. I wrote the manuscript together with Ulf Aronsson.

Paper VI

Measurements of the actual soot distribution in a heavy-duty diesel engine were performed using high-speed LII, providing series of cycle-resolved images of the soot distribution. The soot distribution was studied as a function of oxygen concentration. The results showed that soot formation is only partially responsible for the engine-out soot, and that soot oxidation may be more important.

I performed the measurements together with Ulf Aronsson, Clément Chartier and Rikard Wellander. I had the main responsibility for the laser diagnostics. Ulf and Clément were responsible for the engine rig. I performed some of the post-processing while Ulf contributed the greater part. Ulf Aronsson was responsible for the preparation of the manuscript, to which I contributed several sections.

Paper VII

Studies of high-speed LII from atmospheric flames and in a heavy-duty Diesel engine were performed using the multi-YAG laser. The results from the atmospheric flames showed that a large proportion of the soot was destroyed after several high-power laser pulses. The engine measurements, however, showed a surprisingly small effect from sublimation, indicating that high-speed LII in diesel engines might actually, in this aspect, be easier.

I performed the measurements in the atmospheric pressure flames and had the main responsibility for the laser diagnostics in the engine measurements, which were carried out together with Ulf Aronsson, Clément Chartier and Rikard Wellander. I performed the data evaluation and was responsible for writing the manuscript.

Paper VIII

This paper describes the first application of SLIPI to gas phase LIF and in-cylinder measurements in an IC engine. The measurements required some development of the SLIPI technique, and were carried out in a heavy duty diesel engine. A comparison between quantitative LIF using SLIPI and regular LIF (also quantitative) showed that SLIPI indicated lower equivalence ratios in the free jet but not in the recirculation zone between the jets.

I performed the measurements together with mainly Clément Chartier and Elias Kristensson. We also cooperated in the data evaluation and in preparing the manuscript, for which I had the main responsibility.

Paper IX

Quantitative fuel tracer LIF using SLIPI was performed with different injector geometries and injection pressures. The equivalence ratio in the free jet before wall impingement and in the recirculation zone between adjacent fuel jets was studied in detail. The results indicated that the mixing in the wall jet was aggravated compared to a free jet (without the bowl wall) under the same conditions, and that the entrainment wave after the end of injection did not survive beyond the wall impingement.

I performed the measurements together with mainly Clément Chartier and Elias Kristensson. We also cooperated in the data evaluation and in preparing the manuscript, for which Clément had the main responsibility.

Paper X

Simultaneous OH, CH, CH_2O and toluene PLIF measurements were performed in a methane jet flame for several different jet flow speeds. The setup involved four laser sheets with different wavelengths and four ICCD detectors. The evaluation involved calculating the spatial overlap between the different species, and showed that turbulence is mainly affecting mixing in the preheating zone of the jet flame.

I designed the experiment together with Mattias Richter, and performed the measurements with some assistance from Bo Li and Joakim Rosell. I performed the data evaluation and was responsible for preparing the manuscript.

Paper XI

Three different excitation–detection schemes for two-photon CO LIF were compared. Pressure dependences, and as well as the interference from C_2 were evaluated for the three different schemes. The results showed that the pressure dependences were stronger for the third-positive group but that it suffers less from C_2 interference compared to the other two schemes.

I performed the measurements together with Joakim Rosell. We also cooperated in the data evaluation and in preparing the manuscript.